

# Experimental Study on Droplet Breakup in Two-Phase Microfluidic System

Submitted in partial fulfillment of the requirements  
of the degree of

Doctor of Philosophy

of the

Indian Institute of Technology Bombay, India

and

Monash University, Australia

by

**Sagar Narhari Agnihotri**

Supervisors:

Prof. Rajneesh Bhardwaj (IIT Bombay)

Prof. Adrian Neild (Monash University)



*The course of study for this award was developed jointly by  
Monash University, Australia and the Indian Institute of Technology Bombay, India  
and was given academic recognition by each of them.  
The programme was administrated by the IITB-Monash Research Academy*

(May 2021)



# **Declaration**

I declare that this written submission represents my ideas in my own words and where other's ideas or words have been included, I have adequately cited and referenced the original sources. I also declare that I have adhered to all principles of academic honesty and integrity and have not misrepresented or fabricated or falsified any idea/data/fact/source in my submission. I understand that any violation of the above will be cause for disciplinary action by the Institute and can also evoke penal action from the sources which have thus not been properly cited or from whom proper permission has not been taken when needed.

## **Notice 1**

Under the Copyright Act 1968, this thesis must be used only under the normal conditions of scholarly fair dealing. No results or conclusions should be extracted from it, nor should it be copied or closely paraphrased in whole or in part without the written consent of the author. Proper written acknowledgement should be made for any assistance obtained from this thesis.

## **Notice 2**

I certify that I have made all reasonable efforts to secure copyright permissions for third party content included in this thesis and have not knowingly added copyright content to my work without the owner's permission.

**Sagar Narhari Agnihotri**



# Acknowledgements

I express my gratitude to my supervisors, Prof. Rajneesh Bhardwaj (IIT Bombay) and Prof. Adrian Neild (Monash University), for their support, patience, and endless technical discussions during my PhD. I am thankful to PhD research progress committee (RPC) members Prof. Victor Cadarso Busto from Monash University and Prof. Venkat Gundabala from IIT Bombay for their technical inputs in annual progress seminars. I acknowledge the Centre of excellence in Nanofabrication (CEN) IITB and Melbourne Centre of Nanofabrication (MCN) for the microfabrication process's facilities. I gratefully acknowledge the funding received towards my PhD fellowship from IITB-Monash Research Academy. I want to thank Prof. Murali Sastry, ex-CEO of IITB-Monash Research Academy, for his support when my visa process got delayed for two years.

I want to acknowledge my senior IITB lab mates, Dr Hemanshul Garg, Dr Anup Kundu, Dr Atul Soti, Dr Nagesh Patil and fellow IITB labmates and friends, Manish Kumar, Prathamesh Bange, Dr Laxman Malla, Rahul Mishra, Sarvesh Shukla, Mayur Bonkile, Ashish Pawar, Bhavesh Kamaliya, Vivek Garg for making PhD tenure memorable. I am grateful to Dr Anwesh Gaddam and Ayaz Siddique for teaching me the basics of microfabrication and PDMS moulding during the initial days of my PhD. I am grateful to Monash University labmates Dr Saab, Dr Jason, Jyunyang, Joe, Gargi, Melati, kamal and my dearest friend Mahraz for making Monash stay genuinely memorable.

I am grateful to my mother, brother, sister-in-law, uncle, aunts and cousins for their love and affection. I wish my late father could have lived to see me getting a PhD. I am grateful to my wife for her constant support, patience and believing in me. Finally, I am thankful to all my teachers for igniting my curiosity in science.

Dedicated  
to the fond memory of my father  
**Late Narhari Bhimsen Agnihotri**



## Abstract

Droplet-based microfluidics involves the generation and manipulation of droplets in a two-phase microfluidic system. With the advent of microfluidic device fabrication using soft lithography techniques in poly-dimethyl siloxane (PDMS), droplet-based microfluidics has attracted significant attention. Today, it finds application in chemical, biological and biomedical interdisciplinary research areas. The present PhD thesis investigates one of the most crucial droplet manipulation capabilities, the controlled breakup of droplets in the two-phase microfluidic system.

First, we experimentally and numerically investigate droplets' interaction with a T-junction that forms the entrance to a bypass channel. The PDMS microchannel is fabricated using standard soft lithography techniques. Droplets are generated upstream at standard T-junction. These generated droplets can interact with a second T-junction, which acts as the start of the bypass channel, which is a channel loop that later re-joins the main channel. Specifically, the effect of Capillary Number ( $Ca$ ) and the bypass channel's relative width to the main channel ( $\beta$ ) is examined. Regimes of droplet breakup and no breakup are plotted on the  $Ca$ - $\beta$  plane. We observe a critical value of  $Ca$  at constant  $\beta$  and vice versa at which droplet breakup occurs. Combining experimental data with numerical simulations, we show that droplet breakup occurs when the average shear stress and hydrodynamic pressure drop across the trapped droplet exceed the differential Laplace pressure. Droplet breakup at the entrance of the bypass channel shows squeezing and dripping regime like droplet generation. We extended this study for the selective breakup of droplets at two locations using two single-layer microvalves. The microfluidic system consists of a standard droplet generation section upstream and a droplet division section downstream. The droplet division section is designed using resistive network analysis so that the same flow rate enters each junction. We observed five different regimes of droplet breakup, namely, (1) no droplet breakup at either junction, (2) droplet breakup in the first junction, (3) droplet breakup in both junctions with higher daughter droplet volume in the first junction, (4) daughter droplet volume higher in the second junction, and (5) intermittent droplet breakup at both junctions. Under specific flow conditions, the nature of the droplet interaction with both the junctions is similar. We then showed design requirements for microvalves' location, simulated by deformation of the main channel wall. Using results from the simulations, we experimentally show the droplets' selective breakup at either junction using two single-layer microvalves.



We extend this new technique to selectively breakup and merge different droplets at four locations using eight single-layer microvalves. We generate four different coloured droplets upstream using four standard T-junctions controlled by four microvalves. We could generate the same kind of droplets, pairs of droplets, or four different droplets, one after the other depending on the requirement, showing excellent operational flexibility. We designed four chambers downstream of the splitting junctions; each containing pillar induced merging section. Again, resistive network analysis was used so that the same flow rate enters each junction. We observed four regimes of droplet interaction with these four junctions. We operated the system in a regime where there is no droplet breakup at all four junctions. The generated droplets are then split selectively at four junctions by altering local geometries by the actuation of single-layer microvalves. Finally, we have shown the ability to merge two similar droplets and two different kinds of droplets in various concentrations. The presented microfluidic platform provides control over the valve pressure at each junction which gives the user complete ability over the volume of droplet and kind of droplet which is split, and at which junction the splitting and subsequent merging events take place.

# Table of Contents

<b>1</b>	<b>Introduction .....</b>	<b>1</b>
1.1	Droplet Generation.....	1
1.2	Droplet Breakup and Sorting.....	13
1.3	Droplet Merging and Mixing .....	22
1.4	Scope and Objective of the Present Thesis .....	24
1.5	Organisation of the Thesis .....	25
<b>2</b>	<b>Droplet Breakup at the Entrance of the Bypass Channel in a Microfluidic System .....</b>	<b>27</b>
2.1	Introduction .....	27
2.2	Methodology .....	30
2.3	Results .....	34
2.4	Discussion .....	42
2.5	Application of Present work in Droplet-Based Microfluidics .....	51
2.6	Closure.....	51
<b>3</b>	<b>Microfluidic Valves for Selective on-Chip Droplet Breakup at Multiple Sites .....</b>	<b>54</b>
3.1	Introduction .....	54
3.2	Methodology .....	57
3.3	Results and Discussion .....	59
3.4	Closure.....	74
<b>4</b>	<b>Controlled Droplet Manipulation and Interaction using Single Layer Microvalves.....</b>	<b>76</b>

4.1	Introduction .....	76
4.2	Methods and Materials.....	78
4.3	Results and Discussion .....	79
4.4	Closure.....	94
<b>5</b>	<b>Conclusion and Future Scope of Work.....</b>	<b>96</b>
5.1	Conclusions.....	96
5.2	Future Scope of Work.....	98
	<b>Appendix.....</b>	<b>100</b>
	<b>List of Publications.....</b>	<b>122</b>

## List of Figures

<b>Figure 1.1:</b> Schematic showing geometries for droplet generation (a) T-junction, (b) flow-focusing geometry, and (c) co-flow geometry. Here $Q_c$ represents the flow rate of the continuous fluid, and $Q_d$ represents the flow rate of the discontinuous fluid. ....	2
<b>Figure 1.2:</b> Active methods of droplet generation (a-h) Single-layer microvalves for control of droplet size and frequency in a flow-focusing device [31]. (i) Application of SAW near the flow-focusing junction for controlling droplet size [33]. Reproduced from ref. 31 and 33 with permission. ....	5
<b>Figure 1.3:</b> A schematic representation of the shape of the discontinuous phase entering the main channel, which is carrying a continuous phase just before the droplet generation. $P_c$ and $P_d$ represent hydrodynamic pressure in the continuous and discontinuous phase, respectively.....	7
<b>Figure 1.4 :</b> Variation of $P_c$ , $P_d$ and $\Delta P$ during droplet generation at T-junction [54]. (a-b) Pressure acting on a droplet along with radius of curvature. (c-e) Variation of pressure acting on a droplet during different stages of droplet generation. Reproduced from ref. 54 with permission. ....	11
<b>Figure 1.5:</b> (a-j) Image sequence from Link et al. [56] showing droplet interaction with T-junction with the width of the channel ( $w_0$ ), length of the droplet ( $l_0$ ), and velocity ( $v$ ) shown. (k) Regime map showing breakup and non-breakup regimes plotted on extension Vs. Capillary Number. Reproduced from ref. 56 with permission. ....	14

<b>Figure 1.6:</b> Image sequence from Ménétrier-Deremble and Tabeling [57] showing outcomes of droplet interaction with the T-junction (a) Direct breakup (b) No breakup (c) Retarded breakup. (d) The geometry used for experiments. Reproduced from ref. 57 with permission. ....	15
<b>Figure 1.7:</b> Working principle of the device which uses an electric field for sorting based on the polarity of the droplets [64]. Droplets are sorted in one of the three outlets shown. Reproduced from ref. 64 with permission.....	17
<b>Figure 1.8:</b> Laser [73] and microheater [75] induced droplet breakup. (a) Symmetric mother droplet breakup in both the branches in the absence of laser. (b) Asymmetric mother droplet breakup when the laser is turned on. The branch in which laser is turned on results in smaller daughter droplet volume. (c) Schematic showing micro heater placed on one side of the simple bifurcating junction resulting in droplet being completely sucked on the side of the channel integrated with microheater. (d) Micro heater temperature is plotted against the size of daughter droplet formed showing different regimes of droplet breakup. Reproduced from ref. 73 and 75 with permission. ....	18
<b>Figure 1.9:</b> (a) SAW [76] used for sorting of the droplet, the first figure shows the path of a droplet when SAW is not actuated while the second figure shows the path of droplet after actuation of SAW. (b) Power supplied to SAW [77] plotted against the ratio of droplet division at Y-junction (c) SAW [80] used for selective droplet breakup and merging at T-junction of a bypass channel. Reproduced from ref. 76,77 and 80 with permission. ....	19

**Figure 1.10: (a-c)** Single-layer microvalve used for droplet sorting [96] at a bifurcating Y-junction. **(d-h)** Multilayer microvalve, in which control channel is located on top of the flow channel is used for droplet sorting [94]. Reproduced from ref. 96 and 94 with permission. ....21

**Figure 1.11:** Passive methods to achieve droplet merging **(a)** Image sequence showing pillar induced [106] droplet merging. **(b)** Use of fusion chamber located at a trifurcating junction for droplet merging [104] **(c)** Image sequence showing merging of two and three droplets. Reproduced from ref. 106 and 104 with permission. ....23

**Figure 1.12:** Active methods of droplet merging. **(a)** Use of surface acoustic waves and expansion channel to demonstrate on-demand merging of two droplets [113]. **(b)** Use of electric field to merge two droplets of different sizes [111]. Reproduced from ref. 113 and 111 with permission. ....24

**Figure 2.1:** Schematic of the setup and geometry used in the present work. Both continuous and discontinuous phase are driven into the microfluidic system using two separate syringe pumps. Deionized water is the discontinuous phase, and oil (paraffin oil/ silicone oil) is the continuous phase. ....31

**Figure 2.2: (a)** Problem definition shown by a schematic. The computational domain is shown by a dotted box and boundary conditions are shown at the inlet, outlet, and wall **(b)** Zoomed in view of the entrance to the bypass channel and droplet shape before interaction with it. **(c)** Mesh is plotted in the region close to the entrance to the bypass channel. ....33

**Figure 2.3:** Grid size independence study: Finger length ( $L_f$ ) on the left-hand side of the Y-axis for different grid sizes (2  $\mu\text{m}$ , 3  $\mu\text{m}$  and 5  $\mu\text{m}$ ) on the X-axis at constant  $\beta = 0.62$ . Pressure drop in a microchannel on the right-hand side of the Y-axis for different grid sizes (2  $\mu\text{m}$ , 3  $\mu\text{m}$ , and 5  $\mu\text{m}$ ) on the X-axis when droplet interacts with the entrance of the bypass channel at constant  $\beta = 0.62$ . .....34

**Figure 2.4 :** (a) Comparison between dimensionless droplet length observed in experiments and model presented by Garstecki et al. [52]. The solid line is the curve showing the predicted droplet size. (b) Mother droplet length Vs Number of experiments. ....35

**Figure 2.5:** High-speed visualization of the droplet interaction with the entrance of the bypass channel showing the transition from no droplet breakup to droplet break up at different time intervals. Results are plotted for three cases of  $\beta$ . (a)  $\beta = 0.48$  (b)  $\beta = 0.77$  (c)  $\beta = 0.91$ . Capillary number is kept almost constant in all cases ( $Ca = 0.0028 \pm 0.0002$ ). .....37

**Figure 2.6:** High-speed visualization of the droplet interaction with the entrance of a bypass channel showing the transition from no droplet breakup to droplet break up at different time intervals showing the effect of  $Ca$  (a)  $Ca = 0.0022$  (b)  $Ca = 0.005$  (c)  $Ca = 0.037$ . The ratio of channel width  $\beta$  is kept constant in all cases ( $\beta = 0.48$ ). .....38

**Figure 2.7:** Comparison between experimental and computational work at  $\beta = 0.48$  and  $Ca = 0.005$ . (a) High-speed visualization of the droplet interaction with the entrance of a bypass channel. (b) Computed contours of the volume fraction of water. (c) Isometric view of the iso-surface of the volume fraction of water at 0.5.....39

**Figure 2.8:** Comparison between experimental and computational work at  $\beta = 0.63$  and  $Ca = 0.007$ . **(a)** High-speed visualization of the droplet interaction with the entrance of a bypass channel. **(b)** Computed contours of the volume fraction of water. **(c)** Isometric view of the iso-surface of the volume fraction of water at 0.5.....40

**Figure 2.9:** **(a)** Regime map is showing contours of finger length ( $L_f$ ) on  $Ca-\beta$  plane. A dotted line is shown to demarcate regions of droplet breakup and no droplet breakup. **(b)** Regime map showing contours of  $V_{ratio}$  on  $Ca-\beta$  plane. ....42

**Figure 2.10:** **(a)** Dimensionless daughter droplet volume as a function of the capillary number showing equivalent squeezing and dripping regime. The dotted line shows the squeezing regime given by Menech et al. [53] and a dash-dot line showing current work. **(b)** Contours of shear stress at different  $Ca$  in the equivalent dripping regime. ....44

**Figure 2.11:** Evolution of finger length and  $\varepsilon$  with time. Finger Length ( $L_f$ ) plotted on the left-hand of Y-axis and  $\varepsilon$  on the right-hand side of Y-axis Vs. stages of droplet interaction (evolution with time).....45

**Figure 2.12:** Schematic of the droplet interacting with the T-junction. Zoomed in view shows pressure notations inside and outside the droplet.....46

**Figure 2.13:** Evolution of average shear stress with time for  $Ca$  ranging from equivalent squeezing to the dripping regime. Contours at the top of the figure show average shear stress and corresponding stage of droplet interaction for given computed value. ....47



**Figure 2.14:** Evolution of pressure built up with time for Ca ranging from equivalent squeezing to the dripping regime. Contours at the top show pressure built up and corresponding stage of droplet interaction for given computed value. ....48

**Figure 2.15:** Evolution of  $(F_R + F_T)$  and  $F_Y$  during various stages of the droplet interaction with the T-junction of the bypass channel. (a) Forces acting on the trapped droplet. (b) The case of droplet breakup. (c) Case of no droplet breakup. ....50

**Figure 3.1:** Conceptual depiction of selective droplet breakup using microvalves at two locations. (a) The “mother” droplets are generated at upstream T-junction (not shown) and, as they pass down the main channel, interacts with the first and second junctions positioned adjacent to valves 1 and 2. When the valves are off, operating conditions are chosen such that no droplet breakup occurs at these junctions. (b) When the first valve is pressurized and deforms, the selected droplet breaks up and a small droplet enters the side branch, here it is depicted that a sample of the green and red fluids are selected, subsequently these can be passively merged in the branch (c) Similarly, the second valve also allows selective break up such that different reactions can be initiated in its merging station. The result is a system in which a range of reaction permutations can occur between different reagents. ....56

**Figure 3.2:** Grid size independence study showing finger length ( $L_f$ ) vs minimum grid size ( $\Delta S$ ) for droplet interaction with the first and second junction. ....59

**Figure 3.3:** A schematic of microfluidic system design with upstream droplet generation section followed by two stage droplet division section. Mother droplets are produced upstream and are made to interact with identical droplet division junctions. ....60

**Figure 3.4:** High-speed visualization, at a capillary number ( $Ca$ ) of 0.01, of a mother droplet interacting with the (a) first and (b) second junctions. In which a finger is seen to develop in the branch and either break into a droplet or retract. The discrepancy, between the two junctions, of the maximum length of the finger length (c) and the (d) percentage of the volume of the mother droplet which breaks into a daughter droplet is seen across the  $Ca$  range tested. ....61

**Figure 3.5:** The Resistance network of the microfluidic system with the associated flow rate distribution of the continuous phase, without considering the resistance of the droplets. ....62

**Figure 3.6:** A schematic of a microfluidic system with upstream droplet generation section followed by droplet division section, designed such that the behaviour at each splitting junction is balanced. To achieve this the second junction consists of a section of channel with the original width, followed by an expansion which drops the overall resistance of the branch. ....64

**Figure 3.7:** High-speed visualization of droplet interaction with straight channel branching from the first junction and the expansion channel stemming from the second junction. Five regimes are observed: (a) No droplet breakup in both junctions, (b) Breakup in the first junction, (c) Breakup in first junction onset of breakup in the second junction, (d) Breakup in both the junctions. (e) Intermittent breakup in both the junctions. ....66

**Figure 3.8:** The finger length for four regimes of droplet interaction is plotted against  $Ca$ . The finger length from regime e (intermittent breakup regime) is not plotted as it is

not consistent across each droplet. The dots below the regime letters indicates whether breakup at the first (red) and second (green) junction occurs. ....67

**Figure 3.9:** The evolution of finger length measured in the first and second junction for both the designs (symmetric and expansion channel) as a function of time under the same flow conditions ( $Ca = 0.0055$ ). Case of symmetric design second junction yields no breakup while all other cases represent breakup. ....68

**Figure 3.10:** High-speed visualization of droplet interacting with the first T-junction and expansion channel, which yields the same volume of daughter droplets at both the junctions. This lies between regime 3 and 4. ....68

**Figure 3.11:** Comparison between experimental and 3D numerical simulations at  $Ca = 0.011$ . (a) Contours of the volume fraction of the continuous and discontinuous phase. (b) High-speed visualization of the droplet interaction with the first and second junction. ....69

**Figure 3.12:** Percentage efficiency of droplet breakup in the first junction against deformation at the entrance of the first junction calculated using numerical simulations. Bottom inset shows a top view of the 3D numerical simulation without deformation at the entrance of first junction resulting in no breakup. The top inset shows a top view of the 3D numerical simulation with deformation of  $50\mu m$  at the entrance of first junction resulting in a breakup. ....70

**Figure 3.13:** Percentage efficiency of droplet breakup in the second junction and expansion channel against deformation near the entrance of the second junction calculated using numerical simulations. Bottom inset shows a top view of the 3D

numerical simulation with deformation of 60 $\mu$ m for symmetric second junction resulting in no breakup. The top inset shows a top view of the 3D numerical simulation with deformation of 60 $\mu$ m for expansion channel resulting in a breakup.....71

**Figure 3.14:** High-speed visualization showing the interaction of droplets with two junctions in the presence and absence of valve actuation. (a) Actuation of valve for the first junction (b) Actuation of the valve for the second junction with the valve away from the entrance of second junction (c) Actuation of the valve for the second junction with the valve at the entrance of second junction (d) Actuating both the valves simultaneously. ....73

**Figure 3.15:** Percentage efficiency of droplet breakup vs valve deformation for (a) first junction (b) second junction with two valve locations.....74

**Figure 4.1:** Schematic of the microfluidic device to achieve selective droplet splitting and merging at multiple locations using eight single-layer microvalves. The microfluidic device generates four different coloured droplets mimicking four different chemicals in the upstream part of the chip, this is achieved using four valves located close to each of the channels carrying discontinuous phases. A zoomed-in view shows that downstream of the generation structures, there is a multiple site splitting and merging section of the chip. Here, the droplet can be split at any of four different locations each controlled by a separate microvalve, after splitting the daughter droplets are merged using a passive pillar-based approach. ....78

**Figure 4.2:** Working principle of multi-splitting and multi-merging system. (a) The resistance network of a system considering the flow rate and hydrodynamic resistance of

each branch without consideration of the presence of droplets in the system. **(b)** Schematic of the simplified microfluidic system in which same flow rate enters in four T-junctions with different width. **(c)** Schematic of the actual microfluidic system in the presence of four merging chambers designed in such a way that same flow rate enters in four T-junctions with a similar width.....80

**Figure 4.3:** Droplet generation part of the multi-splitting and multi-merging system using two different approaches. **(a-d)** Valve based droplet generation approach is used to create a red, blue, white, and green droplet, respectively. Scale bars, 100  $\mu\text{m}$ . **(e)** Schematic shows all the four valves are used sequentially to generate droplets following the order of the numbers that are written next to them. **(f-i)** Pressure based droplet generation approach which is used to generate blue, red, green, and white droplets, respectively. Scale bars, 100  $\mu\text{m}$ . .....83

**Figure 4.4:** Generating droplets in different orders using a valve and pressure-based approach. **(a)** Blue and green droplets are generated, alternately. **(b)** Green and green droplets are generated, one after the other. **(c-d)** Four different coloured droplets are produced, sequentially. Scale bar is 100  $\mu\text{m}$ . .....85

**Figure 4.5:** Different Regimes of droplet splitting when droplets interact with four junctions placed one after the other. **(a)** Droplets split in all the four junctions. **(b)** Droplets split in the last three junctions. **(c)** Droplets split in the last two junctions. **(d)** There is no droplet splitting in all the four junctions: scale bars, 100  $\mu\text{m}$ . .....87

**Figure 4.6:** Classification of different splitting regimes by the separation distance and the percentage of the flow rate entering each junction. **(a)** Schematic shows the separation

distance  $d_1$ ,  $d_2$ ,  $d_3$ ,  $d_4$ . Regimes map is extracted based on (b) the average separation distance in each branch of the main channel, and (c) the percentage of the flow rate entering each branch divided by the total flow rate in the main channel, respectively. The dotted lines separate splitting and no splitting regimes.....88

**Figure 4.7:** Characterisation of the single-layer microvalve. **(a)** Maximum deformation of the channel is plotted against different pressures that are applied to the single-layer valve. **(b)** Deformation of the channel is plotted against the time when the single-layer valve is fully pressurised to the pressure of 1800 mbar and fully depressurised, respectively. **(c)** Image sequence showing selectivity of the droplet breakup, red droplet arrives at the second junction and do not break at this junction, just before the second droplet arrives at this junction valve is actuated to break the droplet. Before the third droplet arrives at this junction valve is deactivated, and droplet does not split. ....89

**Figure 4.8:** Splitting of different coloured droplets at different locations using single-layer microfluidic valves. **(a)** Percentage of the relative daughter droplet volume against the deformation of the microchannel channel for all the four junctions. **(b)** The blue coloured droplet is split at the first junction when the valve is pressurised at 1800 mbar (deformation of 53  $\mu\text{m}$ ). **(c)** Splitting of the red coloured droplet at the second junction using valve pressurised at 1800 mbar. **(d)** Droplet splitting of the green coloured droplet at third junction using valve pressurised at 1800 mbar. **(e)** The white coloured droplet is split at the fourth junction when the valve is pressurised at 1800 mbar. ....91

**Figure 4.9:** Splitting of different coloured droplets occurs whilst the valve is actuated. The two daughter droplets are merged within the chamber, the first being retarded by the pillar structures, after merging the total volume is such that the droplet is dragged out of

the merging chamber. Merging of two different coloured droplets an equal volumetric ratio is shown at the (a) third and (b) first junctions. In the former, a single red daughter droplet is merged with a single clear one. For the latter two blue daughter droplets are merged with two clear droplets, Finally, (c) merging of an unequal number of droplets generated from two different samples is achieved, such that the mixing ratio is 1:2 (red: clear).....92

**Figure 4.10:** Image sequence demonstrating the merging of two different selected droplets (one clear and one red droplet) at the third junction. The clear droplet is split by transient actuation of the valve, resulting in the deposition of a daughter droplet in the merging chamber. Subsequent clear droplet pass without splitting due to timely deactivation of the valve. Finally, a single red droplet is selected and split, again a daughter droplet is formed and merges with the clear daughter droplet. ....93

## List of Tables

<b>Table 1.1:</b> Variation of Laplace pressure, the pressure of the continuous and discontinuous phase during four stages of droplet breakup. ....	11
<b>Table 2.1:</b> Grid-independence test. Error in $\Delta P$ and $L_f$ are compared with the finest grid (2 $\mu\text{m}$ ). ....	34
<b>Table 3.1:</b> Grid size independence study showing error in finger length ( $L_f$ ) compared to the finest grid. ....	59



# Nomenclature

Symbols	Definition
$Ca$	Capillary Number
$Pe$	Peclet Number
$Bo$	Bond Number
$We$	Weber Number
$\mu$	Viscosity of the continuous phase ( $Pa.s$ )
$v$	Velocity of the continuous phase ( $\mu m/s$ )
$\gamma$	Interfacial tension ( $N/m$ )
$\Delta P$	Laplace Pressure ( $Pa$ )
$r$	Radius of curvature ( $\mu m$ )
$w$	Width of the microchannel ( $\mu m$ )
$h$	Height of the microchannel ( $\mu m$ )
$u_{gap}$	Velocity of the continuous phase in a gap between wall and a droplet. ( $\mu m/s$ )
$\varepsilon$	Gap between microchannel wall and a droplet interface ( $\mu m$ )
$Q_c$	Flow rate of continuous phase ( $\mu L/min$ )
$Q_d$	Flow rate of discontinuous phase ( $\mu L/min$ )
$P_c$	Pressure of continuous phase ( $Pa$ )
$P_d$	Pressure of discontinuous phase ( $Pa$ )
$\Delta S$	Grid size ( $\mu m$ )
$L_f$	Finger length ( $\mu m$ )
$\Delta t$	Time step in simulations ( $s$ )
$\beta$	The ratio of width of bypass channel to main channel

$V_{ratio}$	The ratio of daughter droplet volume to mother droplet volume
$F_R$	Resistance to the flow of continuous phase ( $\mu N$ )
$V_d^*$	Dimensionless daughter droplet volume
$P_h$	Pressure in head of the droplet ( $Pa$ )
$P_t$	Pressure in tail of the droplet ( $Pa$ )
$d$	Separation distance ( $\mu m$ )

### Subscript

$b$	Bypass channel
$m$	Main channel
$c$	Continuous phase
$d$	Discontinuous phase

### Superscript

$*$	Dimensionless quantity
-----	------------------------



# Chapter 1

## 1 Introduction

The development of soft lithography techniques for microfabrication has increased interest in fluid flow at the microscopic level [1,2]. Microfluidics attracted the attention of research fields ranging from engineering, biology, chemistry, and physics, making it an interdisciplinary research area. It is an adaptable tool for a range of applications due to advantages like micro to nanolitre scale fluid consumption resulting in a decrease in the cost of samples/reagents, decrease in the overall size of the setup, high surface area to volume ratio, fast reactions, and high throughput analysis. Microfluidics promises to exceed the overall performance compared to conventional equipment used for general laboratory procedures like mixing, pipetting, centrifugation, and incubation with inexpensive microchips or lab on chip (LOC) devices.

A subset of microfluidics is droplet-based microfluidics [3,4] or digital microfluidics, which involve generation and manipulation of droplets of nL to fL volume size. Monodisperse droplets can be generated in an immiscible carrier fluid at rates of more than 20 kHz [5,6]. Droplets generated are separated by immiscible carrier fluid, which in turn provides physical and chemical isolation to each droplet and avoids cross-contamination. Different samples, reagents, and cells can be encapsulated in a droplet allowing various screening and selection processes [7]. These microsystems allow control of each droplet volume, precise and reliable droplet manipulation; hence each droplet can be considered as the microreactor which can be transferred, mixed, and analysed at multiple locations [8]. Due to these advantages, droplet-based microfluidics finds application in reaction kinetics [9], protein crystallisation [10,11], clinical diagnostic [12,13], single-cell analysis [14], microparticle synthesis [15,16], clinical and biological assays [17,18], inorganic chemistry [19], and high throughput screening [20–24]. While droplet production is rapid and highly repeatable, there is a need to control and manipulate the droplet via generation, breakup, sorting, merging, mixing, and trapping within the microfluidic circuits.

### 1.1 Droplet Generation

The first step for any droplet-based microfluidic device is the precise and controlled generation of monodisperse droplets. Droplet generation is achieved mostly through passive techniques

without any external actuation or source of energy. However, for selectivity, few researchers used active techniques of droplet generation as well. There are three critical geometries for generating droplets passively, namely T-junction, flow-focusing and co-flow devices. Moreover, some researchers also demonstrated active methods like pneumatic microvalves, surface acoustic waves and electric field for on-demand and selective generation of droplets. The generation of droplets is also categorised based on the mechanism into three regimes: squeezing, dripping, and jetting regime with different forces dominating each regime. Here, we first discuss microfluidic geometries used for droplet generation, regimes, and droplet generation mechanism.

## 1.1.1 Device geometries

### 1.1.1.1 T-junction

T-junctions are the most commonly used geometries for droplet generation. Two immiscible fluids, continuous/carrier fluid and discontinuous/dispersed fluid contact each other orthogonally to produce monodisperse droplets, as shown in **Figure 1.1 (a)**. This geometry was used for the first time by Thorsen *et al.* [25] to generate stable droplets. The droplet size, frequency of generation and separation distance between droplets in a T-junction are determined by flow parameters like flow rate of two fluids, interfacial tension, Capillary Number and dimensions of the geometry. The continuous and discontinuous fluids are carried to the junction by two separate channels; when interacting, they form an interface at the junction. Over the time the small portion of the discontinuous phase enters the main channel, further elongation of the head of the discontinuous phase occurs until the neck thins out. Eventually, a droplet is generated from the discontinuous fluid.

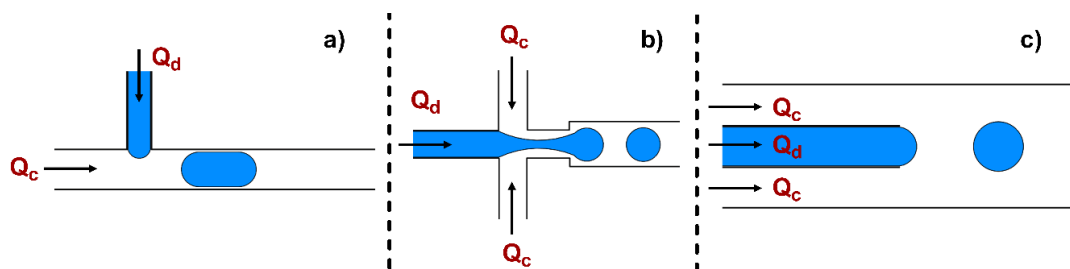


**Figure 1.1:** Schematic showing geometries for droplet generation (a) T-junction, (b) flow-focusing geometry, and (c) co-flow geometry. Here  $Q_c$  represents the flow rate of the continuous fluid, and  $Q_d$  represents the flow rate of the discontinuous fluid.

### 1.1.1.2 Flow-focusing

In flow-focusing devices, the discontinuous fluid is broken into droplets by two streams of continuous fluid, as shown in **Figure 1.1 (b)**—two streams of continuous fluid shears stream of dispersed phase which causes controlled and stable droplet formation. Anna *et al.* [26] first proposed flow-focusing geometries. Compared to T-junction, flow-focusing geometries are more complicated to operate, as they involve a total of three fluid streams. Still, they offer enhanced monodispersity and control over the volume of droplets. These geometries are preferred while working with the biological samples and can produce smaller droplets with greater control. Flow parameters that govern the droplet production are viscosity and the flow rates of two phases. There are many variations of flow focusing geometries developed based on the application for which they are used.

### 1.1.1.3 Co-flowing

In co-flow geometries, continuous and discontinuous fluid streams flow parallel to each other, with two streams of the continuous phase bordering the discontinuous phase on both sides. This results in a thinning of the discontinuous phase thread, and ultimately the formation of droplets, as shown in **Figure 1.1 (c)**. Umbanhowar *et al.* [27] demonstrated the use of co-flow devices for the first time. The physics of flow-focusing devices and co-flow devices are similar.

## 1.1.2 Active Methods of Droplet Generation

Passive methods of droplet generation can produce droplets of similar size continuously, but they do not deliver on the aspect of selectivity or on-demand nature of droplet production. In studies where it is often necessary to change the volume of samples/reagents active methods of droplet generation are attractive, as they offer additional control over droplet production. Active methods of droplet generation utilise an external actuation or source of energy for droplet generation rather than just relying on the channel's geometric configuration. Though the addition of active droplet generation techniques to the microfluidic chip adds the complexity and cost of the device, it does provide extra control over a range of parameters and offer on-demand droplet generation in chemical and biological screening processes. Several researchers demonstrated the use of active methods [28] like single/ multi-layer pneumatic microvalves [29–31], surface acoustic waves (SAW) [21,32–34], dielectrophoretic [35–39],

electro-wetting [40–42], thermal actuation [43–47] and magnetic actuation [48–51] successfully for droplet generation.

Abate *et al.* [31] used single-layer pneumatic microvalves for precise control of size, and frequency of droplets generated in the flow-focusing device. Two microvalves are placed close to the flow-focusing junction. The authors demonstrated that without the actuation of valves, droplets are generated in specific size and frequency for a particular flow rate of continuous and discontinuous phase, as shown in **Figure 1.2 (a-h)**. When valves are pressurised systematically, a broad range of droplet sizes with different frequencies can be produced without changing the flow rates. Schmid *et al.* [33] used surface acoustic waves (SAW) near the flow-focusing junction for droplet generation. The authors demonstrated that the size of the droplet formed could be controlled at will by changing the power of SAW. The size of the droplets produced is inversely proportional to the power of SAW while the frequency of droplet generation is directly proportional to the power, as shown in **Figure 1.2 (i)**. In the subsequent work, authors [34] extended their study in T-junction in a squeezing regime. Collins *et al.* [32] used SAW to produce on-demand picolitre-sized droplet. The volume of the droplet generated can be varied by parameters like applied power, time for which SAW is actuated, and geometric configuration.

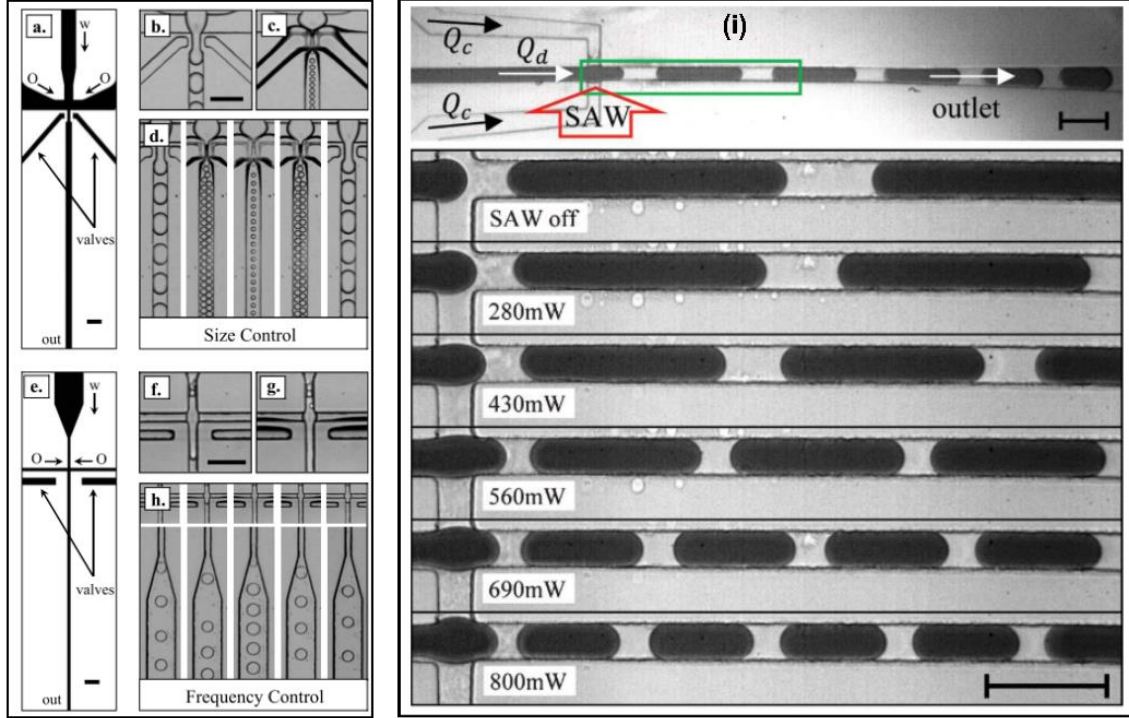


**Figure 1.2:** Active methods of droplet generation (a-h) Single-layer microvalves for control of droplet size and frequency in a flow-focusing device [31]. (i) Application of SAW near the flow-focusing junction for controlling droplet size [33]. Reproduced from ref. 31 and 33 with permission.

### 1.1.3 Mechanism of Droplet Generation

Two theories are proposed to explain the mechanism of droplet generation in a microfluidic system, namely ‘*shear driven droplet generation*’ proposed by Thorsen *et al.* [25], and ‘*rate of flow controlled generation*’ proposed by Garstecki *et al.* [52]. Before discussing the details of these two theories, it is essential to understand the dimensionless numbers and forces acting on the droplet during generation.

#### 1.1.3.1 Important Dimensionless Numbers in Droplet Microfluidics

Various dimensionless numbers play an important role in droplet formation; these dimensionless parameters are explained below.

##### 1.1.3.1.1 Capillary Number

The Capillary Number represents the relative effect of viscous forces against the interfacial tension between the two immiscible fluids. Mathematically, the Capillary Number is given as,



$$Ca = \frac{\mu \cdot V}{\gamma} \quad 1.1$$

Where  $\mu$ ,  $V$ , and  $\gamma$  represents dynamic viscosity, the velocity of the continuous fluid and interfacial tension between two immiscible phases (continuous and discontinuous phase), respectively[[53]]. Generally, for applications involving microchannels and microfluidic droplet generation, the Capillary Number is small (less than 0.1), hence it indicates that capillary forces are more dominant than viscous forces.

#### 1.1.3.1.2 Peclet Number

The Peclet number is the ratio of advection transport rate to diffusion transport rate of a particular physical quantity (for example heat, mass). Mathematically, the Peclet Number is given by,

$$Pe = \frac{\text{Advection transport rate}}{\text{Diffusion transport rate}} \quad 1.2$$

$$Pe = \frac{L u}{D}$$

Where  $L$  represents the characteristics length,  $u$  represents the velocity of the continuous phase, and  $D$  represents the diffusion coefficient.

#### 1.1.3.1.3 Bond Number

The bond number is the ratio of body forces versus surface tension forces.

$$Bo = \frac{\Delta \rho g L^2}{\sigma} \quad 1.3$$

Where  $\Delta \rho$ ,  $g$ , and  $\sigma$  represents the density difference between the two phases (continuous and discontinuous phase), gravity, and interfacial tension between two phases, respectively. Bond Number plays a crucial role in determining the shape of a droplet moving in the microfluidic system. For a Bond Number less than 1, the shape of the droplet in the microfluidic system is approximately spherical.

#### 1.1.3.1.4 Weber Number

The Weber number shows the relative strength of inertia forces and the surface tension forces.

$$We = \frac{\rho v^2 l}{\sigma} \quad 1.4$$

If the Weber number is greater than one, it indicates that inertia forces dominate over surface tension forces. For droplet generation in microfluidic systems, capillary forces typically dominate inertia forces; hence the value of Weber Number is less than 1.

### 1.1.3.2 Forces Acting during Droplet Generation

#### 1.1.3.2.1 Interfacial Force

Interfacial tension depends on the Laplace pressure jump ( $\Delta P$ ) across the droplet interface, which is mathematically given by,

$$\Delta P = \gamma \left[ \frac{1}{r_a} + \frac{1}{r_r} \right] \quad 1.5$$

Where  $r_a$  is the radius of axial curvature and  $r_r$  is the radius of radial curvature,  $\gamma$  is interfacial tension between two immiscible phases. The radial curvature bound by the height of microfluidic system while the radius of axial curvature is equal to the width ( $w$ ) of the microfluidic channel upstream and half of the width downstream ( $w/2$ ), as shown in **Figure 1.3**.

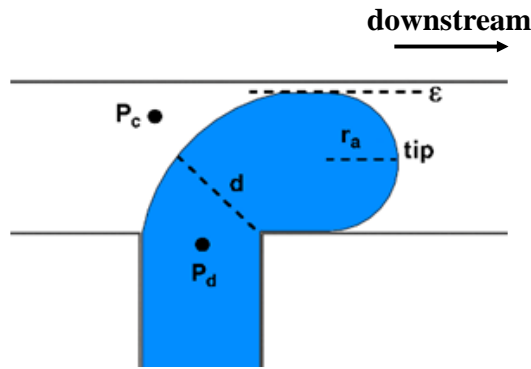


**Figure 1.3:** A schematic representation of the shape of the discontinuous phase entering the main channel, which is carrying a continuous phase just before the droplet generation.  $P_c$  and  $P_d$  represent hydrodynamic pressure in the continuous and discontinuous phase, respectively.

The Laplace pressure jump upstream and downstream is calculated as follows[54],

$$\Delta P_{upstream} = \gamma \left[ \frac{1}{w} + \frac{2}{h} \right] \quad 1.6$$

$$\Delta P_{downstream} = -\gamma \left[ \frac{2}{w} + \frac{2}{h} \right] \quad 1.7$$

The negative sign in equation 1.7 represents that the force is acting in the opposite direction, adding above two equations and multiplying it by the cross-section area gives the interfacial force[54].

$$F_\gamma = -\gamma h \quad 1.8$$

In the absence of any other force acting on the discontinuous phase, the interfacial force acts as a stabilizing effect resisting the process of droplet breaking up from the stream of discontinuous fluid.

### 1.1.3.2.2 Shear Force

The shear stress acting on the tip of the discontinuous phase is calculated by using the velocity of the continuous fluid ( $u_{gap}$ ) in the gap between the droplet and the channel wall as follows,

$$u_{gap} = \left[ \frac{Q_{continuous\ phase}}{h \cdot \varepsilon} \right] \quad 1.9$$

Where  $\varepsilon$  represents the gap between the droplet and the microchannel wall, we can assume with reasonable accuracy that the flow rate of the continuous phase supplied through the inlet of the main channel is equal to that in  $\varepsilon$ . Shear stress is calculated as [52]

$$\tau \approx \left[ \frac{\mu u_{gap}}{\varepsilon} \right] \quad 1.10$$

Putting the value of  $u_{gap}$  in the above equation, we get

$$\tau \approx \left[ \frac{\mu Q_{carrier\ phase}}{h \cdot \varepsilon^2} \right] \quad 1.11$$

The shear force on a droplet tip at a T-junction is given as,

$$F_\tau \approx \frac{\mu Q_{carrier\ phase}}{\varepsilon^2} \times w \quad 1.12$$

The shear force calculated above is an overestimation since, we assume that the discontinuous phase tip is static in the main channel; whilst the nature of the discontinuous phase tip is dynamic.

### 1.1.3.2.3 Resistance to the Flow of Continuous Fluid

The blocking effect due to the presence of the discontinuous phase tip in the main channel gives rise to the resistance to flow. We can use the Hagen-Poiseuille or thin-film equation to

calculate the pressure drop caused due to this resistance to the flow using the value of  $\varepsilon$ . When the value of  $\varepsilon$  is of the order of  $w$ , we can use Hagen-Poiseuille equation

$$\Delta p \approx \frac{\mu \cdot Q_{\text{continuous phase}} \cdot w}{h^2 \cdot \varepsilon^2} \quad 1.13$$

If  $\varepsilon \ll w$ , we can use the pressure drop equation for thin film,

$$\Delta p \approx \frac{\mu \cdot Q_{\text{continuous phase}} \cdot w}{h \cdot \varepsilon^3} \quad 1.14$$

$$F_R = \Delta p \cdot h \cdot w \quad 1.15$$

$$F_R = \frac{\mu \cdot Q_{\text{continuous phase}} \cdot w^2}{h \cdot \varepsilon^3} \quad 1.16$$

From the above equations, we observe that value of  $F_t$  and  $F_R$  are inversely proportional to  $\varepsilon$ . When  $\varepsilon \ll w$ ,  $F_t > F_R$  [52]. In the process of droplet generation, stabilization is provided by interfacial force while the other two forces are destabilizing (assisting droplet generation) in nature.

## 1.1.4 Available Models of Droplet Generation

There are different models available for explaining the scaling and mechanism of the droplet generation. Out of these models, two are used widely. First one proposed by Thorsen *et al.* [25], which is commonly known as a '*shear driven model*' and the second one is proposed by Garstecki *et al.* [52], which is commonly known as a '*rate-of-flow-controlled*' droplet generation. In the following subsection, we will discuss these two models.

### 1.1.4.1 Shear Driven Droplet Generation

Thorsen *et al.* [25] carried out several experiments by varying the pressure of water and oil, to investigate the droplet generation in microfluidic T-junction. The authors observed that the size of the droplets formed depend on the geometry of device and pressure/flow rate of two fluids used. When the pressure of the oil (continuous phase here) is much higher than that of the water (discontinuous phase here), there is no droplet generation. As the pressure of the water becomes comparable to that of the oil, droplet generation starts. Based on the ratio of oil and water, droplets of the different sizes and separation distances are formed.

According to this theory, droplet generation is caused by the competition between capillary and shear forces. The volume of the droplet formed in the T-junction is determined by equating the Laplace pressure with the shear force acting the tip of the discontinuous phase and droplet is generated when shear force overcomes the Laplace pressure.

$$\Delta p \sim \frac{\mu u_{gap}}{\varepsilon} \quad 1.17$$

$$r \sim \frac{\gamma \varepsilon}{\mu u_{gap}} \quad 1.18$$

$$\therefore r \sim \frac{\gamma}{\mu \dot{\varepsilon}} \quad 1.19$$

Where  $r$  is the radius of droplet formed and  $\dot{\varepsilon}$  is the shear rate.

#### 1.1.4.2 Rate-of-flow Controlled Droplet Generation

This mechanism of droplet generation is given by Garstecki *et al.* [54]. According to this mechanism, droplet generation at the T-junction is governed by flow rate or the pressure of continuous ( $P_c$ ) and discontinuous ( $P_d$ ) fluids used as shown in **Figure 1.4**. The process of droplet generation consists of four stages, namely 1) the small portion of discontinuous phase enters the main channel. 2) The discontinuous phase starts to occupy the cross-section of the main channel. 3) The neck of the discontinuous phase starts to become thinner and thinner. 4) The droplet separates from the discontinuous phase and moves in the main channel.

It is necessary to understand what happens with  $P_c$  and Laplace pressure ( $\Delta P$ ) during these four stages, while  $P_d$  is assumed to remain constant. Laplace pressure (equation 1.5) decreases in the first two stages of droplet generation; this is because the height of the system bounds the radial curvature while axial curvature tends to increase till the third stage. Hence Laplace pressure is maximum just before the droplet is breaking from the discontinuous phase. During the first stage ( $P_d - \Delta P > P_c$ ), which forces the discontinuous phase to enter the main channel. However, during stage two, three and four pressure in the continuous phase ( $P_c$ ) continues to increase due to blockage of the continuous fluid. Hence  $P_c - (P_d - \Delta P)$  becomes maximum in the fourth stage, which causes droplet getting separated from the discontinuous phase. Variation of different pressures during four stages is shown in **Figure 1.4 (a-e)** and **Table 1.1**.

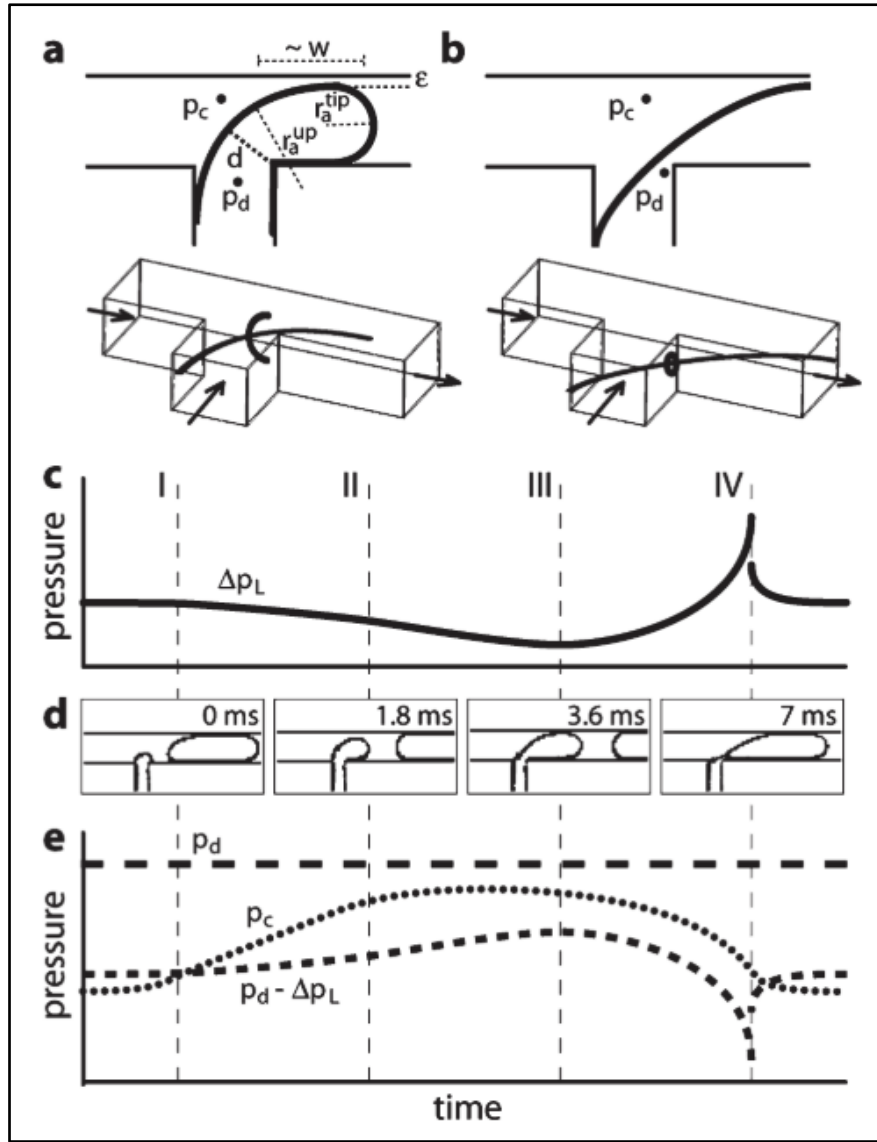


**Figure 1.4 :** Variation of  $P_c$ ,  $P_d$  and  $\Delta P$  during droplet generation at T-junction [54]. (a-b) Pressure acting on a droplet along with radius of curvature. (c-e) Variation of pressure acting on a droplet during different stages of droplet generation. Reproduced from ref. 54 with permission.

	$P_d$	$P_c$	$\Delta P$	$P_c - (P_d - \Delta P)$
<b>Stage 1</b>	Constant	Constant	Decreases	Negative value
<b>Stage 2</b>	Constant	Increases	Decreases	Positive value
<b>Stage 3</b>	Constant	Increases	Decreases	Positive value
<b>Stage 4</b>	Constant	Increases	Increases	Maximum value

**Table 1.1:** Variation of Laplace pressure, the pressure of the continuous and discontinuous phase during four stages of droplet generation.

With the help of above analysis, Garstecki *et al.* [52,55] came up with the scaling relation for determining the size of the droplet formed in T-junction of a microfluidic system,

The velocity of the continuous phase is given by,

$$u_c \approx \frac{Q_{continuous\ phase}}{h \cdot w} \quad 1.20$$

While the velocity of the droplet can be given as,

$$u_d \approx \frac{Q_{discontinuous\ phase}}{h \cdot w} \quad 1.21$$

The final length of the droplet is equal to

$$L = \left[ w + \frac{d \cdot u_d}{u_c} \right] \quad 1.22$$

$$\frac{L}{w} = \left[ 1 + \alpha \left( \frac{Q_{discontinuous\ phase}}{Q_{continuous\ phase}} \right) \right] \quad 1.23$$

### 1.1.5 Regimes of Droplet Generation

Interaction of the discontinuous phase with the continuous phase has been investigated several times by researchers based on the flow conditions and type of droplets formed. They observed three different regimes of droplet generation, namely squeezing, dripping, and jetting regime and how different theories of droplet generation explain these regimes.

Menech *et al.* [53] observed that at the low capillary Number ( $Ca < 0.01$ ), resistance to the flow of the continuous phase is a most critical factor in the formation of a droplet, known as the squeezing regime. In this regime, as the discontinuous fluid tip enters the main channel, pressure in the continuous phase continues to increase until the discontinuous phase completely blocks the main channel. The time duration of this blocking stage is called  $T_{block}$ . As the flow of continuous phase is blocked completely, it squeezes the neck of discontinuous phase till droplet breaks up into the main channel and pressure changes abruptly. This time duration is called as  $T_{squeeze}$ . When  $Q_c \gg Q_d$ , blocking time is more than the squeeze time and vice versa. In this regime, stabilising force is interfacial tension while destabilising force is due to building up of the pressure. In squeezing regime, the shear force plays the least important role compared to the other two forces. This regime is best explained by ‘*rate-of-flow-controlled*’ droplet generation.

As the Capillary number increases ( $Ca > 0.02$ ), the size of the droplet formed decreases compared to the squeezing regime. The changes in the pressure of the continuous phase decrease drastically, and significant contributing force for the droplet formation comes from

both shear force and resistance to the flow of continuous phase. This regime is termed the dripping regime. In the dripping regime, the discontinuous phase does not entirely block the main channel. The gap between the droplet and the microfluidic wall is significant compared to that of the squeezing regime. Thorsen *et al.* [25] gave the mechanism of droplet formation in this regime. However, the size of the droplet predicted by the shear driven breakup model is consistently over predicting the actual size of droplets formed in experiments, because pressure effects which were considered negligible compared to the shear force also significantly contribute to the droplet formation. The presence of shear force and force due to resistance to the flow, makes prediction of the droplet size in this regime complicated compared to the squeezing regime. When Capillary Number is increased further droplet generation point moves consistently forward and instead of droplets stream of discontinuous phase flows downstream parallel to the continuous phase. This regime is termed the jetting regime.

After discussing various aspects of droplet generation, the generated droplet is manipulated in a microfluidic system. The next section will cover the most crucial droplet manipulation technique, which is known as droplet breakup and sorting used for dividing the droplet in required volume at the desired location on a chip.

## **1.2 Droplet Breakup and Sorting**

The volume of the droplets generated using geometries like T-junction and co-flow is on the higher side. These generated droplets carrying samples and reagents are delivered to the required location on-chip using a manipulation technique called droplet breakup. Based on the application where it is used, droplets can be subdivided into symmetric or asymmetric daughter droplets. Droplet breakup techniques can be categorised as active or passive droplet breakup. Active methods use an external source of energy like surface acoustic waves, microvalves to achieve selective or non-selective droplet breakup. In contrast, passive droplet breakup methods use change in geometry instead of an external source of energy to achieve droplet breakup. In the section below, we explain different methods used to achieve droplet breakup.

### **1.2.1 Use of Channel Geometry**

Use of channel geometry to achieve droplet breakup is a passive tool in microfluidics. Droplets can be subdivided at different locations using these simple, inexpensive methods with less control in terms of selectivity and volume of the daughter droplet formed. Link *et al.* [56] used



two geometries 1) Successive T-junctions to subdivide the large droplet into symmetric smaller daughter droplets (shown in **Figure 1.5 a-j** and **m**) and 2) obstacles placed in a channel, where the location of the obstacle determines the ratio in which a droplet is subdivided ( **Figure 1.5 L**). Link *et al.* found out that there exists a critical capillary number above which droplet always breaks and is given as  $Ca = \alpha \varepsilon_0 \frac{1}{(\varepsilon_0^{2/3} - 1)^2}$  where  $\alpha$  is a constant determined using viscosity contrast of the fluids,  $\varepsilon_0$  is the initial extension of the droplet. Critical Capillary number is validated with the experimental results and found to be in good agreement with the experiments. Furthermore, the authors plotted the regions of the breakup and no breakup on a parameter map featuring the Capillary number and initial extension of the droplet. With this understanding, Link et al. used the series of three T-junctions to break the droplet symmetrically into eight daughter droplets, as shown in **Figure 1.5 m**.

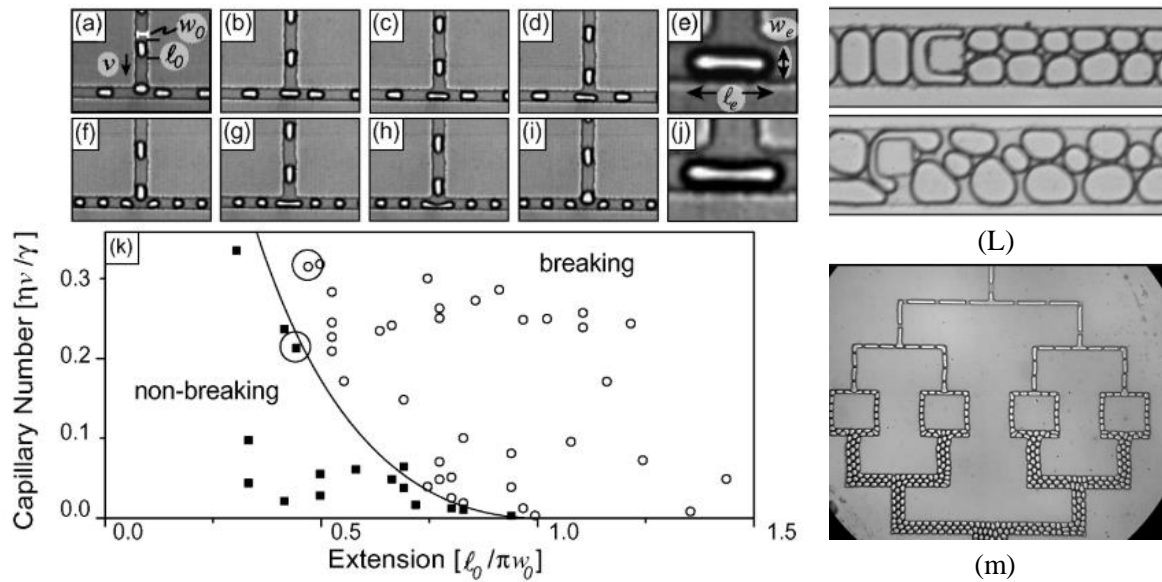


**Figure 1.5:** (a-j) Image sequence from Link *et al.* [56] showing droplet interaction with T-junction with the width of the channel ( $w_0$ ), length of the droplet ( $l_0$ ), and velocity ( $v$ ) shown. (k) Regime map showing breakup and non-breakup regimes plotted on extension Vs. Capillary Number. Reproduced from ref. 56 with permission.

Ménétrier-Deremble and Tabeling [57] used asymmetric junctions connecting at an arbitrary angle to the main channel carrying mother droplets (**Figure 1.6 d**). The authors observed that when droplet interacts with such junctions, there are three possible outcomes, namely direct breakup, retarded breakup, and no breakup. In direct breakup, when the mother droplet interacts with the junction, the finger length of the droplet formed in the secondary channel continues to

increase, and eventually, the droplet breaks up creating a daughter droplet (**Figure 1.6 a**). Here, the term finger length refers to the maximum portion of the mother droplet that enters the secondary channel. In retarded breakup, the mother droplet enters the junction, but here, with time the finger length of the droplet starts to decrease, yet still break up occurs (**Figure 1.6 b**). Finally, in the no breakup case, the mother droplet enters the junction, then over the time it retreats, hence the finger length decreases, resulting in no droplet breakup (**Figure 1.6 c**). The authors concluded that there exists a critical value of finger length above which droplet breakup occurs while below that finger length no droplet breakup takes place.

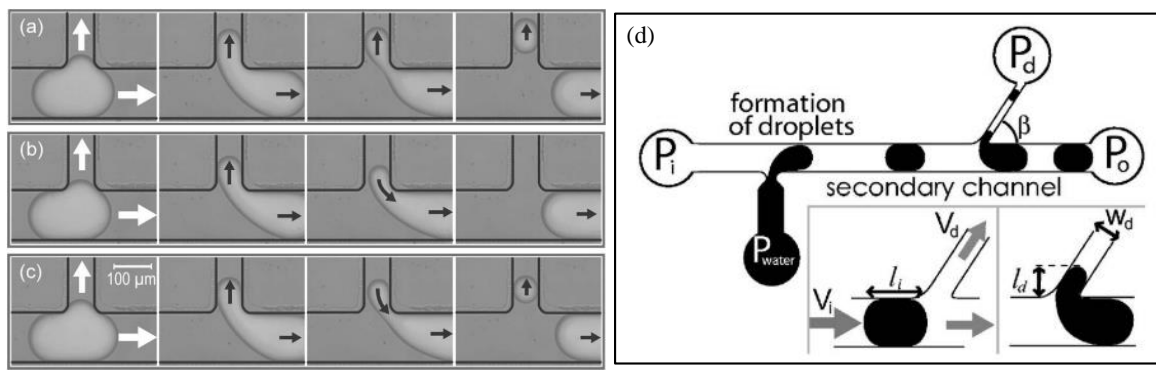


**Figure 1.6:** Image sequence from Ménétrier-Deremble and Tabeling [57] showing outcomes of droplet interaction with the T-junction (a) Direct breakup (b) No breakup (c) Retarded breakup. (d) The geometry used for experiments. Reproduced from ref. 57 with permission.

The phenomenon of droplet breakup in a range of moderate ( $10^{-3}$ ) to large ( $10^{-1}$ ) capillary number is widely described in the literature, but there are very few studies that focus on the low capillary number range. Jullien *et al.* [58] extended the range of capillary number compared to the previous studies, covering from  $4 \times 10^{-4}$  to 0.2. The authors identified three regimes of droplet breakup. In the first regime, there is no droplet breakup. In the second regime a gap is formed between the droplet and wall of the microchannel, and finally in the third regime, the droplet completely obstructs the flow of continuous phase before the droplet breakup occurs.

In addition to experimental work, some studies use numerical simulations to explain the physics of droplet breakup in microfluidic systems[59]. Hoang *et al.*[60] used full three-dimensional numerical simulations and stop-flow simulations to investigate the droplet breakup at T-junction in a microfluidic system. The authors concluded that the breakup process consists of two steps, in the first step the droplet deforms due to an externally applied flow while in the second step, surface tension driven pinching occurs which is related to externally

applied flow. The second step of breakup starts when the curvature at the neck of the droplet exceeds the curvature everywhere else. It depends strongly on the aspect ratio of the geometry while weakly depends on the capillary number and viscosity ratio of fluids. De Menech [61] used a phase-field model for investigation of droplet breakup in T-junction. The results of the phase-field model are validated with experimental work and are found to be good agreement, showing that phase-field models can be used for two-phase microfluidics system. The author concluded that the breakup of the droplet in T-junction depends on the viscosity ratio of the continuous and discontinuous phase. Leshansky *et al.* [62] used 2D numerical simulations with simple geometric construction to explain droplet breakup in T-junction. The authors explained the role of critical droplet extension in droplet breakup using lubrication in the gap of droplet and channel wall.

Even though passive methods of droplet breakup/sorting are cheap and straightforward, they do not provide the desired control required for chemical and biological applications. In the next sections, we will discuss active methods (electrical, thermal, acoustic, and pneumatic actuation) of droplet breakup and sorting on a microfluidic chip.

### 1.2.2 Use of Electric Actuation

The channel geometries used for droplet breakup/sorting discussed in the previous section when incorporated with an external source of energy changes the outcome of droplet interaction with a secondary channel from no breakup to break up or no sorting to sorting, thus providing more control. Some studies use electric [63–67], magnetic and thermal actuation to change droplet breakup behaviour when required. Link *et al.* [63] used an electric field to achieve droplet breakup. The authors applied the electric field to simple T-junction to achieve asymmetric droplet breakup or sorting of the droplets. In the absence of an applied electric field when the droplets arrived at the junction, they split into the bifurcating junction randomly, however, when the electric field is applied to one of the branch droplets entered that branch. The volume of the droplet breakup can be controlled by an electric field applied at the junction—this method provided a contact-free way of droplet breakup and sorting, which is a requirement of screening processes. Ahn *et al.* [64] used an electric field to charge the droplets (either positive or negative) and later sort these droplets in one of the three channels (shown in **Figure 1.7 a and b**). In the absence of electric field, droplets preferred the central channel, but in the presence of a stable electric field, they were sorted in the selected channel. Some studies

used dielectrophoretic [68,69], electric capacitance [70] and fluorescence activated [71,72] droplet sorting.

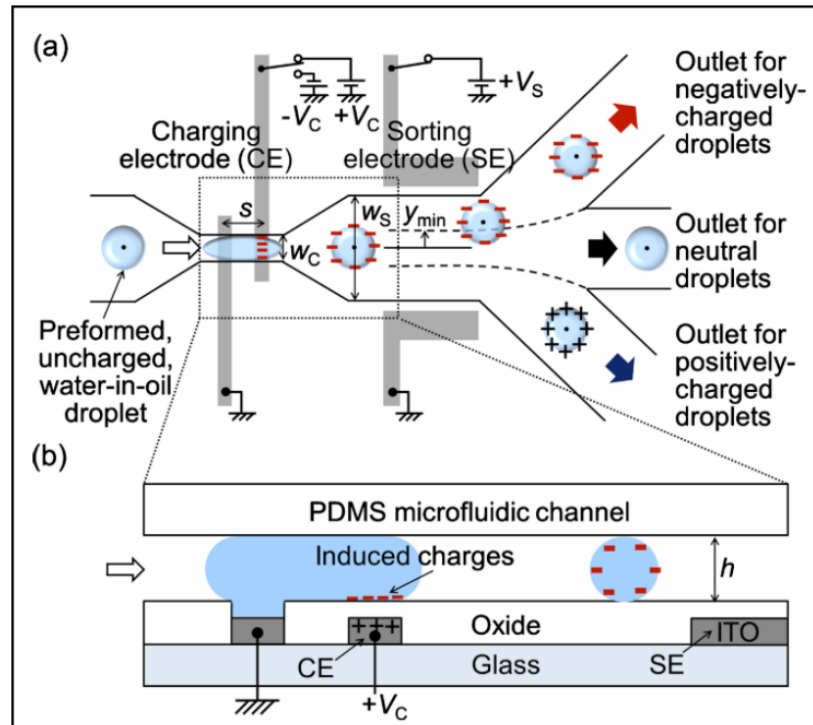


**Figure 1.7:** Working principle of the device which uses an electric field for sorting based on the polarity of the droplets [64]. Droplets are sorted in one of the three outlets shown. Reproduced from ref. 64 with permission.

### 1.2.3 Use of Thermal Actuation

Some studies have used thermo-capillary forces, induced due to localized application of laser [73,74] to manipulate droplet behaviour. Baroud *et al.* [74] used a localised laser to block the path of the droplet by acting as a thermo-capillary valve hence showing a way to sort the droplets actively. In an extension of this study, the authors [73] demonstrated different droplet manipulations like droplet generation, merging, asymmetric breakup and sorting with the help of focused laser beams in combination with passive method (so utilising the change in geometry shown in **Figure 1.8 a and b**). To achieve droplet breakup, authors used obstacle placed at the bifurcating junction, which divided the incoming droplet symmetrically in the absence of laser. When a laser beam on one side of the obstacle is turned on, it caused the flow on that side to be reduced or stopped wholly, depending on the power applied, resulting in the asymmetric breakup or sorting of the droplet.

Ting *et al.* [75] used the surface tension gradient created by thermal effects to break the droplet asymmetrically or sort the droplet in one of the secondary channels. The micro heater is placed in one of the secondary channels, as shown in **Figure 1.8 c**. In the absence of the heater being activated, droplets were divided symmetrically in both the secondary junctions. However, when heater temperature is gradually increased from 25 degrees to 40 degrees, droplet divides asymmetrically in the bifurcating junction and volume of the daughter droplet formed in the secondary channel with heater is higher than without heater. When the heater temperature is increased further to 55 degrees, the droplet completely enters the secondary channel with the integrated heater as plotted in **Figure 1.8 c**; hence droplets are sorted from above the heater temperature of 40 degrees.

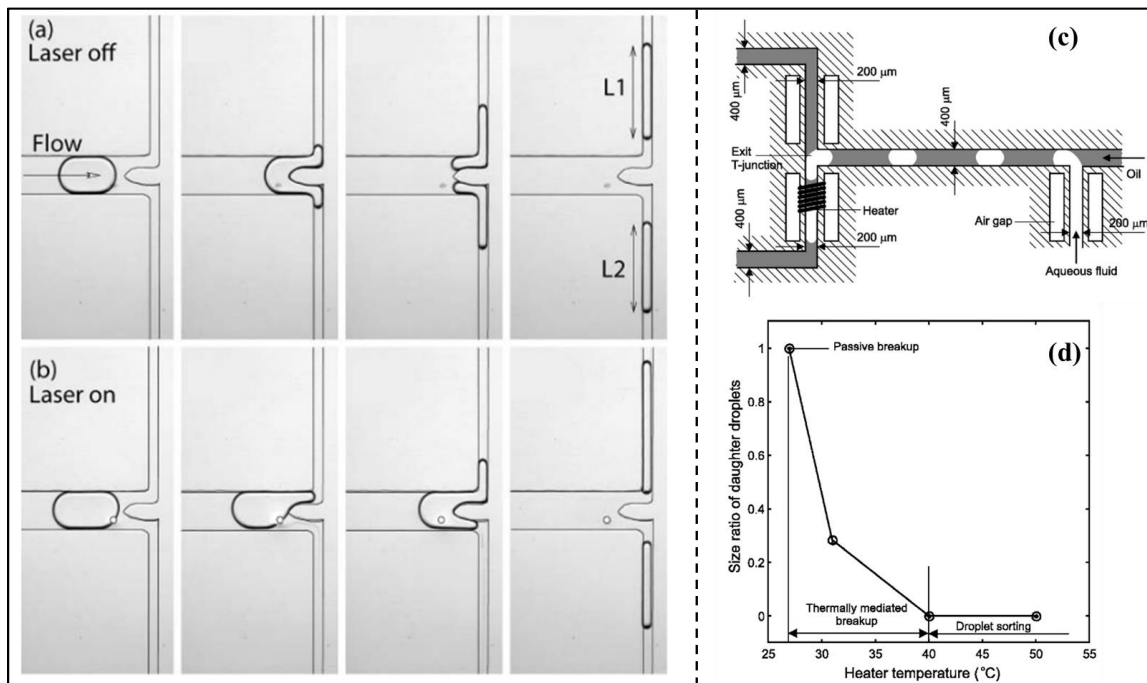


**Figure 1.8:** Laser [73] and microheater [75] induced droplet breakup. (a) Symmetric mother droplet breakup in both the branches in the absence of laser. (b) Asymmetric mother droplet breakup when the laser is turned on. The branch in which laser is turned on results in smaller daughter droplet volume. (c) Schematic showing micro heater placed on one side of the simple bifurcating junction resulting in droplet being completely sucked on the side of the channel integrated with microheater. (d) Micro heater temperature is plotted against the size of daughter droplet formed showing different regimes of droplet breakup. Reproduced from ref. 73 and 75 with permission.

#### 1.2.4 Use of Surface Acoustic Waves (SAW)

Surface acoustic waves (SAW) are generated by interdigital transducers (IDT) which are fabricated on the surface of piezoelectric material. The IDTs consists of electrodes, the dimensions of which determine the resonance frequency of the device. In these devices,

acoustic forces are used for droplet manipulation. Surface acoustic waves [76–81] are used widely for droplet breakup and sorting due to its bio-compatible nature.

Franke *et al.* [76] used SAW for sorting of the droplets in two channels, as shown in **Figure 1.9 a**. In the absence actuation of SAW, droplets were sorted into the channel with lower hydrodynamic resistance; however, when SAW is actuated, the acoustic force pushes the droplet into the channel with higher hydrodynamic resistance, which results in the sorting of droplets. Sesen *et al.* [77] used SAW for asymmetric droplet breakup and sorting of droplet plug. In the absence of SAW actuation, droplets interacting with the Y-junction divides equally into two branches. Authors demonstrated, with actuation of the SAW, droplet plug can be divided asymmetrically into two daughter droplets, and even an entire plug can be sorted into one of the branches. The volume of droplet divided in each branch is directly proportional to the power of the surface acoustic wave, as shown in **Figure 1.9 b**. Sesen *et al.* [80] allowed the droplet to interact with the bypass channel of the microfluidic chip. The system is operated on the knife-edge where a slight change in flow condition can cause the outcome of droplet breakup or no breakup. In the absence of SAW actuation, there is no droplet breakup, however when SAW has actuated droplet breaks into the bypass channel and that too selectively as shown in **Figure 1.9 c**.

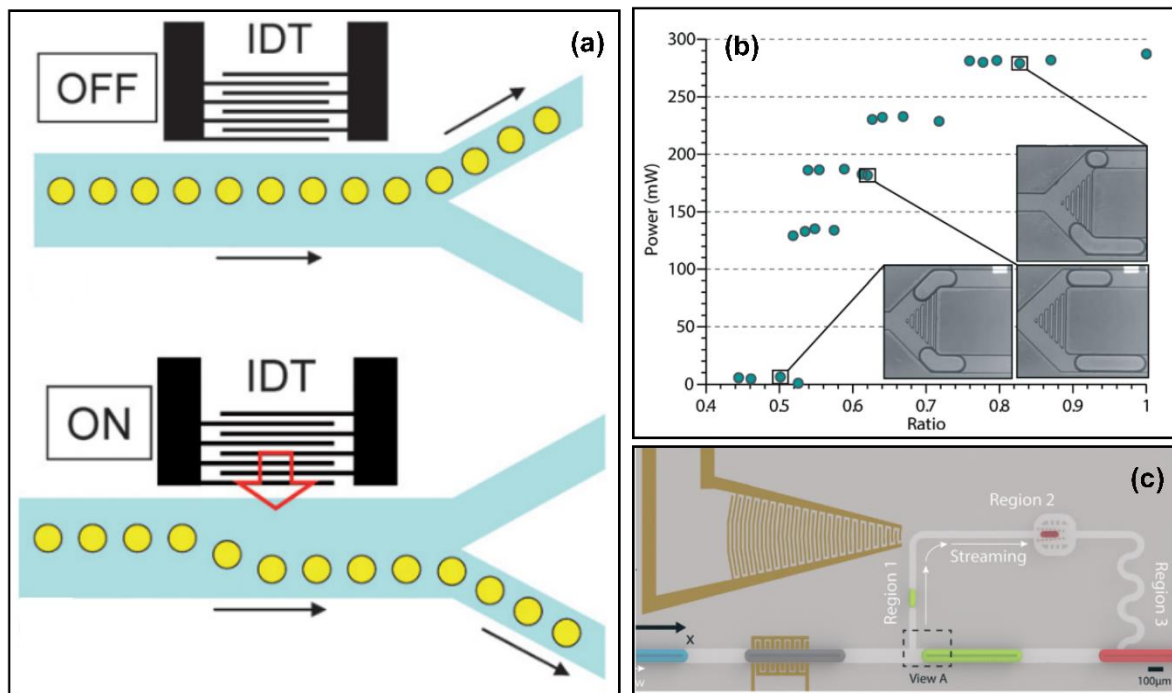


**Figure 1.9:** (a) SAW [76] used for sorting of the droplet, the first figure shows the path of a droplet when SAW is not actuated while the second figure shows the path of droplet after actuation of SAW. (b) Power supplied to SAW [77] plotted against the ratio of droplet division at Y-junction (c) SAW [80]

used for selective droplet breakup and merging at T-junction of a bypass channel. Reproduced from ref. 76,77 and 80 with permission.

### 1.2.5 Use of Pneumatic Microvalves

Microvalves offer flow control in a microfluidic system, either by providing on/off control of the flow or partially changing the flow conditions. In general, microvalves are classified based on the mean of actuation used. Microvalves most commonly use mechanical actuation [82–85], electrochemical actuation [86,87], pneumatic actuation [88–92]. However, pneumatic microvalves are simple to operate, cheap and can easily be incorporated in a microfluidic chip with soft lithography techniques and hence are compatible in droplet-based microfluidics; hence in this section, we will be discussing in detail about pneumatic microvalves used for droplet breakup and sorting [30,93–95].

Integration of pneumatic microvalves in microfluidic system fabricated by soft lithography process was demonstrated for the first time by Unger *et al.* [89]. Pneumatic microvalves consist of two flow channels, namely control channel and flow channel. Control channel is designed for carrying pressurised air or other fluid while the flow channel carries the primary fluid/droplets in the microfluidic system. Control and flow channel are separated from each other by a thin elastic membrane, and this elastic membrane is deformed by pressurised air to block the flow partially or entirely in the microfluidic system and thereby alter the flow conditions. Based on the soft lithography process used for the microfabrication, microvalves are broadly classified as single-layer microvalves, also called as horizontal microvalves and multilayer microvalves also called as vertical microvalves. In single-layer microvalves, both control and flow channel are fabricated in the same layer. In these valves the control and flow channel are separated by a membrane in same horizontal plane; hence they are also called as horizontal microvalves. On the other hand, in multilayer microvalves, the control channel is fabricated on the top of the flow channel using two or more layers of lithography, and they are separated by an elastic membrane hence called as vertical valves. When compared on the aspect of the simplicity of fabrication, the complexity of the microfluidic system and cost involved, single layer microvalves are more appealing than multilayer microvalves.

Abate *et al.* [96] used single-layer microvalve for droplet sorting at the bifurcating junction. In the absence of valve actuation, droplets always prefer secondary channel with lower resistance, when the valve is actuated droplets are sorted in the branch with higher

resistance and authors also demonstrated selectivity in sorting droplets, as shown in **Figure 1.10 (a,b,c)**. Yoon *et al.* [97] used two single-layer microvalves close to two branches of the bifurcating junction to achieve asymmetric droplet breakup and sorting. In the absence of valve droplets were divided in the same volume at the junction, while when one of the valves is actuated, it causes deformation of the secondary channel and thereby achieve asymmetric droplet breakup. When pressure is increased further, the deformed valve completely blocks the flow in a particular channel to cause droplet getting steered into another branch. Chen *et al.* [94] used multilayer valves to sort the droplets in three branches connected to three different outlets, as shown in **Figure 1.10 (d-h)**. Pneumatic microvalves are located on top of the flow channel on both the sides of the sorting area. In the absence of valve actuation, droplets were always sorted in the central channel, when the valve is actuated droplets were sorted either in the left or right side of the central channel based on which valve is activated.

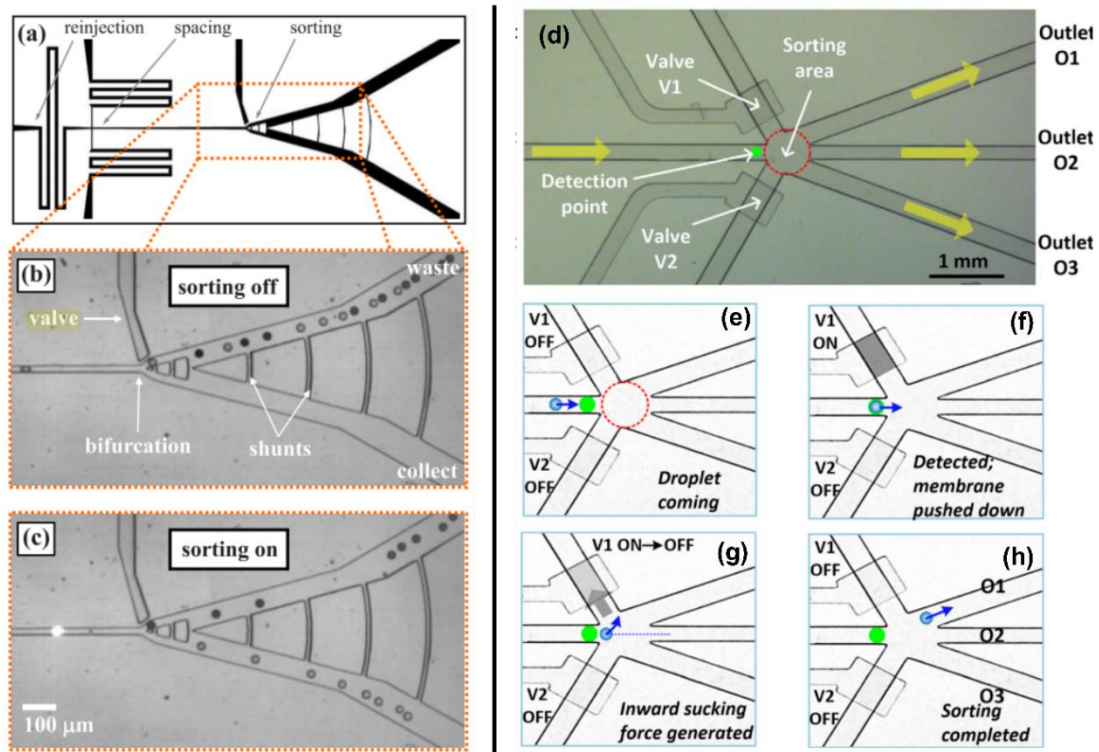


**Figure 1.10:** (a-c) Single-layer microvalve used for droplet sorting [96] at a bifurcating Y-junction. (d-h) Multilayer microvalve, in which control channel is located on top of the flow channel is used for droplet sorting [94]. Reproduced from ref. 96 and 94 with permission.

Single-layer microvalves are bio-compatible, cheap, and simple when compared to other active methods like electric control, SAW, thermal control. These advantages make single-layer microvalve ideal candidate for conducting chemical and biological screening processes on the



chip. Even though different microfluidic manipulation techniques like droplet breakup and merging are demonstrated with the help of single-layer microfluidic valves, integration of all these on the same chip with selectivity is missing.

In this PhD thesis, we demonstrate the integration of selective droplet generation, breakup and merging at multiple locations using multiple single-layer microvalves. To be specific, we demonstrate the use of single-layer valve to achieve selective droplet breakup at a bypass channel and two locations in the second and third chapter of the thesis, respectively. In the fourth chapter of the thesis, we integrate all the droplet manipulation techniques on the same microfluidic chip with the use of eight single-layer microvalves.

### 1.3 Droplet Merging and Mixing

For many chemical and biological applications [1,98], where reactions need to be performed within a droplet, merging and mixing of droplets plays an important role. When two droplets in a microfluidic system come close to each other, in the absence of surfactants, a film of continuous phase fluid prevents the droplet merging. As time passes, this film starts to thin and the two droplets can merge [99]. In the presence of surfactant, the time required for thinning out of the film increases due to stability of the droplets.

Droplet merging and mixing can be achieved by passive methods such as the addition of geometrical feature [100–105], pillars [106], changing the wetting property of the small portion of the channel [107] and promoting chaotic mixing using serpentine channels [108]. Passive merging of droplets is challenging in terms of control, to merge different droplets droplet generation frequency needs to be matched according to the need of application and geometrical feature used for merging. Niu *et al.* [106] used pillars for droplet merging. When droplets enter a merging chamber, which consists of pillars, their velocity decreases, and finally, it gets trapped in the chamber. A merging chamber can hold a specific volume of droplet. When the next droplet arrives in the chamber, it merges with the previous droplet and pillars cannot hold the volume of both the droplets, causing the merged droplet to exit the chamber as shown in **Figure 1.11 a**. Tan *et al.* [104] used a fusion chamber to achieve droplet merging. The fusion chamber is located at the trifurcating junction, the merging is achieved by taking into consideration the time required to drain the continuous fluid in between two droplets as shown in **Figure 1.11 b and c**. Authors showed merging of up to six droplets in this study.

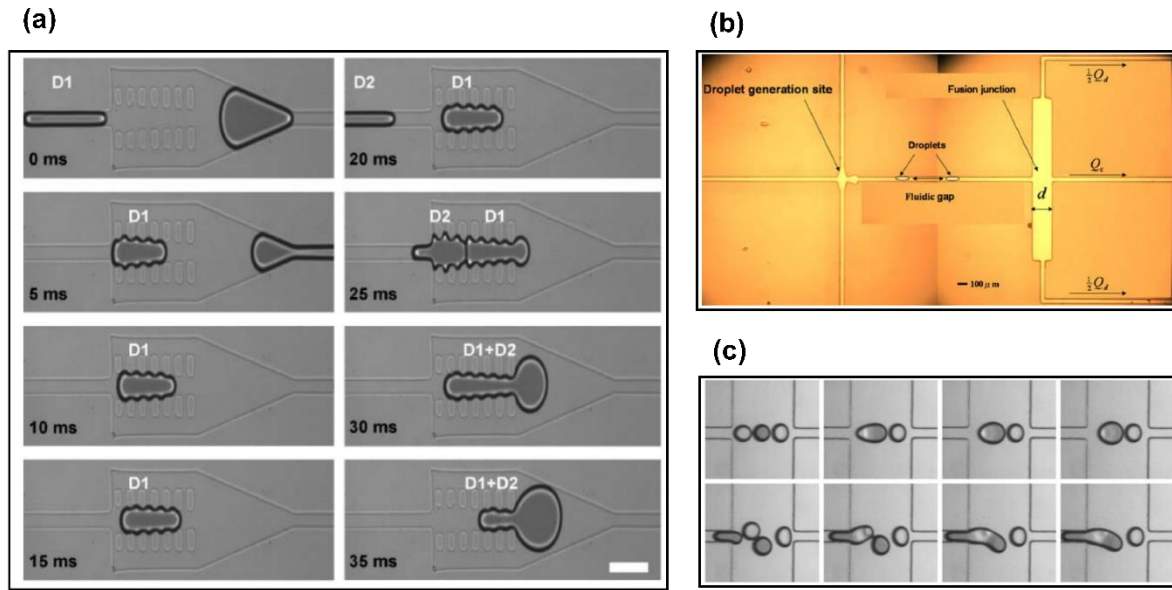


**Figure 1.11:** Passive methods to achieve droplet merging (a) Image sequence showing pillar induced [106] droplet merging. (b) Use of fusion chamber located at a trifurcating junction for droplet merging [104] (c) Image sequence showing merging of two and three droplets. Reproduced from ref. 106 and 104 with permission.

Droplet merging can also be achieved with better control but with the added complexity of using active methods such as electric field [63,109–112], surface acoustic waves (SAW) [80,113,114], microvalves [115], optical platforms [116] and thermal actuation [117]. Sesen *et al.* [113] used surface acoustic waves for an on-demand merging of droplets. The geometry consists of an expansion channel to slow down the droplet, and later stop the droplet movement by using acoustic force. The droplet is immobilised until the next droplet arrives in an expansion channel and merges with the previous droplet. The drag force of newly formed droplet overcomes the acoustic force, and the newly formed droplet is released from an expansion channel, as shown in **Figure 1.12 a**. Ahn *et al.* [111] demonstrated merging of two different sizes of droplets by application of the electric field, as shown in **Figure 1.12 b**. Two droplets of different sizes are produced by using two T-junctions. Due to the difference in velocities of smaller and larger droplets, smaller droplets catch up with larger droplets. Both these droplets are then merged using an electric field. Jamshaid *et al.* [115] used single-layer microvalves along with pillar to demonstrate droplet merging. Droplets are slowed down using pillar in a chamber, with actuation of microvalves any further movement of the droplet is restricted till the successive droplet comes and merges with the already trapped droplet. Finally, microvalve is deactivated to release newly-formed droplet after merging. Even though droplet merging here is achieved using single-layer microvalve, selectivity and merging different

composition of the droplet is not demonstrated. In this PhD thesis, we show the merging of droplets made from different materials with a combination of single-layer microvalve and pillars to show selectivity and different permutations and combinations required for performing different reactions on a chip.

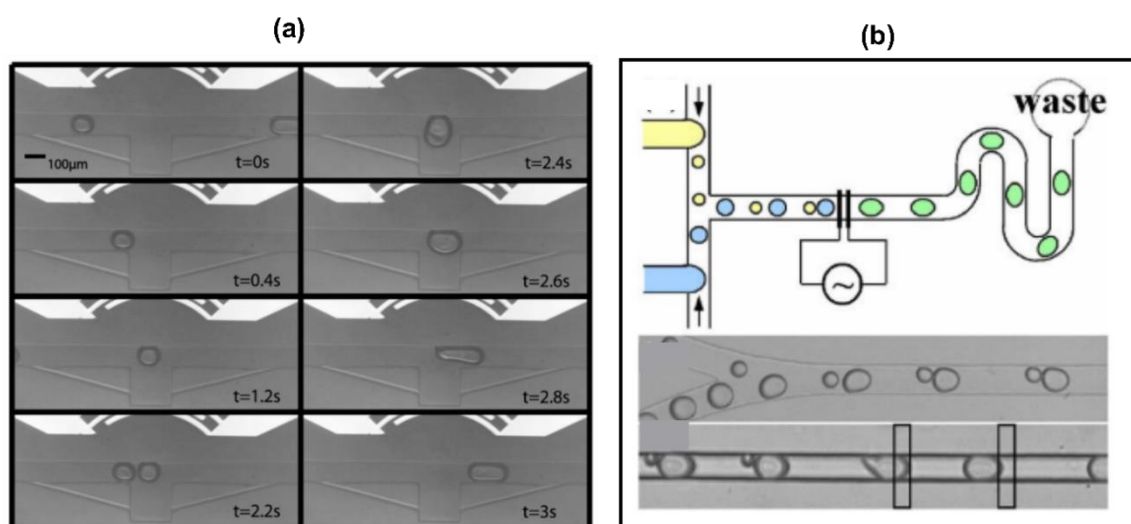


**Figure 1.12:** Active methods of droplet merging. (a) Use of surface acoustic waves and expansion channel to demonstrate on-demand merging of two droplets [113]. (b) Use of electric field to merge two droplets of different sizes [111]. Reproduced from ref. 113 and 111 with permission.

## 1.4 Scope and Objective of the Present Thesis

Droplet-based microfluidics is considered as the potential tool to bring high-throughput screening (HTS) on a microfluidic chip. Pharmaceutical industries use high-throughput screening (HTS) for drug research, in HTS target cells are tested against permutations and combinations of samples/reagents. For HTS on-chip, the system needs to perform different permutations and combinations of reactions on-chip. Droplet-based microfluidics is considered as the potential tool to bring HTS on a microfluidic chip. Different samples, reagents and cells can be encapsulated inside a droplet. As droplets are separated from each other by a buffer of the continuous phase, there is no cross-contamination chance. For permutations and a combination of reaction, droplet needs to be generated, split and merged at will or selectively. From the available literature, various active and passive methods are used for droplet manipulation. However, no study shows a combination of droplet generation, breakup, and merging with selectivity. Active methods previously used in the literature like electric force, surface acoustic waves, lasers have disadvantages, including cost, biocompatibility issues and

an overall increase in the setup complexity. To incorporate surface acoustic waves on a microfluidic chip, apart from traditional soft lithography on a silicon wafer and PDMS moulding, we need a lithium niobate wafer with interdigital transducers (IDTs) fabricated on it. To incorporate electric control on a chip, we need to fabricate electrodes on a microfluidic chip. This additional microfabrication increases the overall cost and adds extra complexity to the operation of a device. Therefore, in this PhD thesis, we propose the use of active (single layer horizontal pneumatic microvalve) and passive methods to demonstrate selectivity in droplet manipulation techniques. To be specific, we are going to investigate the droplet interaction with a bypass channel in terms of droplet breakup and no droplet breakup. Then follow it up with droplet interaction with two junctions and use of two microvalves to selectively break the droplet. Finally, using eight microvalves, we will demonstrate selectivity in droplet generation, breakup and merging for different permutations and combinations.

## **1.5 Organisation of the Thesis**

The rest of the thesis has been organized as follows:

### **Chapter 2 – Droplet Breakup in a Bypass Channel:**

This chapter studies droplet interactions with a T-junction, at the entrance to a bypass channel, using both experiments and numerical techniques. The regime map showing two different regimes of no droplet breakup and droplet breakup is plotted, which shows the knife edge separating the regimes.

### **Chapter 3 – Droplet Breakup Using Single-Layer Microvalves:**

We describe a microfluidic system for droplet breakup at two locations using a T-junction and expansion channel which are placed one after another. We observed five different regimes of droplet breakup when droplet interacts with both the junctions. We operated the system on the knife-edge separating regime of droplet breakup and no breakup at both the junctions. Later we used two single-layer horizontal microvalves placed close to two junctions to break the droplet at two locations selectively.

### **Chapter 4 – Controlled Droplet Manipulation Using Single-Layer Microvalves:**

This chapter demonstrates selective droplet generation, breakup and merging of different droplets at four junctions and merging chambers using eight single-layer horizontal microvalves. Compared to the last chapter, we added microvalves for selectivity in generating different kinds of droplets, later breaking them at four junctions and finally merging different droplets at four merging chambers.

## **Chapter 5 - Conclusions and future work:**

This chapter explains conclusions drawn from the three chapters above and presents the future scope of work.

# Chapter 2

## 2 Droplet Breakup at the Entrance of the Bypass Channel in a Microfluidic System

*We experimentally and numerically investigate breakup of a droplet at the entrance to a microfluidic bypass channel. The PDMS microchannels are manufactured using standard photolithography techniques, and we employ a high-speed camera to visualize the interfacial dynamics of the droplets. 3D numerical simulations are carried out for conditions causing both droplet breakup and non-breakup. The droplets are generated upstream of the bypass channel using a standard T-junction, the subsequent interaction with the entrance to the bypass channel is studied. In particular, the effects of capillary number ( $Ca$ ) and the relative width of the bypass channel with respect to the main channel ( $\beta$ ) are examined. The regimes of breakup and non-breakup are plotted on  $Ca$ - $\beta$  plane, experimentally, with the volume of the daughter droplets formed and the finger length in the bypass channel are also plotted on this regime map. There exists a critical value of  $Ca$  at constant  $\beta$  and a critical value of  $\beta$  at constant  $Ca$ , at which droplet breakup occurs. Combining measurements with numerical simulations, we show that the droplet breakup occurs if the hydrodynamic pressure drops across the droplet and average shear stress overcomes the differential Laplace pressure. We also found out that droplet breakup at the entrance to the bypass channel can exhibit squeezing and dripping regimes which are equivalent to those occurring in droplet generation at a T-junction.*

### 2.1 Introduction

Droplet microfluidics is finding widespread use in applications as diverse as drug discovery, clinical diagnostics, chemical synthesis, single-cell encapsulation, on-chip chemistry, and the production of microstructures [21,100,118–120]. Droplets are produced when two immiscible liquids, one of which acting as the continuous and other as the discontinuous phase, interact with each other in a microfluidic system [121–125]. Using different geometries droplets can be produced in a broad range of volumes ranging from fL to nL [6]. Droplets produced in the microfluidic system are isolated from each other by a buffer of the continuous phase, hence in

the paradigm of lab-on-a-chip, they can be viewed as analogous to test tubes at the laboratory scale. The presence of the continuous phase allows easy transport of the droplets around the microfluidic system.

While droplet production is rapid and highly repeatable, there is a need to control and manipulate the droplets' passage, behaviour within the microfluidic systems [21]. Techniques, to achieve this, are broadly classified as being either passive or active. Passive techniques require no external source of energy; instead, they control droplet outcomes through the use of changes in channel geometry [56,57,105,126], gravity [127] and surface properties [107]. Active techniques require an external source of energy through various means like the use of electric forces [64], dielectrophoresis [68,71], magnetic forces [128] or surface acoustic waves [33,34,129]. Acoustic actuation can also be used to produce individual droplets on demand and volume of the droplet can be controlled via the applied power [32] or producing small (fL) droplets [130]. Passive techniques cause the same outcome for each droplet, while the nature of active methods allows the possibility of bespoke interactions.

The physics of passive droplet generation at a T-junction displays three distinct regimes [53,131], namely 'squeezing' 'dripping' and 'jetting.' The squeezing regime has been reported to exist for  $Ca$  less than 0.015 when the width of the channels meeting at the T-junction is equal to each other [53,132,133]. A model was proposed by Garstecki *et al.* [52] to predict the length of the droplets formed:  $(l/w) = (1 + \alpha Q_{in}/Q_{out})$  where  $l$ ,  $w$ ,  $\alpha$ ,  $Q_{in}$  and  $Q_{out}$  are the length of the droplet, the width of the microchannel, a fitting parameter, the flow rate of the continuous and discontinuous phase, respectively. In the dripping regime, a droplet generation occurs when the shear force and pressure build-up, around the tip of the protruding discontinuous phase, become dominant over the interfacial force [25]. The range of Capillary number ( $Ca$ ) reported for this regime is  $Ca > 0.015$  [53]. Finally, a third regime exists, termed "jetting" in this regime the discontinuous phase extends downstream, and two phases move side-by-side in a laminar flow for a distance of a few channel widths downstream.

After droplet generation, there are studies, for investigating the conditions required for the subsequent divisions of the droplets at T-junctions. Link *et al.* [56] investigated the droplet breakup in a symmetric T-junction and demonstrated breakup of mother droplet into precisely controlled daughter droplets. Their analytical model shows that there exists a critical capillary number, and a critical initial extension of the mother droplet which indicated when droplet breakup would occur:  $\varepsilon_0 = l_0/(\pi w_0)$  is the initial extension where  $l_0$  and  $w_0$  are the length of the droplet and width of the channel, respectively. Menetrier-Deremble and Tabeling [57] experimentally studied the droplet breakup at the junction between microfluidic channels

which meet at various angles. They showed that when the droplet interacts with the asymmetric junction of arbitrary angles, three outcomes are possible, namely direct breakup, retarded breakup and no breakup. The authors proved that there exists a critical finger length, above which droplet breaks up. Subsequently, Jullien *et al.* [58] identified two regimes of the breakup for a droplet interacting with the symmetrical T-junction over a Capillary number range of  $4 \times 10^{-4} < Ca < 2 \times 10^{-1}$ . These two regimes were defined using the distance between the droplet and channel wall. In the first regime, there is a gap between the droplet and the microchannel wall, on the other hand, in the second regime, there is no gap between the droplet and microchannel wall, which obstructs the flow. Hoang *et al.* [60] used three-dimensional numerical simulations to investigate the droplet breakup in the symmetric T-junction and “stop-flow” simulations, in which droplet breakup was studied by switching off the flow in the simulations, causing the droplet breakup only by capillary effects. In doing so, they concluded that the droplet breakup occurs if the curvature of “neck” exceeds the value of curvature elsewhere on the interface of the droplet. In all the previous studies involving the interaction of a droplet at any junction, the outlet conditions of the two branches/channels are controlled externally to the microfluidic chip, either at a specified pressure or extracted flow rate.

In this chapter, we examine the droplet breakup at the entrance to a bypass channel in a microfluidic system. By this, we mean a secondary channel which branches from and then re-joins the main channel. Though the entrance to bypass channel is a T-junction, the flow conditions in each branch are dictated by conditions internal to the chip (the flow rate which occurs in each branch), the external control is limited to the outlet of the main channel. Bithi *et al.* [134] used a bypass channel to examine the dynamics of the droplet merging in microfluidic parking network. While, Sesen *et al.* [80] showed that by application of surface acoustic waves, a transition could be made between breakup and non-breakup of a droplet selectively at the entrance to a bypass channel. Though previous studies have offered significant clarity on the behaviour of a droplet at T-junction, the critical flow conditions for a bypass channel have not been explored previously. Here, we study breakup of a droplet during interaction with the entrance to a bypass channel and show the equivalence to the squeezing and dripping regimes using experimental and numerical methods and investigate the effect of the width of the bypass channel and Capillary number on the mechanism of droplet breakup.



## 2.2 Methodology

### 2.2.1 Experimental Methods

The microfluidic chips were fabricated from polydimethylsiloxane (PDMS) using standard photolithography techniques. First, we fabricate a mold for the microchannel on a 2-inch silicon wafer. The wafer was RCA cleaned, wet oxidized and a negative photoresist SU-8 (MicroChem, SU-8 2050) was spin coated on the wafer. The spin speed was adjusted based on the height of the microchannel needed. Further, the wafer was prebaked at 65 °C for 5 minutes and at 95 °C for 12 minutes. An iron oxide coated glass mask with a pattern of the microfluidic circuit (printed using Laser Writer, LW405, Microtech Inc) was aligned on the top of the spin-coated wafer using a mask aligner (Karl Suss, MJB4). The wafer was subjected to ultraviolet radiation with an intensity of 215 mJ/cm<sup>2</sup>, later post-baked at 65 °C for 4 minutes, at 95 °C for 10 minutes and allowed to cool in ambient. Subsequently, it was developed by SU8 photo developer for 10 to 15 min and cleaned with isopropanol. The wafer was kept on a hot plate at 120 °C for 10 min for hard-baking and allowed to cool in ambient. We poured a PDMS 10:1 mixture (Dow Corning, Sylgard 184) over the prepared mould and a 6:1 mixture was used for manufacturing a PDMS base slab on a glass slide. Both mixtures in the mould as well as in the base slab were baked in the furnace at 65 °C for about 30-40 minutes until they became sufficiently hard. The PDMS replica of the microfluidic circuit was peeled from the mould and was appropriately punched to make inlets and an outlet to the fluid channels. The patterned PDMS replica and PDMS base slab were bonded in an oven at 95 °C for 10-12 hours.

**Figure 2.1** shows a schematic of the experimental setup along with the microchannel geometry. The width of the main channel ( $w_m$ ), the width of inlet channel of the discontinuous phase ( $w_d$ ) and channel height ( $h$ ) are kept constant in all measurements at:  $w_m = 130 \pm 5 \mu\text{m}$ ,  $w_d = 65 \pm 3 \mu\text{m}$  and  $h = 60 \pm 3 \mu\text{m}$ . We vary the width of bypass channel ( $w_b$ ) over a range of six values:  $60 \pm 3 \mu\text{m}$ ,  $70 \pm 3 \mu\text{m}$ ,  $80 \pm 3 \mu\text{m}$ ,  $90 \pm 3 \mu\text{m}$ ,  $105 \pm 5 \mu\text{m}$  and  $120 \pm 5 \mu\text{m}$ . As such the values of  $\beta$  ( $w_b/w_m$ ) are  $\beta = 0.48, 0.54, 0.62, 0.77, 0.80$  and  $0.91$ , respectively. Deionized water was used for the dispersed phase, while for the continuous phase two types of oil were selected, these were silicone oil (50 cSt Sigma Aldrich Inc,  $\rho = 960 \text{ kg/m}^3$ ,  $\mu = 0.048 \text{ Pa-s}$ ) and paraffin oil (30 cSt, Merck Inc,  $\rho = 850 \text{ kg/m}^3$ ,  $\mu = 0.022 \text{ Pa-s}$ ). Both the water and oil flows were driven by a syringe pump (New Era pump systems Inc, USA). The range of flow

rates for both silicone oil and water were 0.24 to 16.4  $\mu\text{L}/\text{min}$  when used together. When paraffin oil and water were used together this range of flow rates became 0.24 to 1.64  $\mu\text{L}/\text{min}$ . We utilized high-speed visualization to record the interfacial dynamics of the droplet interacting with the entrance to the bypass channel. A high-speed camera (Motion Pro Y3, IDT Inc, USA) with a long-distance working objective (Qioptiq Inc., Germany) was used to capture images at 300 frames per second resolution of  $1280 \times 1024$  and a magnification such that the image is  $3 \mu\text{m}$  per pixel. The velocity and size of droplets (generated at a T-junction upstream of the bypass channel) were measured using image processing, with the latter estimated assuming the plug consists of a cuboid section and spherical caps at either end. The maximum uncertainty in the volume measurement is around  $\pm 2.8\%$ , considering an error of  $\pm 4$  pixels during length measurement by our image processing method. The volume of the daughter droplet formed after breaking up at the entrance to the bypass channel was measured by taking the difference between the volumes of the mother droplet, before and after the breakup.

A spinning drop tensiometer (Dataphysics Inc, SVT20) was employed to measure the surface tension for the water-oil system, yielding values of 38 mN/m and 30 mN/m for water-silicon oil and water-paraffin oil, respectively. The corresponding range of the capillary number ( $Ca = (\mu v_c / \gamma)$ ) in our measurements was 0.001 to 0.04, where  $\mu$ ,  $v_c$  and  $\gamma$  represent viscosity of the oil, velocity of the oil and surface tension for the oil-water system, respectively.

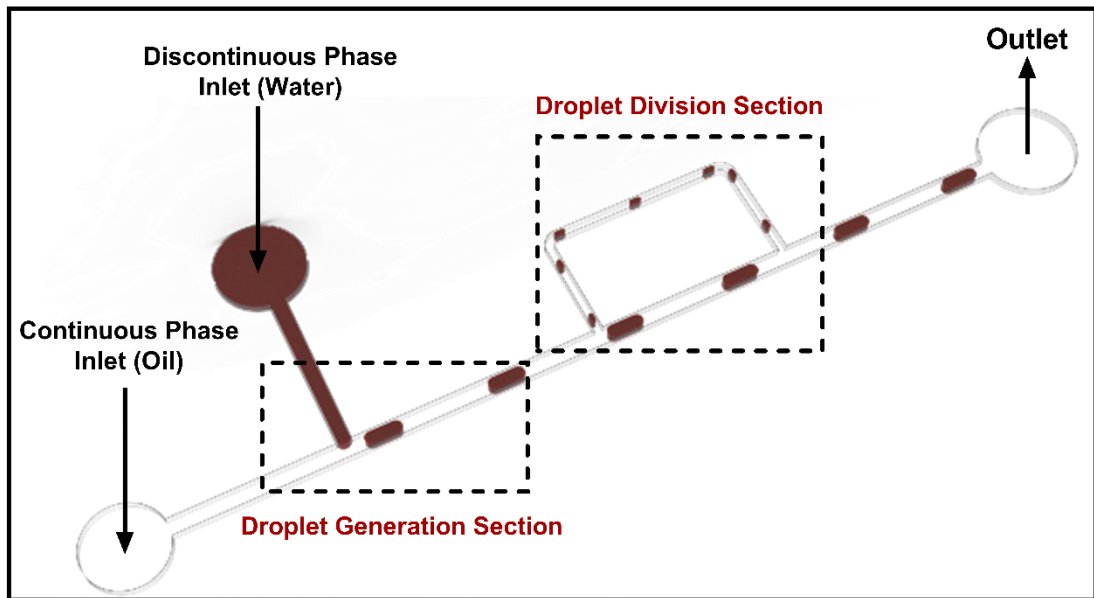


**Figure 2.1:** Schematic of the setup and geometry used in the present work. Both continuous and discontinuous phase are driven into the microfluidic system using two separate syringe pumps. Deionized water is the discontinuous phase, and oil (paraffin oil/ silicone oil) is the continuous phase.

### 2.2.2 Simulation Setup and Grid Size Independence Study

A commercial CFD software package (Fluent 15.0, ANSYS Inc, USA) was used to simulate the droplet behavior at the entrance to the bypass channel. Within the software, 3D Navier-Stokes equations were numerically solved using the finite volume method with the PISO (Pressure-Implicit with Splitting of Operators) scheme, and Volume-of-Fluid method was used for tracking the liquid-liquid interface. This was done using the computational domain shown in **Figure 2.2 a**. We did not simulate the generation of the droplets at upstream T-junction and used a single droplet in the main channel. A three-dimensional isometric view of the droplet just before the interaction with the entrance to the bypass channel is shown in **Figure 2.2 b**. The volume and velocity of a droplet ( $v$ ) generated at upstream T-junction were used as the input parameters for the simulation. At the inlet of the microchannel, a uniform velocity obtained from the experiments was imposed as a boundary condition. While, at the outlet of the microchannel the pressure was set to atmospheric. No slip conditions were applied to the walls of the microchannel.

A Cartesian structured mesh was generated using a commercial meshing software (ICEM, Ansys Inc). We used a uniform, structured Cartesian grid near the entrance to the bypass channel and a non-uniform grid with grid stretching is utilized away from the entrance to the bypass channel (**Figure 2.2 c**). A time step of  $\Delta t = 10^{-5}$  s was used in all simulations. The following properties of silicone oil and water were used in the simulations:  $\rho = 960 \text{ kg/m}^3$ ,  $\mu = 0.048 \text{ Pa-s}$ ;  $\rho = 1000 \text{ kg/m}^3$  and  $\mu = 0.00086 \text{ Pa-s}$ . The measured value of the contact angle of water-oil on PDMS from the recorded visualization of the droplet motion was around  $140^\circ$ , and we used this value in the simulation, assuming it as constant for a moving droplet.

**Figure 2.3** shows a grid size independence study for  $\beta = 0.62$  and  $Ca = 0.007$  for the three refinements at the entrance to the bypass channel:  $\Delta S = 2 \text{ }\mu\text{m}$ ,  $3 \text{ }\mu\text{m}$ , and  $5 \text{ }\mu\text{m}$ , where  $\Delta S$  is the minimum grid size in x, y and z directions. The finger length ( $L_f$ ) and pressure drop ( $\Delta P$ ) between two fixed points are plotted for the different grid refinements. The corresponding number of cells in these cases and the error with respect to the finest grid ( $\Delta S = 2 \text{ }\mu\text{m}$ ) are shown in **Table 2.1**. As the error in case 2 is just 0.16 % and 2 % for  $\Delta P$  and  $L_f$ , respectively,  $\Delta S = 3 \text{ }\mu\text{m}$  was used in the simulations.

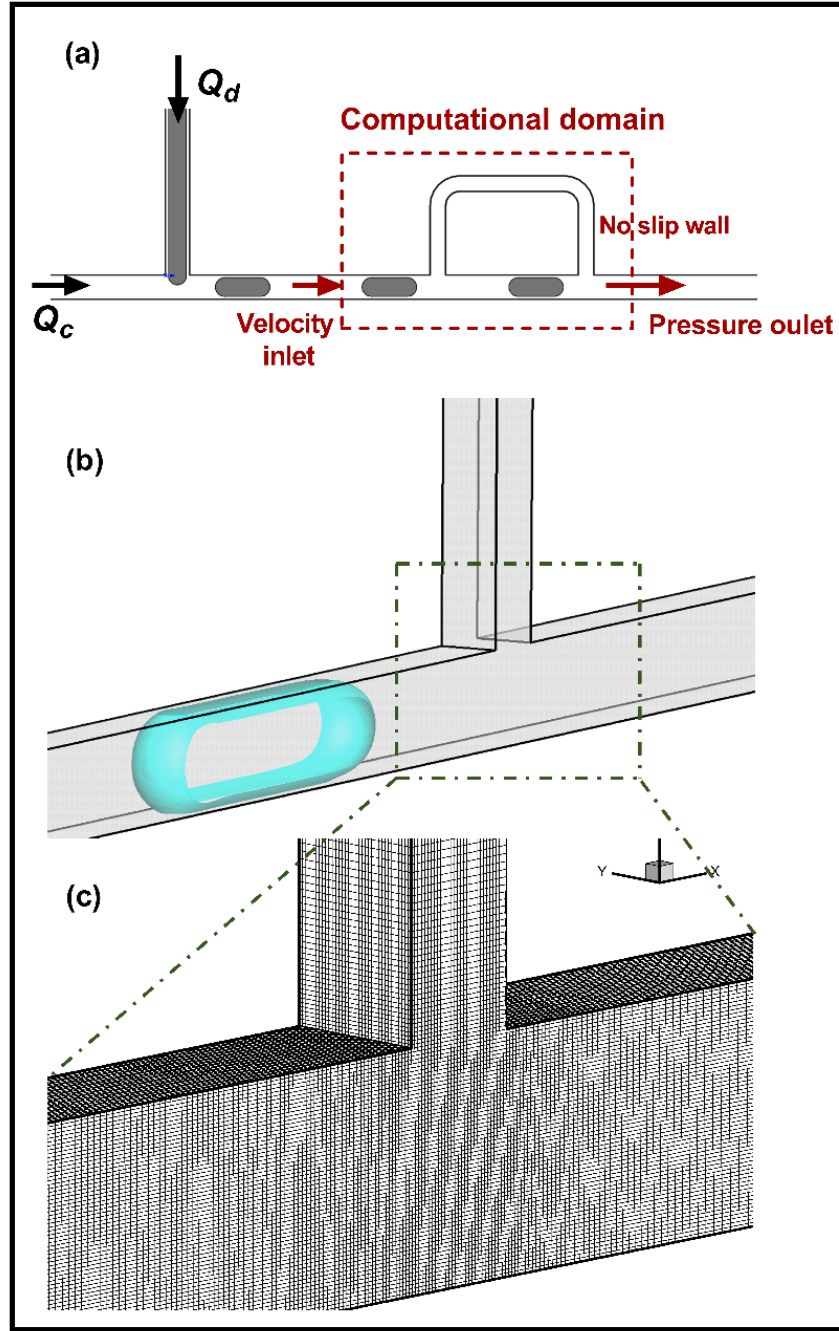


**Figure 2.2:** (a) Problem definition shown by a schematic. The computational domain is shown by a dotted box and boundary conditions are shown at the inlet, outlet, and wall (b) Zoomed in view of the entrance to the bypass channel and droplet shape before interaction with it. (c) Mesh is plotted in the region close to the entrance to the bypass channel.

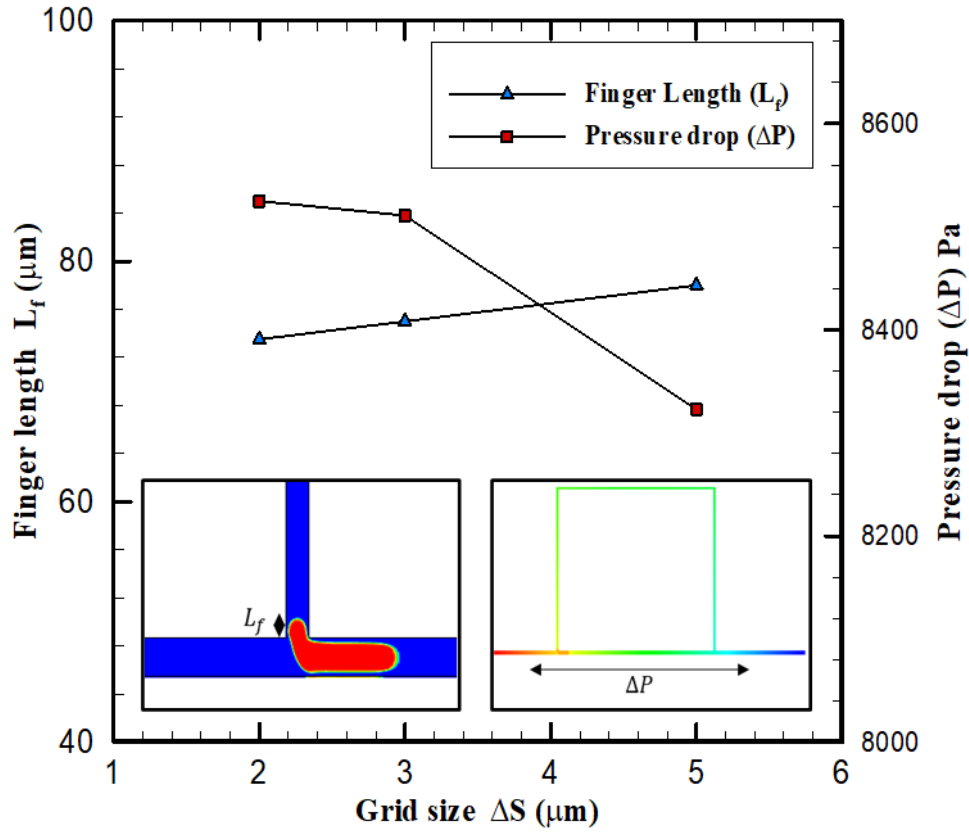


**Figure 2.3:** Grid size independence study: Finger length ( $L_f$ ) on the left-hand side of the Y-axis for different grid sizes (2  $\mu\text{m}$ , 3  $\mu\text{m}$  and 5  $\mu\text{m}$ ) on the X-axis at constant  $\beta = 0.62$ . Pressure drop in a microchannel on the right-hand side of the Y-axis for different grid sizes (2  $\mu\text{m}$ , 3  $\mu\text{m}$ , and 5  $\mu\text{m}$ ) on the X-axis when droplet interacts with the entrance of the bypass channel at constant  $\beta = 0.62$ .

Cases	$\Delta S$	Number of Cells	Relative % error in $\Delta P$ with respect to case 3	Relative % error in $L_f$ with respect to case 3
1	5 $\mu\text{m}$	$0.3 \times 10^6$	2.2 %	3.8 %
2	3 $\mu\text{m}$	$0.56 \times 10^6$	0.16 %	2 %
3	2 $\mu\text{m}$	$1.12 \times 10^6$	-	-

**Table 2.1:** Grid-independence test. Error in  $\Delta P$  and  $L_f$  are compared with the finest grid (2  $\mu\text{m}$ ).

## 2.3 Results

We present results of droplet behavior at the entrance to the bypass channel, characterizing it as either a breakup or non-breakup event. The analysis of the bypass channel will start with a study of the effect of ratio of the width of the bypass to that of the main channel ( $\beta$ ) in the range of 0.48 to 0.91, while keeping the capillary number constant ( $\text{Ca} \approx 0.003$ ). Then, we vary the capillary number from 0.001 to 0.04, while  $\beta \approx 0.48$ . Finally, we will compare experimental

and numerical results for interfacial dynamics and use this technique to explain the mechanisms of breakup. We combine the experimental data to present regime maps on  $Ca$ - $\beta$  plane with contours of finger length and volume of the daughter droplet. We have examined the volume of the mother droplet generated at upstream T-junction and compared this with a previously reported model [52].

### 2.3.1 Droplet Generation

The droplets are generated at a T-junction using oil and de-ionized water as the continuous and discontinuous phases, respectively. Of the existing literature, the geometry we have used most closely matches with that of Garstecki *et al.* [52] ( $w_d/w_m$ ). We compared the experimentally measured length of the droplet formed at the T-junction with the predicted scaling model given by Garstecki *et al.* [52] as  $\frac{L}{w} = 1 + \alpha \left( Q_{water}/Q_{oil} \right)$ , where  $L$ ,  $w_m$ ,  $\alpha$ ,  $Q_{water}$ ,  $Q_{oil}$  are the length of droplet formed, the width of the main channel, a fitting parameter ( $\alpha = 1$ ), the flow rate of water and the flow rate of oil, respectively. **Figure 2.4 a** plots the droplet length ( $L/w_m$ ) as a function of flow rate ratio and we note that the measurements of droplet length ( $L/w_m$ ) are clustered near the curve proposed by Garstecki *et al.* [52], and are slightly larger than the values predicted by the model.

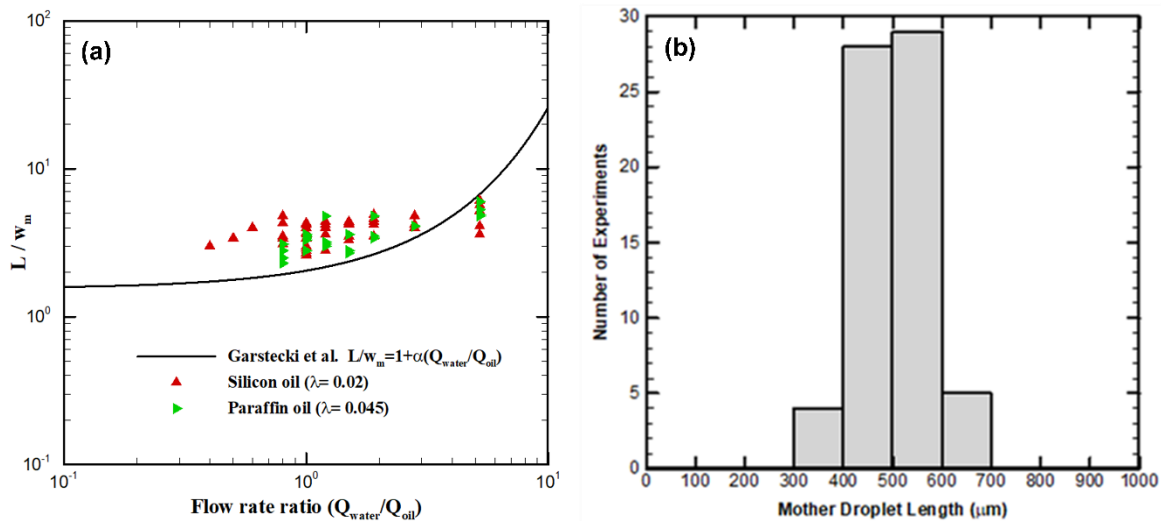


**Figure 2.4 :** (a) Comparison between dimensionless droplet length observed in experiments and model presented by Garstecki *et al.* [52]. The solid line is the curve showing the predicted droplet size. (b) Mother droplet length Vs Number of experiments.

We observed that in our experiments, the variation of mother droplet length is relatively small. We have plotted mother droplet length distribution in **Figure 2.4 b**. The average length of mother droplet is 500  $\mu\text{m}$ , and we have maintained mother droplet length of  $500 \pm 100 \mu\text{m}$  in 88 % of our experiments.

### 2.3.2 Effect of Channel Width Ratio

To start the analysis of the droplet interaction with the entrance of the bypass channel we examine the effect of the ratio of width of the bypass channel to the main channel,  $\beta$ . A range of  $\beta$  from 0.48 to 0.91 was used, keeping the capillary number constant at  $0.0028 \pm 0.0002$ . To classify the droplet interaction with bypass channel as droplet breakup, it must satisfy two conditions: i) the volume of the daughter droplet formed must be more than 2% of that of mother droplet volume and ii) the droplet breakup must be consistent. In **Figure 2.5** image sequences are shown column-wise for three different values of  $\beta$  ( $\beta = 0.48, 0.77, 0.91$ ). At  $\beta = 0.48$ , when the droplet interacts with the bypass entrance, breakup does not occur (it does not satisfy the two conditions), the maximum finger length,  $L_f$  into the bypass channel was measured to be 71  $\mu\text{m}$ . However, we observed tiny droplets inconsistently (the images have been chosen so that these droplets are observed). The percentage of the volume of these daughter droplets with respect to the volume of the original droplet ( $V_{ratio}$ ) is less than 2%. At  $\beta = 0.77$ , the droplet breakup occurs consistently, with a finger length of 97  $\mu\text{m}$  prior to partition, and a volume ratio of 12%. When  $\beta$  was increased to 0.91 the finger length rises to 139  $\mu\text{m}$  and the volume ratio to 30%. From this data, a critical value of  $\beta$  exists at a given  $Ca$ , above which droplet production is consistent, and upon further increase of  $\beta$  the finger length and, hence the volume ratio will rise.

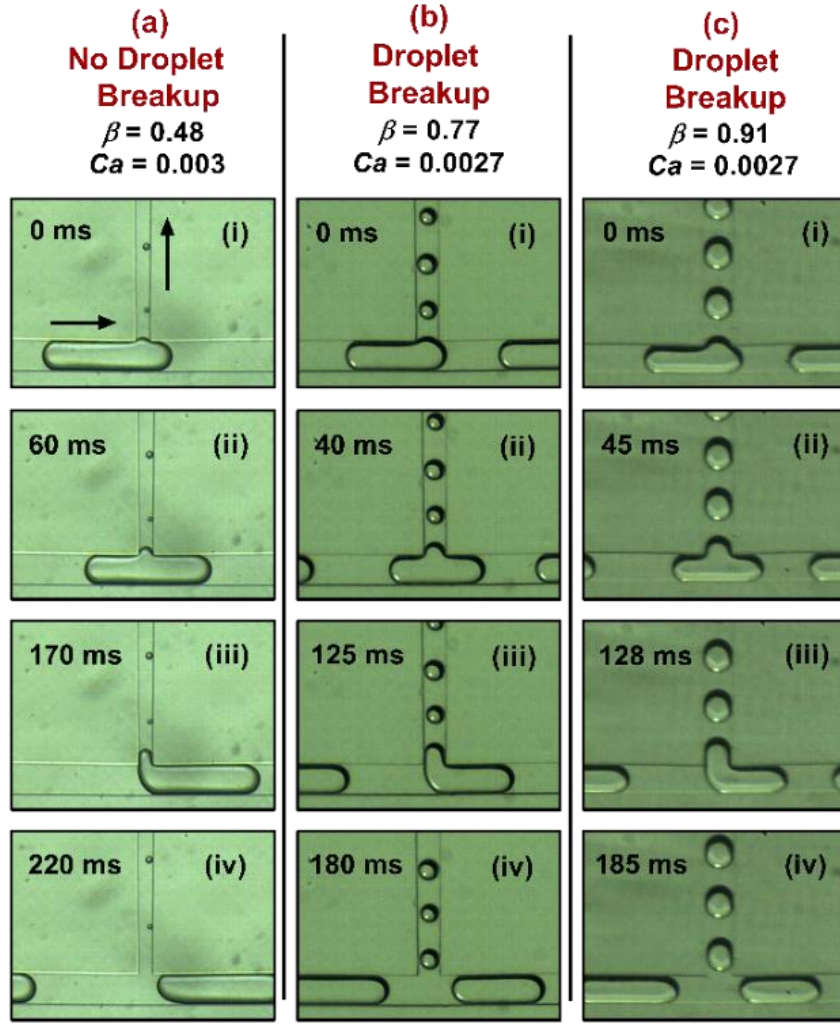


**Figure 2.5:** High-speed visualization of the droplet interaction with the entrance of the bypass channel showing the transition from no droplet breakup to droplet break up at different time intervals. Results are plotted for three cases of  $\beta$ . (a)  $\beta = 0.48$  (see appendix B, video B1) (b)  $\beta = 0.77$  (see appendix B, video B2) (c)  $\beta = 0.91$  (see appendix B, video B3). Capillary number is kept almost constant in all cases ( $Ca = 0.0028 \pm 0.0002$ ).

### 2.3.3 Effect of Capillary Number ( $Ca$ )

We investigate the effect of  $Ca$  over the range of 0.001 to 0.04, while keeping  $\beta$  constant at 0.48. **Figure 2.6** shows that at  $Ca = 0.0022$ , droplet breakup occurs at the bypass entrance with a finger length of  $82 \mu\text{m}$  and the volume ratio of 7%. However, with increased  $Ca$ , droplet breakup ceases. Instead at  $Ca = 0.005$ , we don't observe droplet breakup with a finger length of  $71 \mu\text{m}$ . For further increase of  $Ca$  to 0.037 caused droplet breakup to cease completely and the finger length to drop further to  $27 \mu\text{m}$ . Hence, a critical value of  $Ca$  exists to achieve breakup at a constant  $\beta$ . Also,  $L_f$  and  $V_{ratio}$  decrease with increased  $Ca$ .



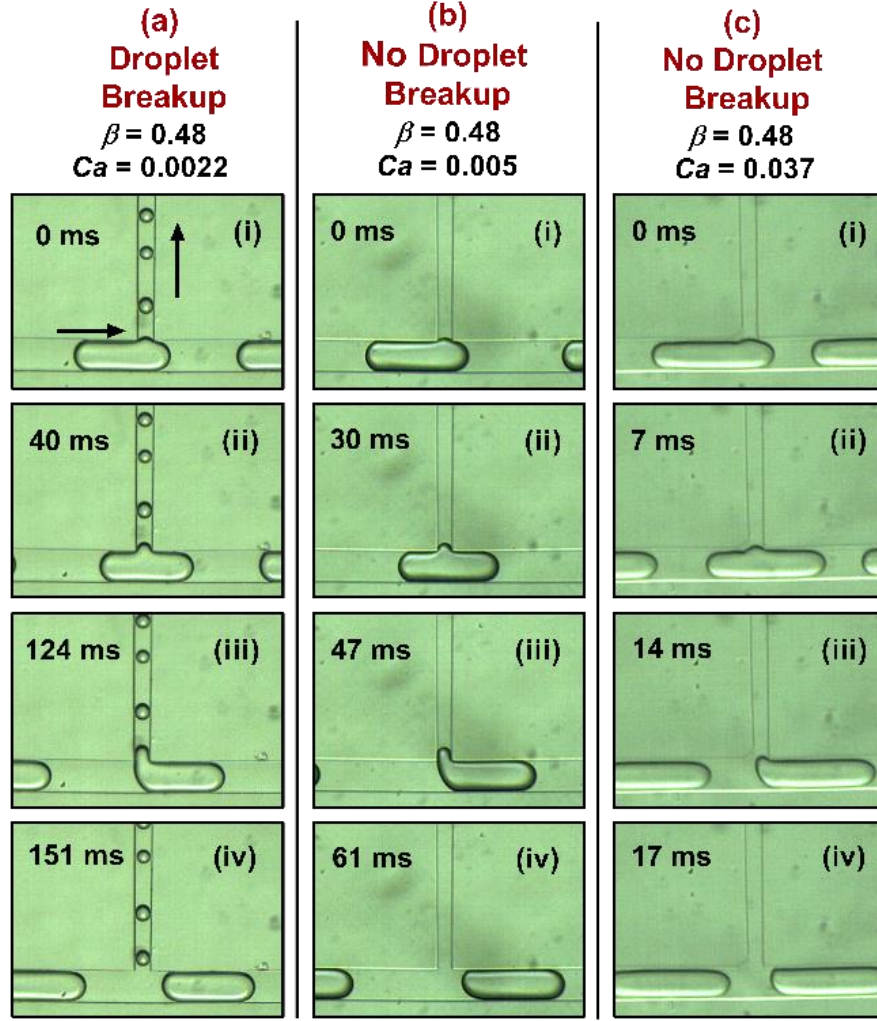


**Figure 2.6:** High-speed visualization of the droplet interaction with the entrance of a bypass channel showing the transition from no droplet breakup to droplet break up at different time intervals showing the effect of  $Ca$  (a)  $Ca = 0.0022$  (see appendix B, video B4) (b)  $Ca = 0.005$  (see appendix B, video B5) (c)  $Ca = 0.037$  (see appendix B, video B6). The ratio of channel width  $\beta$  is kept constant in all cases ( $\beta = 0.48$ ).

### 2.3.4 Comparison between Experimental and Computational Results

We compare the results from numerical simulations of the non-breakup case with the experimental results at  $\beta = 0.48$  and  $Ca = 0.005$ , as shown in **Figure 2.7**. The length of the mother droplet in the simulation is kept similar to that of measured in the experimental work. The shape of the droplet interface obtained at different times is in excellent agreement qualitatively with those recorded in the experiments. We compare finger length and volume of daughter droplet as the criteria for validation. The experimentally measured maximum  $L_f$  is 62  $\mu\text{m}$  while the numerical value is found to be 53  $\mu\text{m}$ . Similarly, **Figure 2.8** compares the

experimental results with computational data for a case of droplet breakup ( $\beta = 0.63$  and  $Ca = 0.007$ ); again, good agreement is observed. The experimentally measured  $L_f$  is around  $90 \mu\text{m}$  as compared to a computed value of  $78 \mu\text{m}$ . The percentage of daughter droplet volume in experiments as compared to original droplet ( $V_{ratio}$ ) is measured to be 11.4% while in computational work, it is around 7.2%. The difference between the values of computational and experimental results is attributed to the fact that we have considered only one droplet in the entire system in a computational investigation. However, there are many droplets in actual experiments, and each droplet has a hydrodynamic resistance. The number of droplets in the main channel after the bypass channel in actual experiments adds additional hydrodynamic resistance compared to computational investigation with only one droplet. This additional hydrodynamic resistance in experiments causes an increase in daughter droplet volume compared to the numerical investigation.

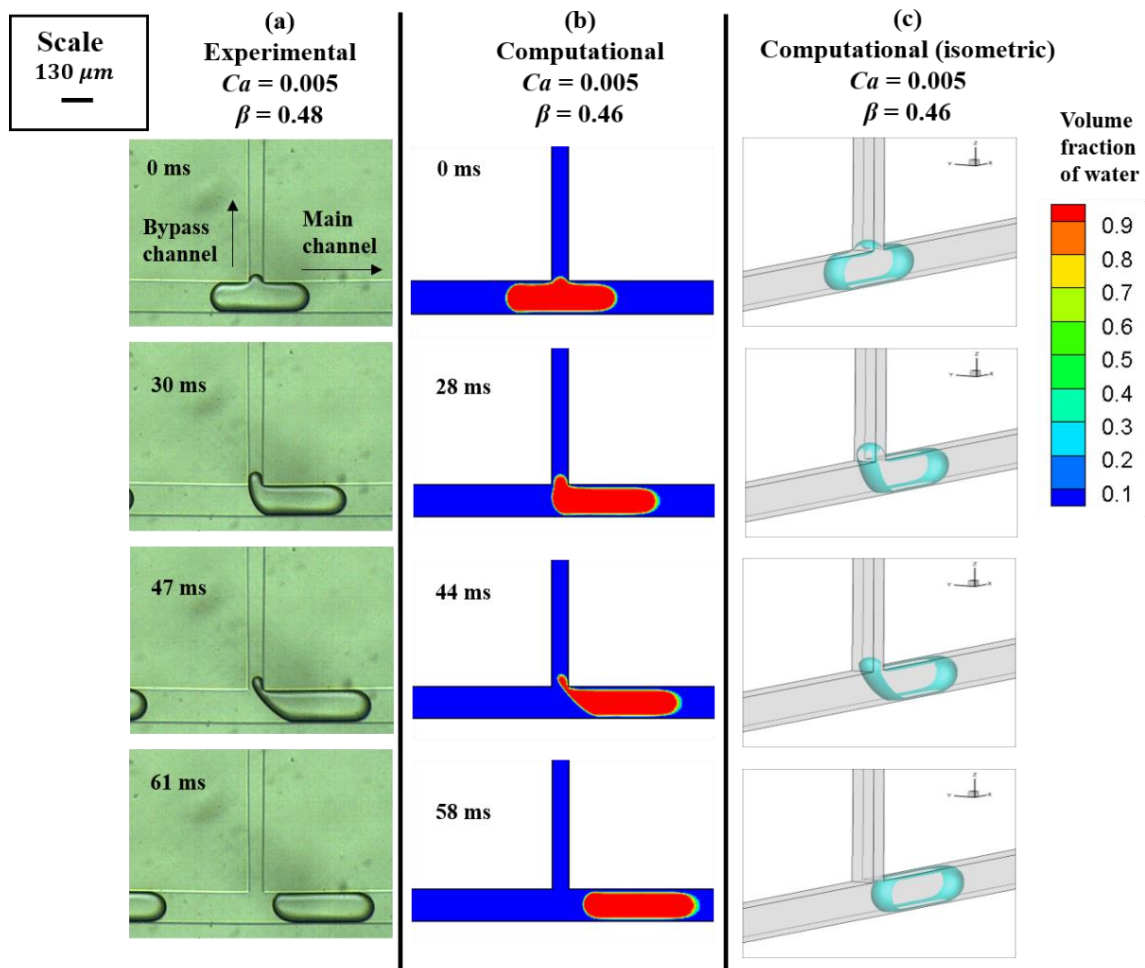


**Figure 2.7:** Comparison between experimental and computational work at  $\beta = 0.48$  and  $Ca = 0.005$ . (a) High-speed visualization of the droplet interaction with the entrance of a bypass channel. (b) Computed

contours of the volume fraction of water (see appendix B, video B7). (c) Isometric view of the iso-surface of the volume fraction of water at 0.5.

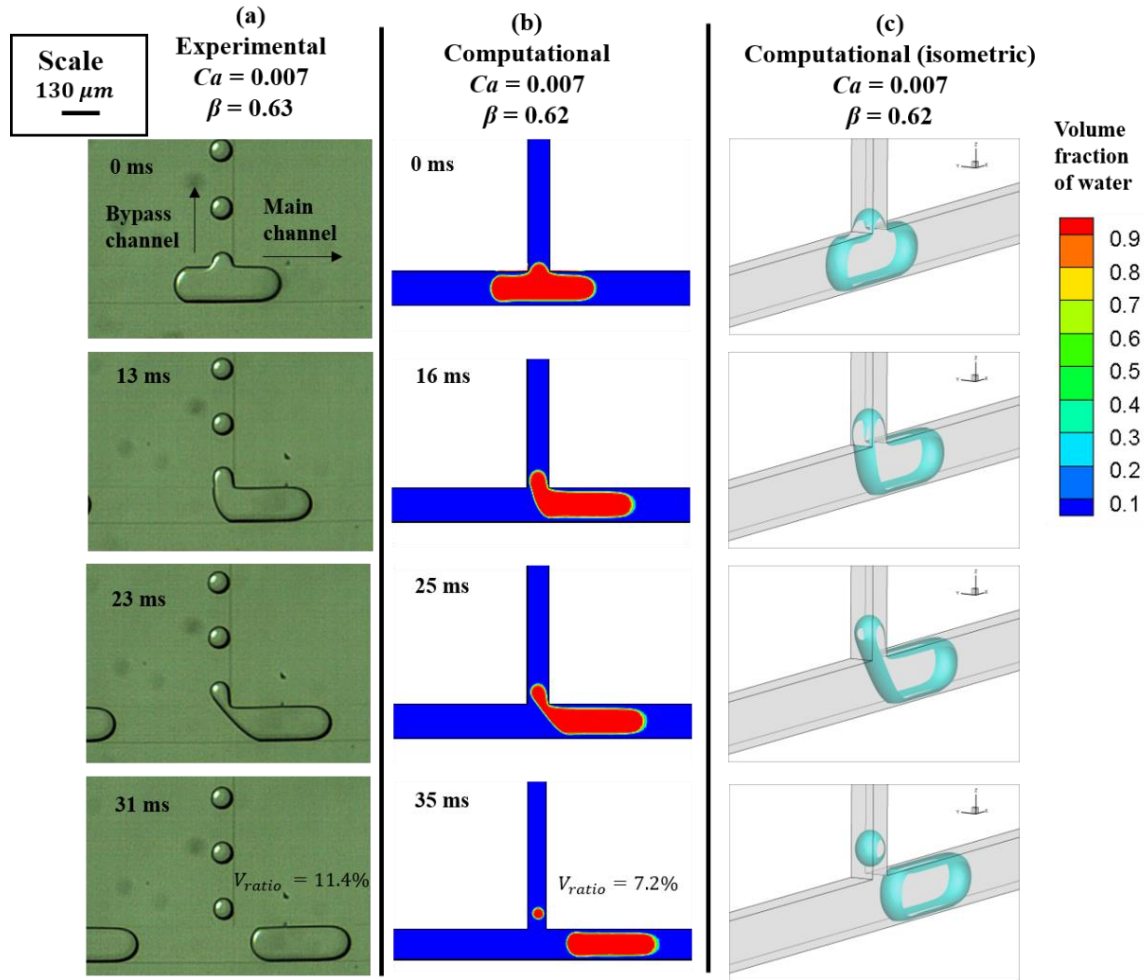


**Figure 2.8:** Comparison between experimental and computational work at  $\beta = 0.63$  and  $Ca = 0.007$ . (a) High-speed visualization of the droplet interaction with the entrance of a bypass channel. (b) Computed contours of the volume fraction of water (see appendix B, video B8). (c) Isometric view of the iso-surface of the volume fraction of water at 0.5.

### 2.3.5 Regime Map

**Figure 2.9** plots data of all the measurements performed in the present study on the  $Ca$ - $\beta$  plane and indicates the transition between the breakup and non-breakup regimes by way of the dashed line. We plot the corresponding finger length ( $L_f$ ) obtained in five ranges, as shown by the legend of **Figure 2.9 a**. Each range is represented using a different symbol and colour. As mentioned earlier and shown by the regimes in **Figure 2.9 a**, to achieve the breakup, a critical value of  $\beta$  exists at constant  $Ca$ , and a critical value of  $Ca$  exists at constant  $\beta$ . The finger length,

$L_f = [125, 150] \mu\text{m}$ , is found to be present at a smaller  $Ca$  and larger  $\beta$ . In the breakup region,  $L_f$  decreases with increase in  $Ca$  at constant  $\beta$  or with a decrease in  $\beta$  at constant  $Ca$ .  $L_f = [25, 75] \mu\text{m}$  corresponds to non-breakup region. As pointed to in Ref. [57], we also observed the existence of a critical finger length ( $75 \mu\text{m}$  in the present study) for achieving the droplet breakup.

**Figure 2.9 b** shows the regime map on the  $Ca$ - $\beta$  plane, and we plot the percentage of daughter droplet volume with respect to original droplet volume ( $V_{ratio}$ ) for the two regimes. The value of  $V_{ratio} = [0, 2] \%$  is assumed to be in the non-breakup region since droplet breakup in this region was very intermittent and inconsistent. In the droplet breakup region the maximum value of  $V_{ratio} = [25, 35] \%$  is measured when  $Ca$  is at the minimum of the range examined and  $\beta$  the maximum, as we go on increasing  $Ca$  or decreasing  $\beta$ ,  $V_{ratio}$  starts decreasing from (25-35%) to (15-25%) to (2-15 %) and finally to (0 to 2%) which we classify as the non-breakup region due to its intermittency.

### 2.3.5.1 Transition Region

When we increase  $Ca$  while keeping  $\beta$  constant, we observe a transition region where, tiny intermittent daughter droplets are produced. As volume of these droplets is less than 2% of mother droplet volume and these tiny droplets are produced once in four to five interactions we don't term this droplet breakup. Insets on the left-hand side of **Figure 2.9** show the transition region at a constant  $\beta$  of 0.48. We observe that at  $Ca = 0.0022$  when the mother droplet interacts with the bypass channel droplet breakup occurs. As  $Ca$  is increased to 0.0033, we observe tiny droplets being produced once in every few interactions. With further increase in  $Ca$  to 0.005, we observe no droplet breakup. Similarly, insets on right-hand side of **Figure 2.9**, shows transition region at constant  $\beta$  of 0.77. We observe that at  $Ca = 0.032$  when mother droplet interacts with bypass channels, droplet breakup occurs. As  $Ca$  is increased to 0.04, we observe tiny droplets being produced in an irregular fashion. We observe that when the system is operating in transition region a slight change in flow condition, we are able to go from breakup to no breakup.

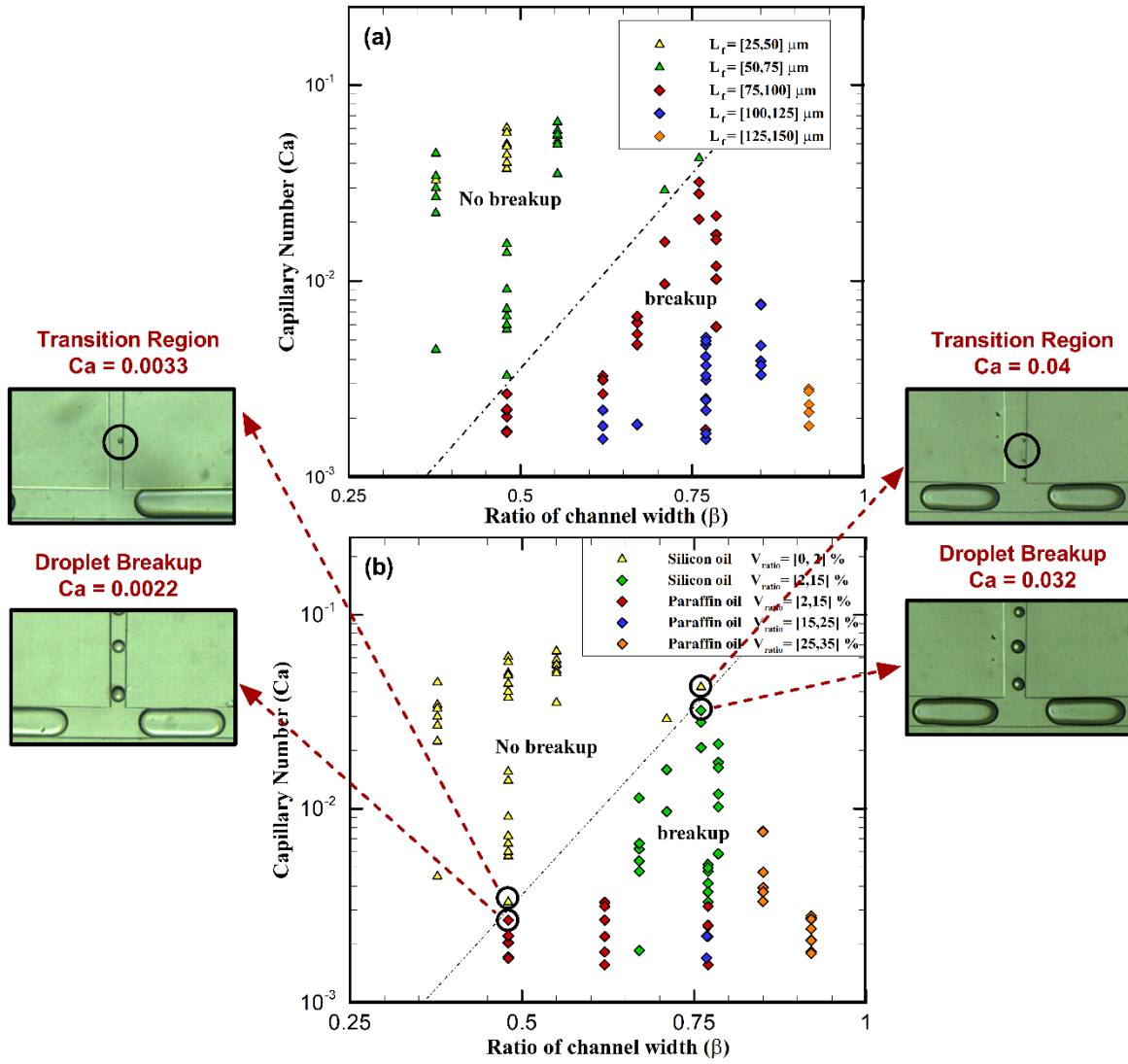


**Figure 2.9:** (a) Regime map is showing contours of finger length ( $L_f$ ) on  $Ca-\beta$  plane. A dotted line is shown to demarcate regions of droplet breakup and no droplet breakup. (b) Regime map showing contours of  $V_{ratio}$  on  $Ca-\beta$  plane.

## 2.4 Discussion

### 2.4.1 Equivalence to Squeezing and Dripping Regime

According to Garstecki *et al.* [52], interfacial tension acts as a stabilising force while resistance to the flow of the continuous phase ( $F_R$ ) and shear force ( $F_\tau$ ) act as destabilising forces in case of droplet generation at standard T-junction. If the gap between the droplet and main channel wall ( $\varepsilon$ ) is smaller than the width of the main channel ( $w$ ), i.e.  $\varepsilon \ll w$ ,  $F_R > F_\tau$  which means leading contribution for droplet breakup comes from  $F_R$ , and this regime is commonly referred as squeezing regime [53]. If  $\varepsilon \sim w$ ,  $F_\tau$  has a significant role to play in droplet breakup along

with  $F_R$ , and this regime is commonly referred to as the dripping regime [53]. Now in this section, we identify an equivalent squeezing and dripping regime in our experiments when generated droplet interacts with the entrance to the bypass channel.

For droplet generation, Menech *et al.* [53] plotted the dimensionless droplet volume ( $V$ ) as a function of  $Ca$  and found out that slope of  $V$  versus  $Ca$  is almost constant in the squeezing regime (which means the droplet volume remains almost constant even after variation in  $Ca$ ) and becomes steeper in the dripping regime (the droplet volume starts to decrease drastically against an increase in  $Ca$ ). In **Figure 2.10**, we plot the dimensionless daughter droplet volume ( $V_d^*$ ) as a function of  $Ca$  for the case droplet breakup at  $\beta = 0.77$ , where  $V_d^* = (\text{volume of daughter droplet}) / (w_m \times w_b \times h)$ . We observed that for constant  $\beta$  if we increase  $Ca$ , the size of the daughter droplet formed decreases; hence the slope of  $V_d^*$  as a function of  $Ca$  becomes steeper in the dripping regime. A similar trend is observed by Menech *et al.* [53]. Insets of **Figure 2.10** show that as we increase  $Ca$ ,  $\varepsilon$  also increases, where  $\varepsilon$ , in this case, is the distance between the wall of the bypass channel and droplet when it is about to break, which signify that the formation of the daughter droplet takes place from a finger which is smaller than the width of the bypass channel. In this case (droplet breakup at bypass channel),  $\varepsilon$  becomes comparable with  $w_b$  at  $Ca \approx 0.02$ , while Menech *et al.* [53] observed similar at  $Ca \approx 0.015$  (for droplet generation).

Thus far, we have defined our dripping regime by comparing the value of  $\varepsilon$  with the value in the dripping regime of droplet generation. However, for this to be an accurate analogy, there should be more than a geometrical similarity, the physics should also be similar. The key feature of the dripping regime is that the shear force, caused by the flow that goes around the interface through the gap measured by  $\varepsilon$ , and starts to play an important role in the generation of the droplet. We now examine if a rise in shear force is also evident in the case of droplet breakup at bypass channel.

We plotted contours of the shear stress in three cases of breakup using numerical simulations for  $Ca = 0.025, 0.031$  and  $0.037$  in **Figure 2.10 b**. In these simulations, the mother droplet volume, the interfacial tension between continuous and discontinuous phase and the viscosity are kept constant, and the change in  $Ca$  is achieved through an increase in the droplet velocity. We have calculated the shear stress on the finger, due to the flow past the finger into the bypass channel. We have plotted component of shear stress,  $\tau_{xz}$ , in the mid-XZ plane of the channel.  $\tau_{xz}$  was averaged over the figure length (liquid-liquid interface), as shown in insets of



**Figure 2.10 b.** We observe that in the dripping regime as  $Ca$  increases, the shear stress acting on the liquid-liquid interface also increases.

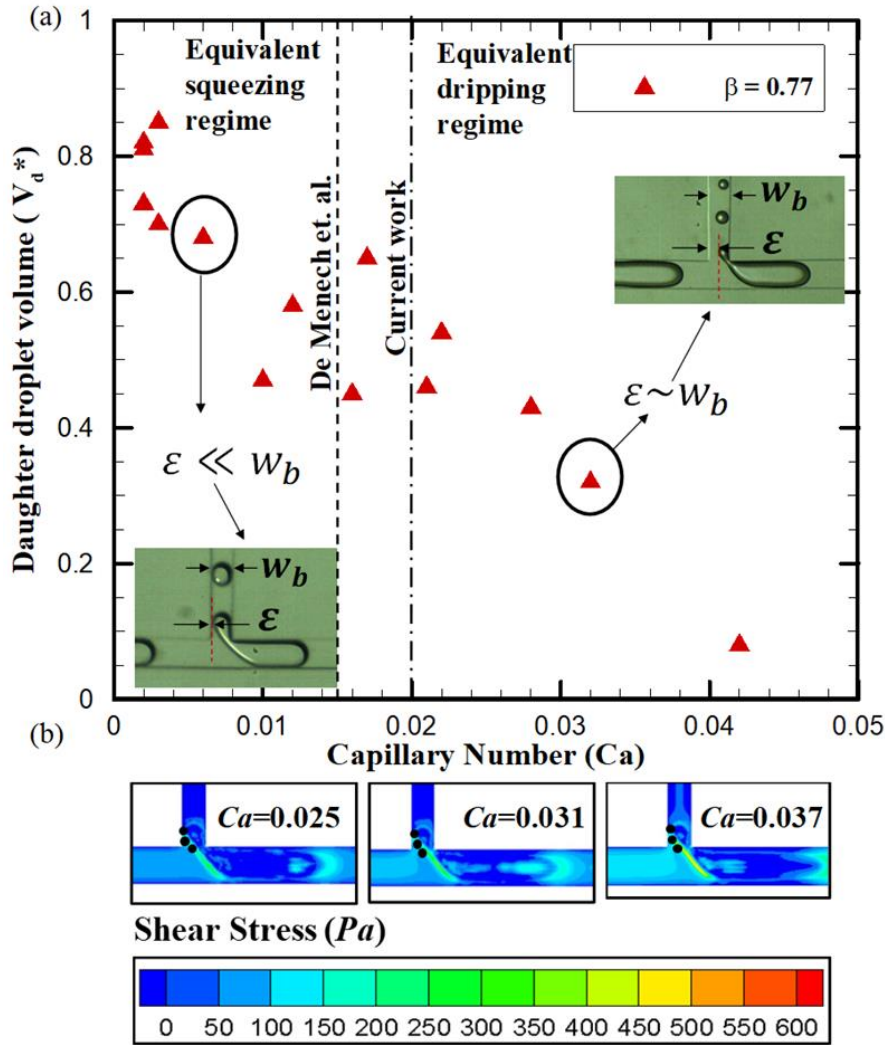


**Figure 2.10:** (a) Dimensionless daughter droplet volume as a function of the capillary number showing equivalent squeezing and dripping regime. The dotted line shows the squeezing regime given by Menech et al. [53] and a dash-dot line showing current work. (b) Contours of shear stress at different  $Ca$  in the equivalent dripping regime.

To further investigate an equivalent squeezing and dripping regime, from our measurements, we plotted the evolution of  $L_f$  and  $\epsilon$  for  $Ca = 0.003$  (squeezing regime) and  $Ca = 0.030$  (dripping regime) in **Figure 2.11**. Both represent the case of droplet breakup and at  $\beta = 0.77$ . Stage 1 represents the time before the droplet interaction, and stage 6 represents the time just before the droplet breakup. These stages of droplet interaction are shown on the top of the plot. We observe that as the droplet moves past the bypass entrance  $L_f$ , as expected, keeps increasing, though the rate of change of  $L_f$  for  $Ca = 0.003$  is higher than that for  $Ca = 0.030$ .

The maximum value of  $L_f$  measured for  $Ca = 0.003$  is  $117\text{ }\mu\text{m}$ , while the maximum value of  $L_f$  measured for  $Ca = 0.030$  is  $65\text{ }\mu\text{m}$ . The value of  $\varepsilon$  is plotted as constant,  $3\text{ }\mu\text{m}$  (a single pixel) for the case of  $Ca = 0.003$ , as we do not see a visible gap between the droplet and microchannel wall. For the case of  $Ca = 0.030$ , the value of  $\varepsilon$  increases consistently from  $3\text{ }\mu\text{m}$  to  $35\text{ }\mu\text{m}$  making  $\varepsilon$  comparable with  $w_b$  as the droplet advances further, which is similar to the observation found in the dripping regime of droplet generation. As the value of  $\varepsilon$  becomes comparable with  $w_b$  shear stress starts to play an important role for this to be termed an equivalent dripping regime.

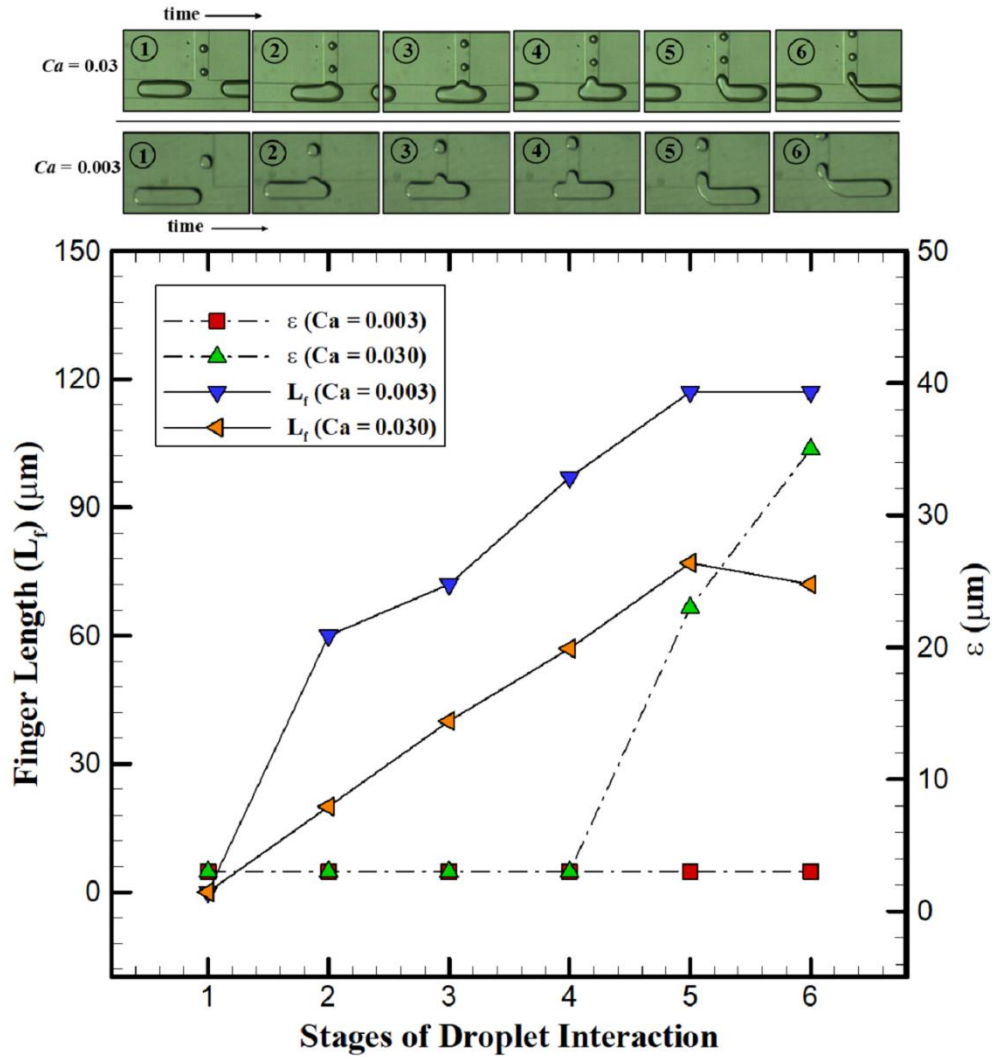


**Figure 2.11:** Evolution of finger length and  $\varepsilon$  with time. Finger Length ( $L_f$ ) plotted on the left-hand of Y-axis and  $\varepsilon$  on the right-hand side of Y-axis Vs. stages of droplet interaction (evolution with time).

**Figure 2.12** shows a zoomed-in view of pressure inside and outside part of the droplet.  $P$ ,  $P_h$ ,  $P_b$ ,  $P_1$  and  $P_2$  represent upstream pressure in the main channel, pressure close to head of



the droplet, pressure close to the tail of the droplet in the bypass channel, the pressure inside the tail end of the droplet and pressure inside the droplet close to head of the droplet. **Figure 2.13** and **Figure 2.14** plots the shear stress acting on the finger of the droplet and the hydrodynamic pressure built up ( $P-P_t$ ) plotted against the stages of droplet interaction with the bypass channel, using numerical simulations. We calculate the shear stress for different values of  $Ca$  and show that the shear stress increases with an increase in  $Ca$ . We plot the pressure build-up across the mother droplet for different values of  $Ca$  as well. In these simulations, an increase in  $Ca$  is achieved through an increase in the droplet velocity at the inlet, while keeping the droplet volume, surface tension, geometrical features and viscosity constant, all the simulations are cases of droplet breakup. Insets in **Figure 2.13** and **Figure 2.14** show the contours of shear stress, pressure and the corresponding stage of droplet interaction with bypass channel at which the current set of data is computed.

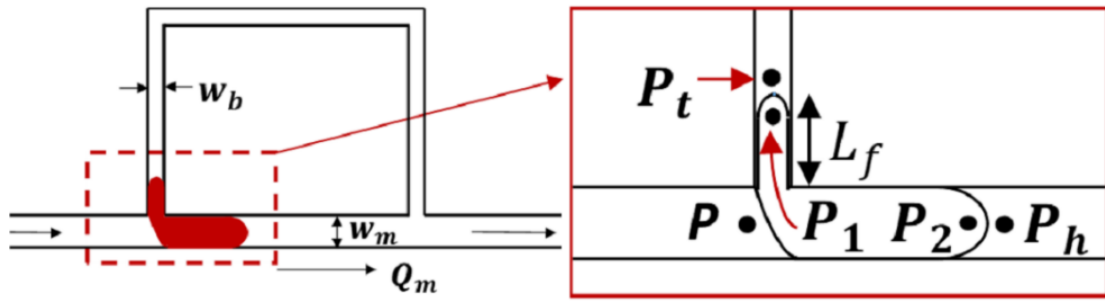


**Figure 2.12:** Schematic of the droplet interacting with the T-junction. Zoomed in view shows pressure notations inside and outside the droplet.

We observe that as we increase  $Ca$  by increasing inlet velocity; there is a consistent increase in the shear stress acting on the finger and a consistent decrease in  $(P-P_t)$ . When droplet enters the bypass channel, the average shear stress acting on the finger goes on increasing due to increase in  $\varepsilon$ . As per Garstecki *et al.* [52], the shear stress in droplet generation is given as  $\tau = (\mu u_{gap}/\varepsilon)$ , while  $u_{gap} = (Q_{oil} / h\varepsilon)$ , hence  $\tau = (\mu Q_{oil}/h\varepsilon^2)$ , where  $\tau$ ,  $\mu$ ,  $u_{gap}$ ,  $Q_{oil}$  and  $h$  are shear stress, the viscosity of the continuous phase, velocity in a gap and height of the microchannel respectively. In droplet generation, as the discontinuous phase push further into the main channel, and blocks it more, the shear stress and build-up of pressure increases, remembering that  $Q_{oil}$  is constant. In this study, the situation is more complicated; as time advances the value of  $\varepsilon$  increases; however, the flow through this gap is not fixed like droplet generation. Growing gap, causes the flow entering the bypass channel to increase (the droplet's progression in the

main channel and bypass channel will slow during this time); hence,  $Q_{oil}$  continues to increase. The growth in  $\varepsilon$  causes a rise in shear stress as captured with the numerical simulations. Even when the finger is narrower than the bypass channel, a droplet can be broken off. The finger length may retract slightly (as in **Figure 2.11**), but the rising shear can be enough to cause the droplet breakup.

In terms of the transition between regimes, we see from **Figure 2.13** and **Figure 2.14**, that as  $Ca$  rises from 0.018 to 0.025 we move from a situation in which shear stress starts to play a critical role in droplet breakup. Hence, the transition from the squeezing regime to the dripping regime is observed.

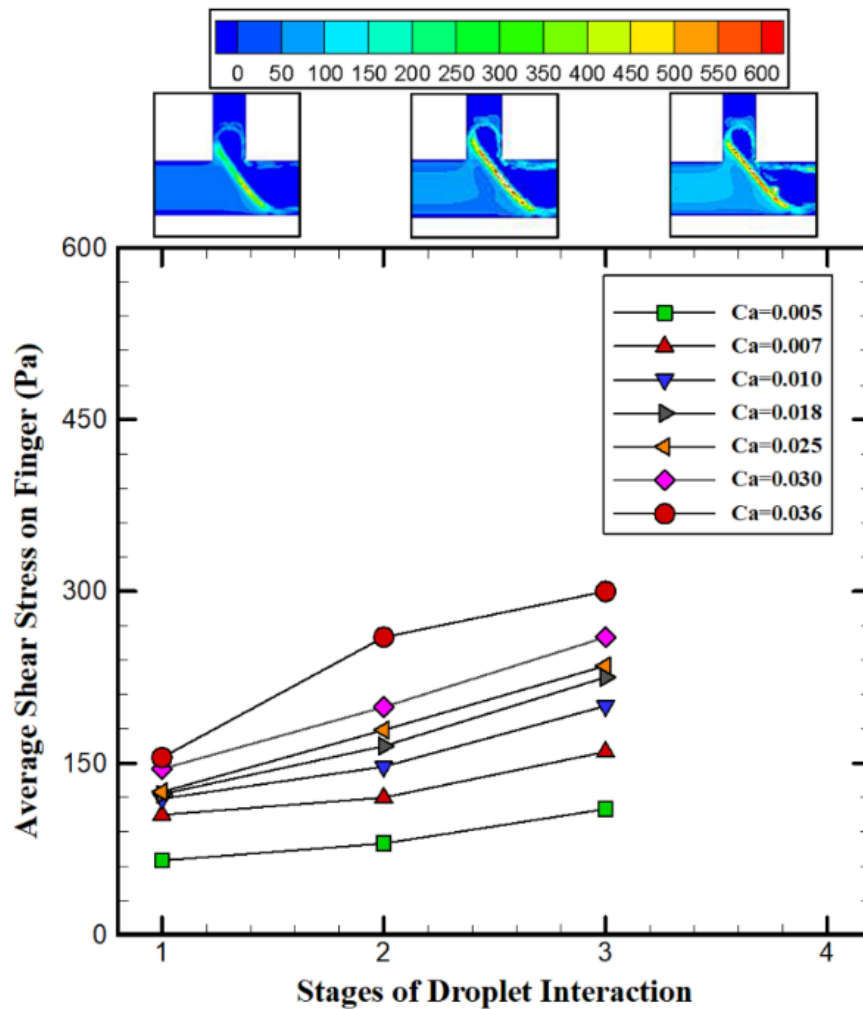


**Figure 2.13:** Evolution of average shear stress with time for  $Ca$  ranging from equivalent squeezing to the dripping regime. Contours at the top of the figure show average shear stress and corresponding stage of droplet interaction for given computed value.

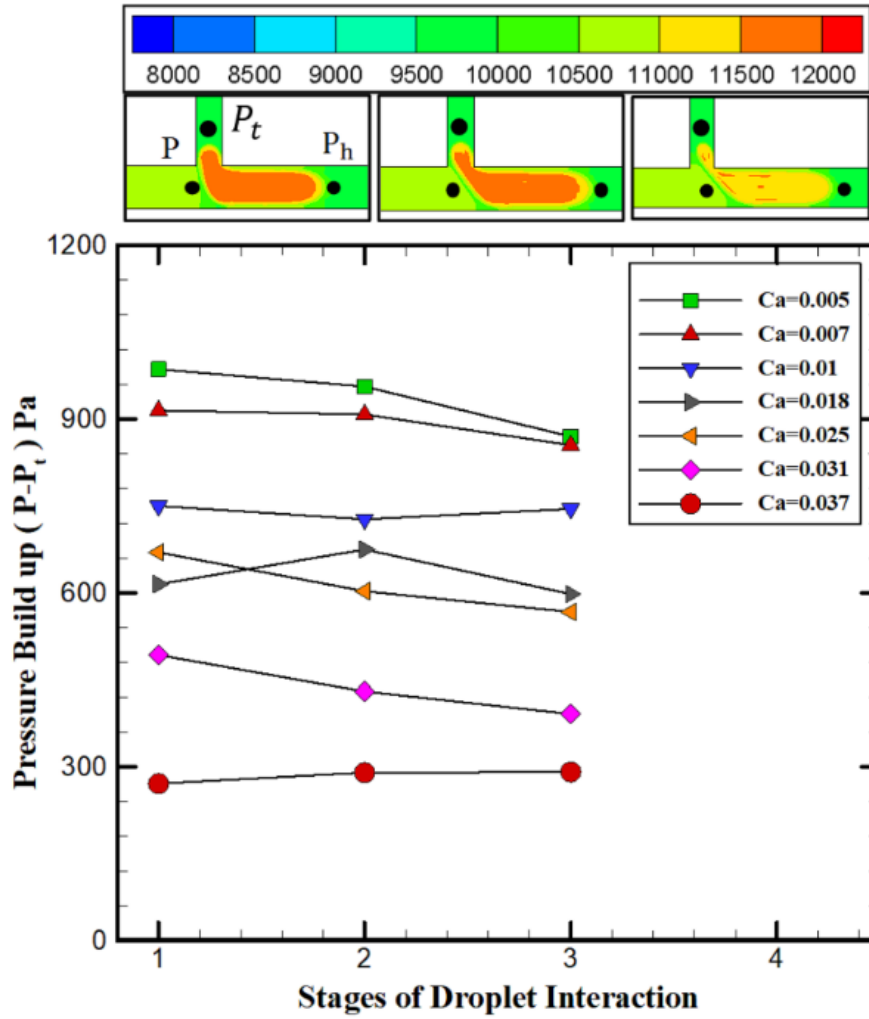


**Figure 2.14:** Evolution of pressure built up with time for  $Ca$  ranging from equivalent squeezing to the dripping regime. Contours at the top show pressure built up and corresponding stage of droplet interaction for given computed value.

## 2.4.2 Mechanism of Droplet Breakup

The flow of the continuous phase gets divided into the main channel and the bypass channel. Flow rate entering (thereby droplet entering) bypass channel depends on the hydrodynamic resistance of the channel. Because of the higher resistance of the bypass channel, only a small portion of the mother droplet enters the bypass channel. Now when we assume droplet trapped in the T-junction, it acts as a blockage to the fluid flow in the bypass channel temporarily, which contributes to increasing the resistance to the flow. The corresponding resistive force  $F_R$  is directly proportional to  $(P - P_t)$  and is given by  $F_R = (P - P_t) h w_b$ . The shear force acting on the finger is given by,  $F_\tau = \text{shear stress} \times h L_f$ , where  $L_f$  is the finger length and  $h$  is the height of the channel. Both  $F_R$  and  $F_\tau$  helps in droplet breakup in the bypass channel.

Once the droplet enters the bypass channel, interfacial tension will try to keep the droplet in the main channel, as  $w_m$  is always more than  $w_b$ . The interfacial tension force is directly proportional to the Laplace pressure jump across the interface. The Laplace pressure across the interface in bypass channel is  $\Delta P_{LB} = \gamma [(2/w_b) + (2/h)]$ , and the orientation of this force is downstream in the main channel. Similarly, the Laplace pressure across the interface in the main channel is  $\Delta P_{LM} = \gamma [(2/w_m) + (2/h)]$  and acting in the exact opposite direction of the previous one. The difference in the Laplace pressure is  $\Delta P_d = \gamma [(2/w_b) - (2/w_m)]$  and acting in a way that, it opposes the droplet breakup in the bypass channel. The corresponding surface tension force ( $F_\gamma$ ) is calculated by multiplying  $\Delta P_d$  by the cross-section area of the channel. Forces acting on the droplet trapped in the T-junction of the bypass channel is shown in **Figure 2.15 a**.

We compute  $(P-P_t)$ , and average shear stress at different instances during interaction of the droplet for the case of no breakup and breakup from simulations. Corresponding  $F_R$  and  $F_\tau$  are shown in **Figure 2.15**. We compute the value of  $\Delta P_d$ , thereby  $F_\gamma$  using both the approaches of simulation and Laplace equation. These simulation cases are like the ones discussed in **section 2.3.4**. The insets show pressure contours corresponding to the instance of the droplet interaction. As shown in **Figure 2.15 b**, when  $(F_R+F_\tau) > F_\gamma$ , droplet break up occurs. On the other hand, when  $(F_R+F_\tau) < F_\gamma$ , there is no droplet breakup, as shown in **Figure 2.15 c**.

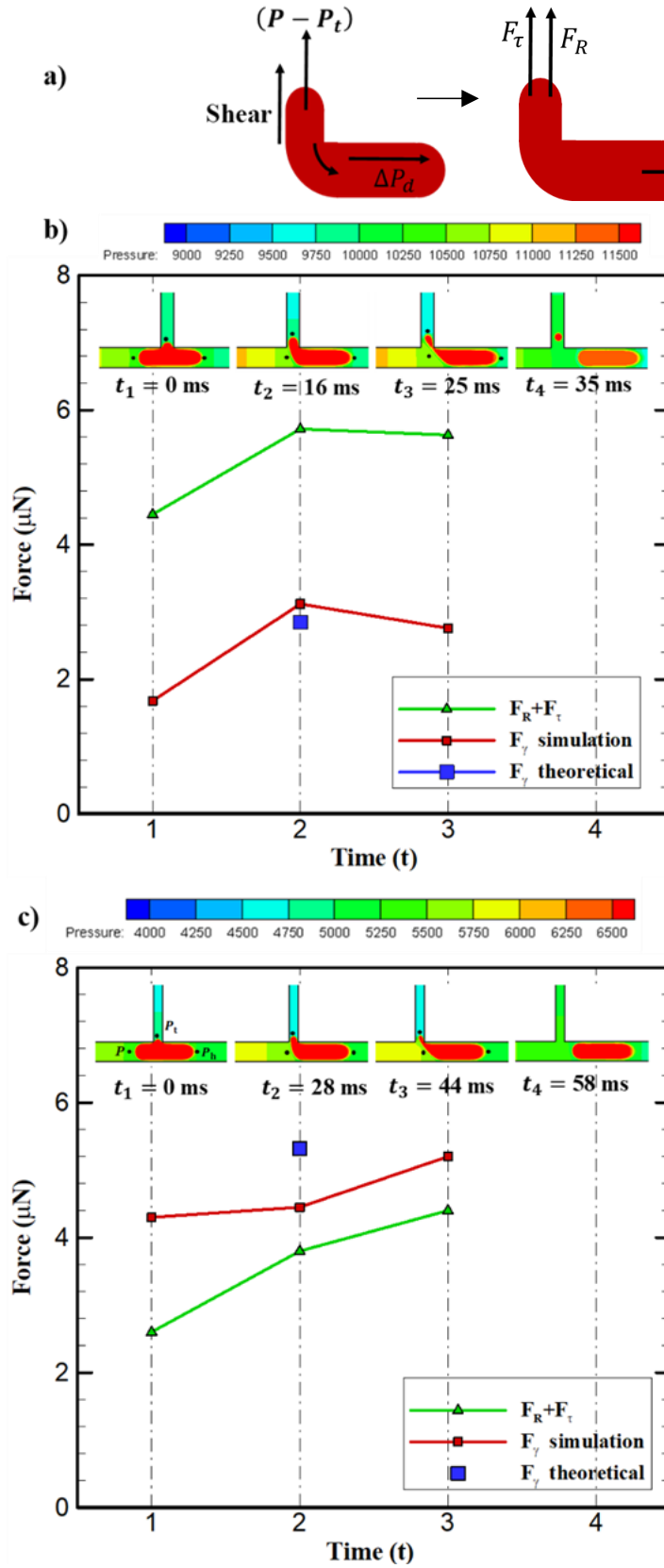


**Figure 2.15:** Evolution of  $(F_R + F_\tau)$  and  $F_\gamma$  during various stages of the droplet interaction with the T-junction of the bypass channel. (a) Forces acting on the trapped droplet. (b) The case of droplet breakup. (c) Case of no droplet breakup.

## 2.5 Application of Present work in Droplet-Based Microfluidics

Drug research is conducted with the help of high throughput screening (HTS). In this method target cells are tested against the library of compounds. Selective combinations of samples and reagents required by HTS makes it difficult to bring it on a microfluidic chip, as continuous droplet production methods are still used. Large droplets of different samples are relatively easily introduced onto a chip. Each is individually isolated, hence in the lab on a chip analogy, can be considered as test tubes. If you can selectively break up these droplets, these test tubes become pipettes, and a technology is born which can react to different chemicals in multiple permutations. An active mechanism used for selectively breaking the droplet into mother droplet used by Sesen *et al.* [80], where authors allowed the mother droplet to interact with the bypass channel and with the help of surface acoustic waves achieved selective droplet breakup into the bypass channel. In such applications exactly knowing the transition between droplet breakup and no breakup will certainly help in optimizing the duration of surface acoustic pulse and voltage applied to the interdigital transducers (IDT) resulting in precise control of daughter droplet volume. This chapter systematically examines the knife-edge (The knife-edge condition means a slight change in flow condition causes a change in outcome from no droplet breakup to droplet breakup) separating droplet breakup/no breakup (with the help of capillary number and geometry of the bypass channel), and forces at play so contribute significantly to the development of such technologies.

## 2.6 Closure

We investigated the effect of the width of the bypass channel ( $\beta$ ) and Capillary number ( $Ca$ ) on no droplet breakup to droplet breakup regimes. Microchannels are fabricated using standard photolithography techniques, and interfacial dynamics is visualised using a high-speed camera. Silicon oil/paraffin oil and water are used as a continuous phase and a discontinuous phase, respectively. Experiments show that there is a critical value of  $\beta$ , keeping  $Ca$  at a constant value, for achieving the droplet breakup. Similarly, there is a critical value of the  $Ca$  exists, keeping  $\beta$  constant. We have proposed a regime map on  $Ca$ - $\beta$  plane for showing regimes of no breakup and breakup. In regime map, we plotted the contours of finger length ( $L_f$ ) and percentage of the volume of daughter droplet to mother droplet volume ( $V_{ratio}$ ). We observed that the maximum volume of the daughter droplet corresponds to the minimum  $Ca$  and maximum  $\beta$ . Three-dimensional numerical simulations are carried out using commercial CFD

software for the breakup and no-breakup cases and validated with the experiments. The simulated results for interfacial dynamics,  $L_f$  and  $V_{ratio}$ , are found to be in good agreement with the experimental results. Simulations proved that when the hydrodynamic pressure drops across the droplet and average shear stress acting on the finger overcomes differential Laplace pressure of the droplet; droplet breakup occurs otherwise not. Like the squeezing and dripping regimes of droplet generation, we report regimes for droplet breakup at the entrance of a bypass channel, and they exhibit equivalent squeezing and dripping regimes. In the squeezing regime, the hydrodynamic pressure drop across the droplet plays a crucial role while in the equivalent dripping regime, both shear stress and hydrodynamic pressure drop are dominant. This work provides useful information regarding the knife-edge between droplet breakup and no breakup, thus significantly useful for the development of technologies used for droplet breakup.





# Chapter 3

## 3 Microfluidic Valves for Selective on-Chip Droplet Breakup at Multiple Sites

*In the previous chapter, we investigated the knife-edge condition at the entrance of the bypass channel. We extend the study to figure out knife-edge condition at two locations and later use two single-layer microvalves (both numerically and experimentally) to alter the behaviour from no droplet breakup to breakup. To be specific, we present a microfluidic system for droplet breakup at two junctions which are placed one after the another. Droplets are generated at standard T-junction upstream and then introduced to the droplet division section which consists of a T-junction and an expansion channel. In the first set of experiments, the droplet division section consists of two identical T-junctions branching from the main channel and place one after another. With this geometry, we produced daughter droplets only at the first junction while there is no droplet breakup in the second junction for any flow condition. Resistive network analysis is used to design the microfluidic system with expansion channel in place of second T-junction, so that same flow rate enters at both the locations. We observe five regimes of droplet breakup in a microfluidic system, namely 1) No droplet breakup at two junctions. 2) Droplet breakup only at the first junction, 3) Droplet breakup at both the junctions with higher daughter droplet volume in first junction 4) Droplet breakup at both the junctions with daughter droplet volume higher at second junction 5) Intermittent/irregular droplet breakup in both the junctions. Under fluid flow condition, droplet interaction with both the junctions produces the same output of no droplet breakup. We then showed design requirements for the location of two single-layer microvalves, simulated by permanent deformation of the main channel wall. We used experiments to break the droplet at two locations using two microvalves.*

### 3.1 Introduction

Droplet-based microfluidics has emerged as an excellent tool for a wide range of biological and chemical applications [7]. Samples and reagents can be encapsulated in a droplet and later

can be divided, for conducting various screening processes. Compartmentalizing samples and reagents in small-sized droplet volumes in a buffer of continuous immiscible phase enables the creation of thousands of reaction volumes without any cross-contamination. Droplets in a microfluidic system find application in analyzing small biological samples, even single cells [14] can be encapsulated and analyzed. Other notable applications of droplet microfluidics are microparticle synthesis [15,16], immunoassays [135], reaction kinetics [9], protein crystallization [11,136], clinical diagnosis [12,13] and conducting high-throughput analysis [137,138].

In high-throughput screening, target samples/disease cells are comprehensively examined against a library of compounds in search of a positive outcome, a process currently performed using microtiter plates and robotic dispensing. However, miniaturisation limits have been reached due to the achievable accuracy of robotic dispensing and evaporation issues in open systems. For further miniaturization of setup, minimising sample and reagent usage, thereby cost reduction. Droplet-based microfluidics provides a compelling alternative as it provides the ability to handle nano to femtoliter volume of samples in an evaporation-free environment. However, a key strength of droplet microfluidics, the rapid production of thousands of identical droplets/samples [25, 26, 52, 121, 139, 140] does not lend itself well to conduct multiple reaction permutations between libraries of samples, which requires the generation merging, splitting, trapping of pairs of droplets of different types. As such, to conduct complex screening processes on a microfluidic device, one approach would be to input large droplets of different types, subdivide and merge them at will. This approach allows for the correct sample to be dispensed at the right reaction site, an on-chip analogy to pipetting [80,141]. Subsequently, the samples require merging, trapping and mixing.

Droplets can be subdivided into symmetric [142,143] or asymmetric [105] daughter droplets using the change in geometric features [144–146] and alteration of flow conditions [56]. However, these passive methods do not require any external energy input, which means that each droplet leads to the same fate; they are all subdivided continuously not selectively. To be able to break droplets selectively active methods are required, where external energy input briefly controls the outcome of a droplet breakup at a specific location on the microfluidic chip, the result is the breakup of a single droplet when and where required. **Figure 3.1** shows how this can be implemented for HTS is depicted using a schematic. Various forms of active methods have been used in conjunction with droplets; some of these methods are surface acoustic waves [32,78, 80,81,129], micro-valves [141], electric fields [147], microheaters [75] and use of a laser [73].

In order to develop a single-layer horizontal microvalve based approach to break selected individual droplet, we first investigated the behaviour of droplets as they pass a junction to a secondary channel which later rejoins the main channel, we termed this a bypass channel in the previous chapter. This study showed that there exist flow conditions at which the droplet remains intact on a knife-edge, but only just so [148]. With the mechanism behind knife-edge condition better understood, we demonstrated that a transition from non-breakup to breakup could be achieved by the partial closing of a microvalve at the entrance to the bypass channel [141] in a collaboration work which is not included in this thesis. However, in both cases, the selectivity of droplet breakup at only one location is considered, while reacting multiple chemicals in various permutations rapidly, more will be needed. Here, we investigate whether the knife-edge condition can be achieved at two junctions. Again, we use mother droplets (generated using standard T-junction) of the same material, rather than introducing different chemicals for each droplet. We design the microfluidic system required for break up at the two locations using resistive network analysis. Later, we demonstrate the capability of the device for selective break-up and location of the microvalve at either junction by local constriction of the main channel wall using experiments and three-dimensional numerical simulations. This demonstrates the prospects for performing pipette like-functions at multiple sites, so moving closer to the kind of robotic dispensing in microtitre plates being realised on a microfluidic chip, and so at far small volumes and no evaporation.

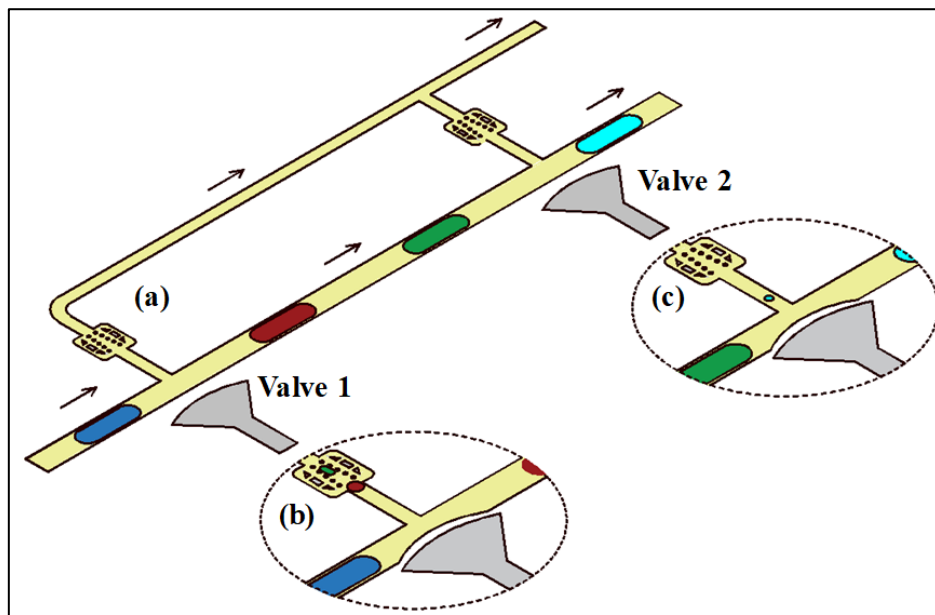


**Figure 3.1:** Conceptual depiction of selective droplet breakup using microvalves at two locations. (a) The “mother” droplets are generated at upstream T-junction (not shown) and, as they pass down the main channel, interact with the first and second junctions positioned adjacent to valves 1 and 2. When

the valves are off, operating conditions are chosen such that no droplet breakup occurs at these junctions. (b) When the first valve is pressurized and deforms, the selected droplet breaks up and a small droplet enters the side branch, here it is depicted that a sample of the green and red fluids are selected, subsequently these can be passively merged in the branch (c) Similarly, the second valve also allows selective break up such that different reactions can be initiated in its merging station. The result is a system in which a range of reaction permutations can occur between different reagents.

## 3.2 Methodology

### 3.2.1 Experimental Methods

The present microfluidic system consists of a standard T-junction to generate monodisperse droplets, and, downstream from this, two junctions placed one after another, and branching into a second outlet, at these junctions the selectivity of droplet breakup is investigated (**Figure 3.1**). The microfluidic chip is fabricated by bonding polydimethylsiloxane (PDMS) with a glass slide, glass is flat and acts as the substrate. At the same time, PDMS is patterned with the microfluidic channel using standard soft lithography method described as follows: The 2-inch silicon wafer is RCA cleaned and the negative photoresist (SU8-2050) is spin-coated on the silicon wafer. The silicon wafer with photoresist is prebaked on a programmable hot plate at 65°C and 95°C for 3 minutes and 9 minutes, respectively. The photomask having the pattern of the microfluidic device is prepared using a laser writer (LW405, Microtech Inc). The photomask and silicon wafer are aligned with each other using mask aligner (Karl Suss MJB4) and subjected to ultraviolet radiation with an intensity of 220 mJ/cm<sup>2</sup>. The silicon wafer is then post-baked on a hot plate at 65°C and 95°C for 2 minutes and 7 minutes, respectively, later developed using SU8 developer for 15-20 minutes and finally hard-baked at 150°C for 10 minutes. PDMS (Dow Corning, Sylgard 184) 20 parts are mixed with 1 part of curing agent, the mixture is poured on the mold and bubbles are removed by keeping it in a desiccator for 2 hours. The mold and clean glass slide are both bonded by subjecting them to oxygen plasma for 18 seconds.

Droplets are generated in a continuous phase of paraffin oil using standard T-junction. Stream of monodispersed droplets is used as a substitute for mother droplets of different samples or composition. The flow of paraffin oil and de-ionised water is driven by two syringe pumps (New Era pump systems Inc, USA). The valves are actuated with a pressurised air supplied with a fluigent system (model MFCS<sup>TM</sup>-EZ). A Fluigent system can control the pressure in a range of 0 to 2 bar. The surface tension between water and paraffin oil is measured using a spinning drop tensiometer (Dataphysics Inc, SVT20) yielding a value of 30 mN/m,

interfacial tension along with the oil viscosity (0.022 Pa.s) and the velocity of the droplets are used to calculate the Capillary number. Generated mother droplets interact with the pair of splitting junctions. The droplet interactions are recorded by using a high-speed camera at 300 frames per second (Motion Pro Y3, IDT Inc, USA) fitted with a long-distance working objective (Qioptiq Inc., Germany). The velocity of the generated droplets, volume of the mother droplet and daughter droplet after breaking up are calculated using image processing.

### 3.2.2 Simulation Setup and Grid Independence Study

Numerical simulations are carried out using commercial software Ansys Fluent. To save computational expense, rather than simulating the generation of droplets, we initialized the simulation with multiple cuboids of de-ionised water along the length of the main channel. These cuboids of de-ionised water have the same volume and separation distance as observed in experiments. Surface tension effect causes these cuboids to turn into the shape of a droplet. We imposed a uniform velocity boundary condition at the inlet while at both outlets, a pressure outlet (atmospheric pressure) boundary condition is used. At the wall, we used a no-slip boundary condition and equilibrium contact angle of  $140^\circ$ . The cartesian structured mesh is generated using commercial software ICEM (Ansys Inc.). Structured grid with refinement is used near the entrances of both the junctions and the wall. At other locations, a coarse grid is used. A variable time step is used in all the simulations; time step for transient simulations is decided based on the Courant number, fixed at 0.5. Fluid properties of oil and water are same as the experimental values.

**Figure 3.2** shows the grid independence test in the regime with no droplet breakup at both the junctions. We used three different mesh refinements of  $\Delta S = 1 \mu\text{m}$ ,  $2 \mu\text{m}$ ,  $3 \mu\text{m}$  near the wall of the microchannel and close to both the junctions. The minimum grid size was kept similar in x, y and z directions. The finger length ( $L_f$ ) of droplets when it interacts with the first and second junction along with the details of the grid size independence test are shown in **Table 3.1 and Figure 3.2**. As the error in the second case is just 1.5% and 0% compared to the finest grid of  $1\mu\text{m}$  for  $L_f$ ,  $\Delta S = 2 \mu\text{m}$  was used in the simulations. We found that for the refinement of  $2 \mu\text{m}$ , we got reasonable accuracy.

Case	$\Delta S$	Number of Cells	% error in $L_f$ compared to case 3 in the first junction	% error in $L_f$ compared to case 3 in the second junction
1	$3 \mu\text{m}$	$0.6 \times 10^6$	4.6%	5%

2	2 $\mu\text{m}$	$0.83 \times 10^6$	1.5%	0%
3	1 $\mu\text{m}$	$1.2 \times 10^6$	-	-

**Table 3.1:** Grid size independence study showing error in finger length ( $L_f$ ) compared to the finest grid.

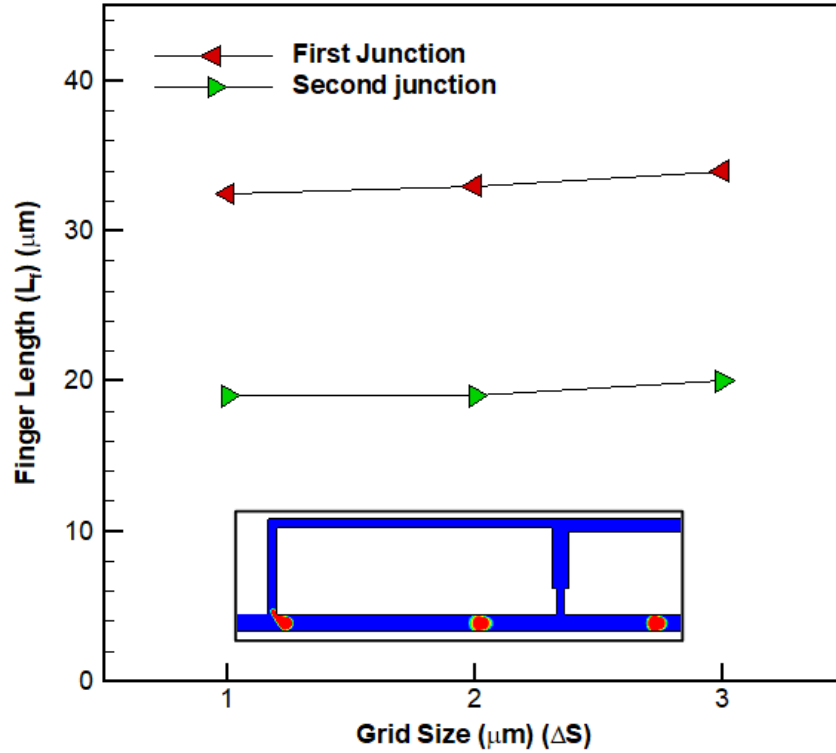


**Figure 3.2:** Grid size independence study showing finger length ( $L_f$ ) vs minimum grid size ( $\Delta S$ ) for droplet interaction with the first and second junction.

### 3.3 Results and Discussion

( $Q_{\text{continuous phase}}/Q_{\text{discontinuous phase}}$ ) is fixed at 1 in all the experiments. The range of flow rates used is 2 to 16  $\mu\text{L}/\text{min}$ , resulting in droplets of volume between 0.6 and 1 nL (or 220 and 180  $\mu\text{m}$  droplet length). We start by analysing the nature of these droplet interactions with two T-junctions downstream and then examine the conditions and regimes of droplet breakup.

#### 3.3.1 Two Identical T-Junctions

Firstly, we examine the interaction of droplets with two identical T-junctions, each connecting to the outlet channel by channels of 50  $\mu\text{m}$  width, as shown in **Figure 3.3**. When the droplet interacts with the first junction, we observe daughter droplet being generated. However, with the second junction, no breakup occurs, for all the flow conditions.

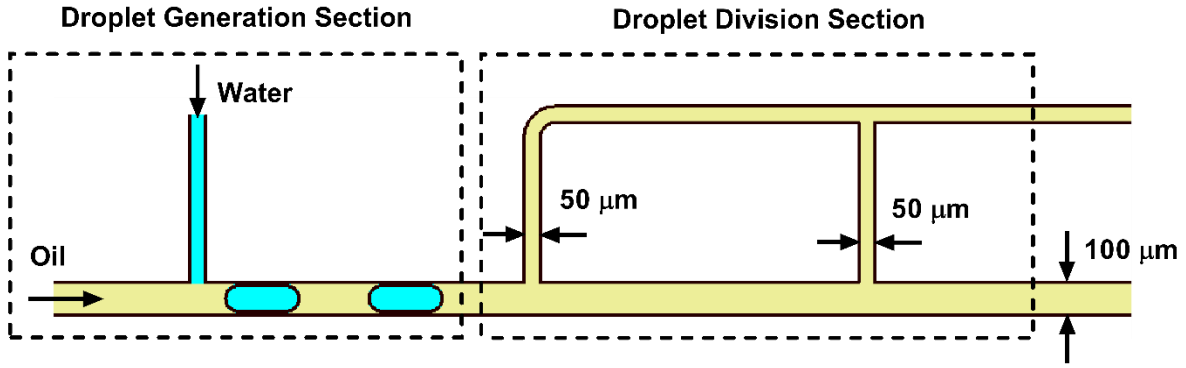


**Figure 3.3:** A schematic of microfluidic system design with upstream droplet generation section followed by two stage droplet division section. Mother droplets are produced upstream and are made to interact with identical droplet division junctions.

**Figure 3.4 a** show a sequence of images of droplet breakup at the first junction (Capillary number ( $Ca$ ) is 0.01). When the mother droplet passes the first junction, a finger is formed into the branch, the length of which increases with time, which ultimately breaks to form a daughter droplet. **Figure 3.4 b** shows image sequence from the second junction, where the finger can be seen to be shorter and retracts without breakup. When the finger length is analysed for both junctions, consistently across all flow rates, this metric is more significant for the first junction. The shear force acts on the finger, resulting from flow past it into the branch channel, this shear will be higher for larger flow rates; hence a smaller finger length is required for break up [148]. When the droplet moves past the first junction; there is a considerable amount of flow rate reduction, which causes altered flow conditions at the second junction. It can be seen in **Figure 3.4 c and d**, in which the daughter droplet volume produced at the first junction is shown, despite the shorter finger created at higher flow rates, the droplet does not decrease commensurately. This is partly attributable to the shear acting on the finger, which acts to prevent its retraction. Besides, there is simply less time for retraction to take place before the breakup. Finally, it is worth noting that the plotting is of percentage volume concerning mother droplet volume and that at higher flow rates, smaller mother droplets are produced, which contributes to a shorter finger length. We can conclude that the finger lengths grow with time; hence the size of the mother droplet will have a significant impact on the finger length. The shear produced on the finger by the flow at higher flow rates lowers the length required for break up.

As a result, we can conclude that the finger lengths grow with time; hence the size of the mother droplet will influence the finger length. The shear produced on the finger by the flow at higher flow rates lowers the length required for break up to occur. But most importantly,

we also conclude that the behaviour of the two junctions is very different; hence there can be no expectation that there is a flow condition which could provide a knife-edge condition (between the breakup and no breakup) at both junctions simultaneously. As such, this design would not lend itself well to selective droplet breakup at multiple locations. Hence, we are discarding this design.

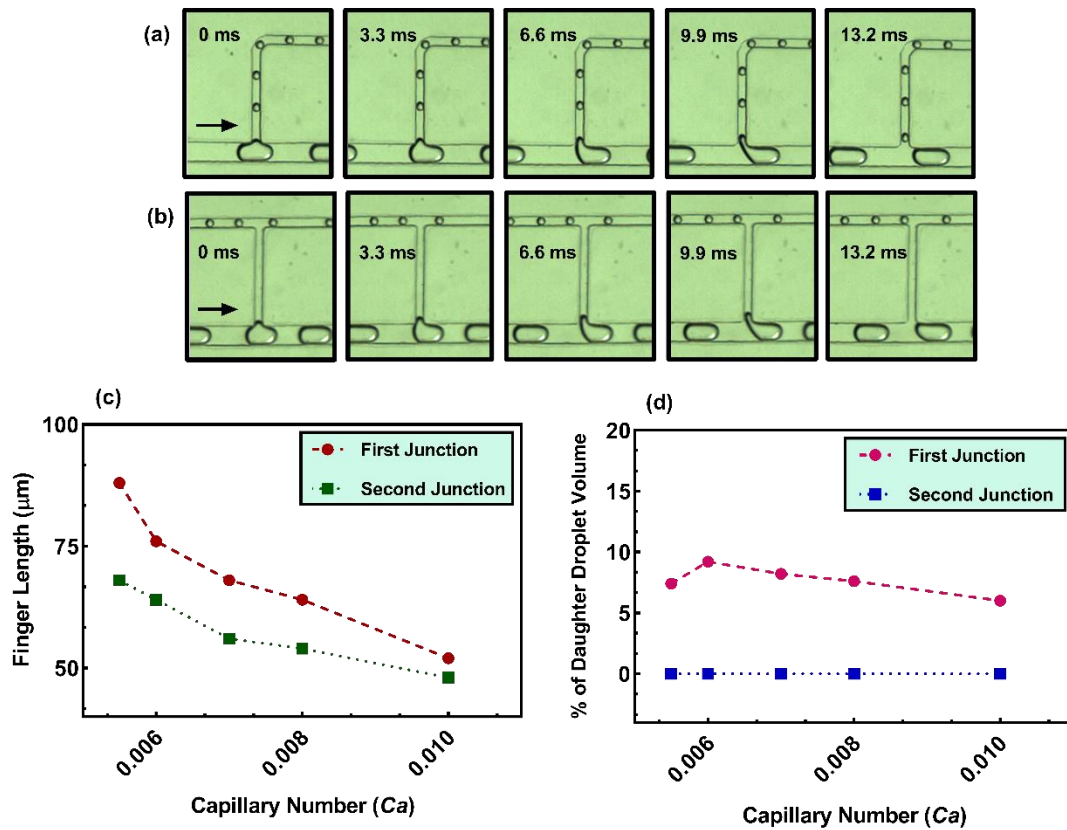


**Figure 3.4:** High-speed visualization, at a capillary number (Ca) of 0.01, of a mother droplet interacting with the (a) first and (b) second junctions. In which a finger is seen to develop in the branch and either break into a droplet or retract. The discrepancy, between the two junctions, of the maximum length of the finger length (c) and the (d) percentage of the volume of the mother droplet which breaks into a daughter droplet is seen across the Ca range tested.

### 3.3.2 Resistance Network Analysis for Channel Design

We now analyse the microfluidic system in a detailed manner, to design it, in such a way that the droplet interaction is the same at both junctions. We have conducted a theoretical examination of the flow distribution in the first and second junctions using an electric circuit analogy [149], which will yield the relative flow rates around the chip and controls the size of the finger. To predict the flow rate distribution with least complexity, we considered only



continuous phase and not droplets (having finite hydrodynamic resistance) in the microfluidic system.

The microfluidic system can be considered as a resistive network, where flow rate ( $Q$ ) is equivalent to current, potential difference is equivalent to the pressure drop ( $\Delta P$ ) and resistance is equivalent to the hydrodynamic resistance of the microchannel. **Figure 3.5** shows the existing microfluidic geometry with hydrodynamic resistance in each branch. The height of microchannel is kept constant at 60  $\mu\text{m}$ .

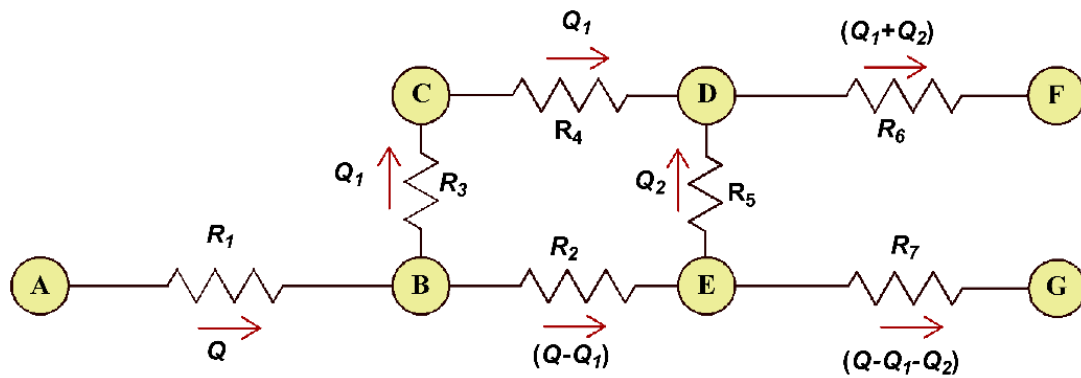


**Figure 3.5:** The Resistance network of the microfluidic system with the associated flow rate distribution of the continuous phase, without considering the resistance of the droplets.

The hydrodynamic resistance is calculated using the equation below,

$$R = \frac{12\mu l}{wh^3 \left[ 1 - 0.63 \left( \frac{h}{w} \right) \right]} \quad 3.1$$

$$R = al \quad 3.2$$

$$\text{Where } a = \frac{12\mu l}{wh^3 \left[ 1 - 0.63 \left( \frac{h}{w} \right) \right]}$$

Where  $w$ ,  $h$ ,  $l$ ,  $\mu$  are width, height, length of the channel and viscosity of the continuous phase, respectively. Kirchhoff's junction law, which states that net charge entering the junction is equal to that of going away from the junction. To find out current in each branch, we have used Kirchhoff's loop law which states that the algebraic sum of all the potential differences along a closed loop is zero.

Applying Kirchhoff's loop law for the first loop,

$$R_2(I - I_1) + R_5I_2 - R_4I_1 - R_3I_1 = 0 \quad 3.3$$

$$R_2 I - R_2 I_1 + R_5 I_2 - R_4 I_1 - R_3 I_1 = 0 \quad 3.4$$

$$R_5 I_2 = (R_2 + R_3 + R_4) I_1 - R_2 I \quad 3.5$$

Converting the equation in terms of flow rate (Q), we get

$$R_5 Q_2 = (R_2 + R_3 + R_4) Q_1 - R_2 Q \quad 3.6$$

$$R_5 = \left[ \frac{(R_2 + R_3 + R_4) Q_1 - R_2 Q}{Q_2} \right] \quad 3.7$$

$$R_5 Q_2 = (R_2 + R_3 + R_4) Q_1 - R_2 Q \quad 3.8$$

$$R_5 = \left[ \frac{(R_2 + R_3 + R_4) Q_1 - R_2 Q}{Q_2} \right] \quad 3.9$$

We have fixed the value of  $R_2$ ,  $R_3$ , and  $R_4$ ;

$$a = \left[ \frac{(R_2 + R_3 + R_4) Q_1 - R_2 Q}{Q_2 l_5} \right] \quad 3.10$$

As both the outlets (F and G) are subjected to atmospheric pressure condition, we can say that

$$P_A - P_F = P_A - P_G$$

$$(P_A - P_B) + (P_B - P_E) + (P_E - P_G) \quad 3.11$$

$$= (P_A - P_B) + (P_B - P_E) + (P_E - P_D) + (P_D - P_F)$$

$$(P_E - P_G) = (P_E - P_D) + (P_D - P_F) \quad 3.12$$

$$(Q - Q_1 - Q_2) R_7 = R_5 Q_2 + (Q_1 + Q_2) R_6 \quad 3.13$$

$$(Q - Q_1 - Q_2) R_7 = a(l_5 Q_2 + l_6 Q_1 + l_6 Q_2) \quad 3.14$$

$$a = \frac{R_7(Q - Q_1 - Q_2)}{l_5 Q_2 + l_6 Q_1 + l_6 Q_2} \quad 3.15$$

For flow rate entering both the junctions is same

By simplifying equation 1.24 and 1.29, we get

$$5a Q_1 = (33 \times 10^{17} Q_1) - (4.29 \times 10^{17} Q) \quad 3.16$$

$$109a Q_1 = (13.9 \times 10^{17} Q) - (27.8 \times 10^{17} Q_1) \quad 3.17$$

We have fixed all the dimensions of the channel except the width of the second branch ( $w_{b2}$ ).

By solving equations for flow rate condition of  $Q_I = Q_2$ ,

$$a = 6.42 \times 10^{16}$$

$$Q_1 = 0.1436 Q$$

From  $a$  and  $Q_1$  we get

$$w_{b2} = 64 \mu\text{m}.$$

However, we are interested in the formation of droplets at these junctions, and we have already seen the importance of the finger formed before breaking up and location at which finger forms. Instead of using the value of  $64 \mu\text{m}$ , we change the channel in a way to maintain the equivalent resistance. The channel geometry for branch five is set such that it has the same opening ( $50 \mu\text{m}$ ) as branch 2 for a distance larger than the longest finger we expect ( $100 \mu\text{m}$ ) and then expands such that the overall resistance is equal to that calculated. The resulting geometry is shown in **Figure 3.6**. By having this geometry, we can directly compare finger lengths in both the junctions and droplet trapped in both the junction will be subjected to same Laplace pressure [148].

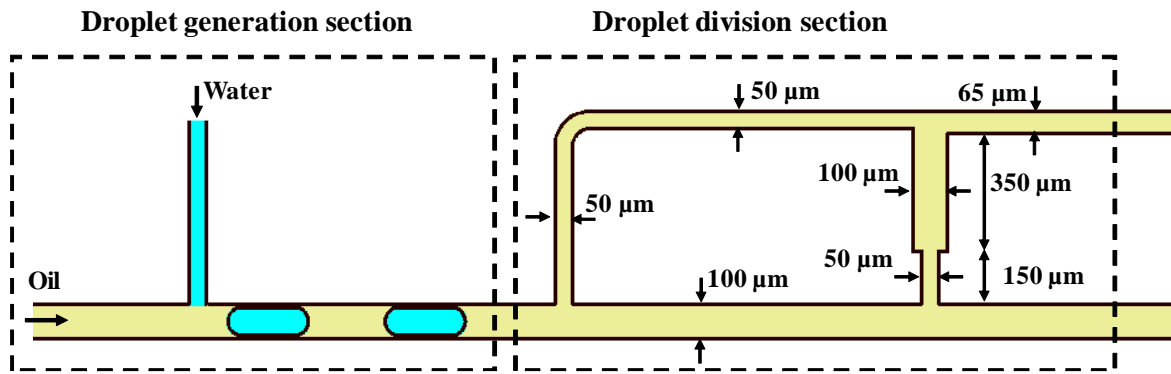


**Figure 3.6:** A schematic of a microfluidic system with upstream droplet generation section followed by droplet division section, designed such that the behaviour at each splitting junction is balanced. To achieve this the second junction consists of a section of channel with the original width, followed by an expansion which drops the overall resistance of the branch.

### 3.3.3 Expansion Channel for Control of Droplet Division

With the channel redesigned to match the flows in the two branches, albeit in the absence of droplets, we reassess the droplet interactions at the junctions to these branches. In contrast to the first design, we observe a range of behaviours. **Figure 3.7** shows five different regimes, the finger lengths for each of which are shown in **Figure 3.8**:

a) In the first regime, droplet develops a small finger which penetrates in the junction, recovers its original shape and moves into the main channel without breaking up in the first and second junction as shown in **Figure 3.7 (a)**. We call this regime as “no breakup in both junctions.”

- b) In the second regime, we observe that droplet breaks up in the first junction while there is no droplet breakup in the second junction, as shown in **Figure 3.7 (b)**. We call this regime as “breakup in the first junction.”
- c) In the third regime, we observe droplet breakup in both junctions, but the volume of daughter droplet formed in the second junction is much smaller than that of the first junction, as shown in **Figure 3.7 (c)**. We call this regime as “breakup in first junction onset of breakup in the second junction.”
- d) In the fourth regime, we observe droplet breakup in both the junctions, but the volume of daughter droplet formed in the second junction is more than that of the first junction, as shown in **Figure 3.7 (d)**. We call this regime as “breakup in both junctions.”
- e) In the fifth regime, we observe intermittent breakup in both junctions. By intermittent breakup, we mean we do not observe daughter droplet continuously forming in both the junctions. Out of 10 droplets interacting with the first and second junction only 3 to 4 droplets break into the first and second junction, as shown in **Figure 3.7 (e)**. We call this regime as “intermittent breakup.” The finger length for this regime is not shown in **Figure 3.8** as it is not consistent across each droplet.

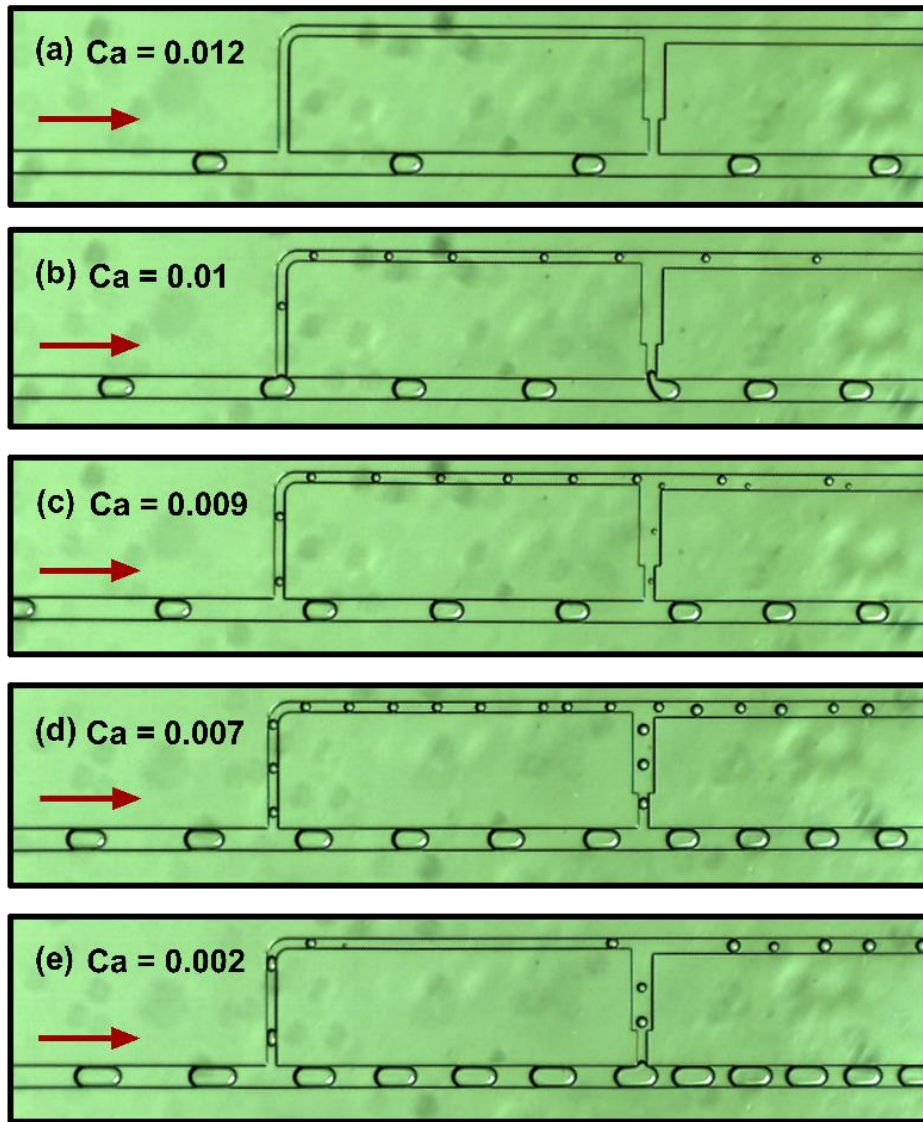


**Figure 3.7:** High-speed visualization of droplet interaction with straight channel branching from the first junction and the expansion channel stemming from the second junction (see appendix C, video C1). Five regimes are observed: (a) No droplet breakup in both junctions, (b) Breakup in the first junction, (c) Breakup in first junction onset of breakup in the second junction, (d) Breakup in both the junctions. (e) Intermittent breakup in both the junctions.

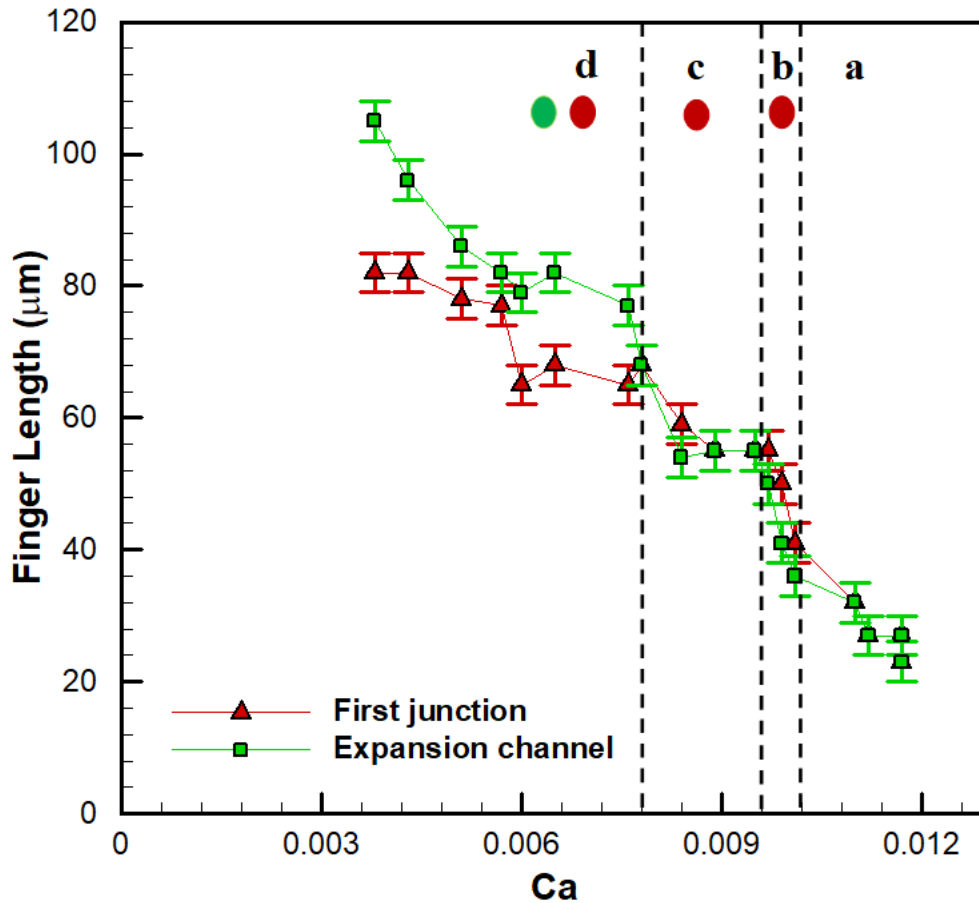


**Figure 3.8:** The finger length for four regimes of droplet interaction is plotted against  $Ca$ . The finger length from regime e (intermittent breakup regime) is not plotted as it is not consistent across each droplet. The dots below the regime letters indicates whether break up at the first (red) and second (green) junction occurs.

Clearly, by changing the chip design such that the branch flows are similar, we have made the behaviour of the droplets similar under some conditions. In **Figure 3.9**, the finger length is shown as a function of time for each of the two designs. We see that the flow equalization in the branches in the second design makes for much similar finger growth across the two channels, thus linking the role of branch flow with finger length.

We see that in this range, there will be a flow condition where we will get the same size of the daughter droplet volume in both junctions. With a slight change in flow conditions, we can either have regime (a) or regime (c). As the continuous phase flow rate is increased further (increase in  $Ca$ ), we again start to get different daughter droplet volumes where the volume of daughter droplet formed in the second junction is higher than the first T-junction. Clearly, in this design, it is possible to obtain very similar behaviour at each junction, either no droplet at each or droplets of the same size (**Figure 3.10**). Here, we move between these results by altering the imposed flow; however, for the selective break-up, we will have a fixed flow rate

and will seek to vary behaviour by local alteration of geometry. By starting with the same behaviour at each junction, we will now seek to alter that behaviour in just one of the junctions by changing the local geometry.

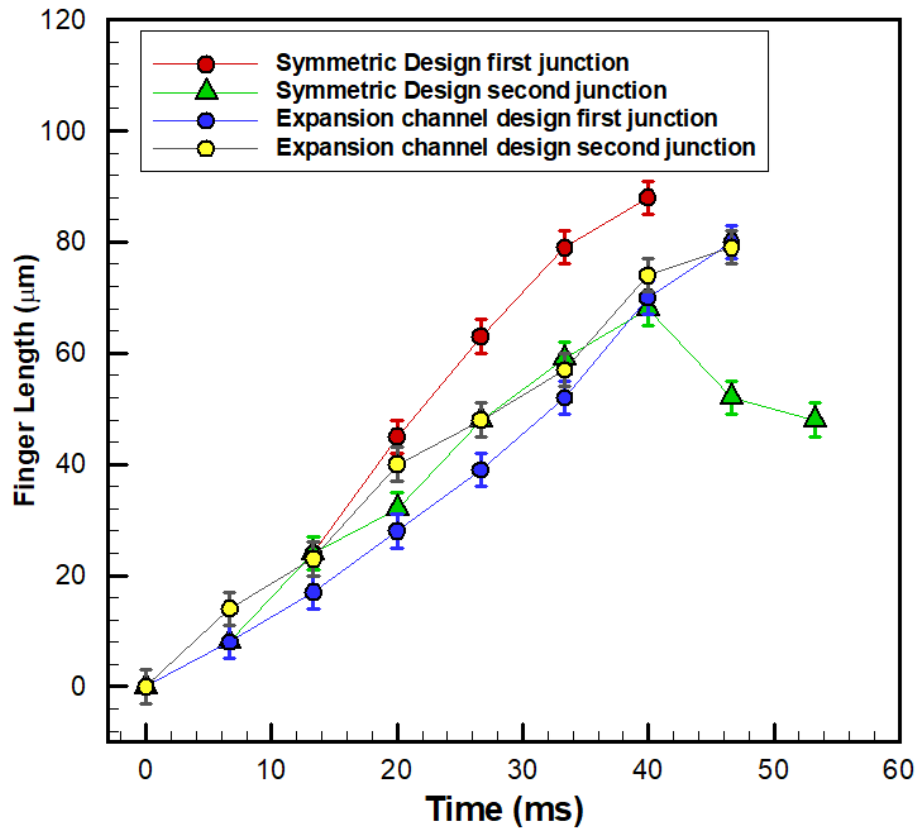


**Figure 3.9:** The evolution of finger length measured in the first and second junction for both the designs (symmetric and expansion channel) as a function of time under the same flow conditions ( $Ca = 0.0055$ ). Case of symmetric design second junction yields no breakup while all other cases represent breakup.

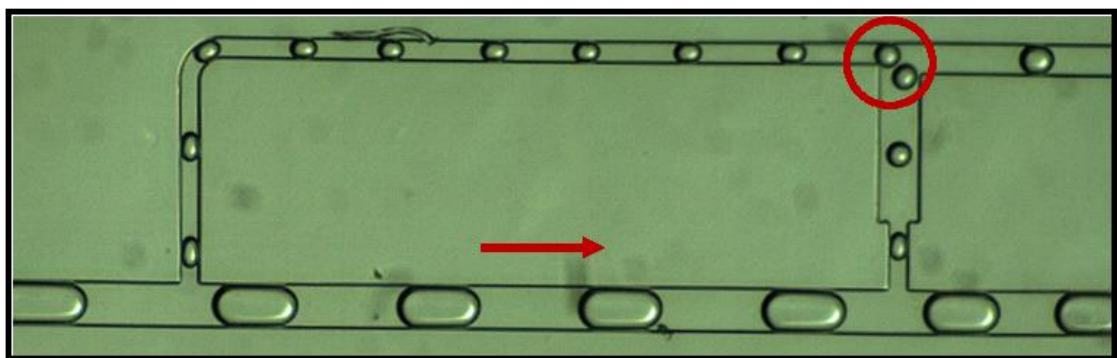


**Figure 3.10:** High-speed visualization of droplet interacting with the first T-junction and expansion channel, which yields the same volume of daughter droplets at both the junctions. This lies between regime 3 and 4.

### 3.3.4 Selective Droplet Breakup at Two Junctions

#### 3.3.4.1 Two Valve System Using Simulations

We compare results of numerical simulations at first and second junction in ‘regime a’ where there is no droplet breakup in both the junctions with the experimental results in the same regime specifically at  $Ca = 0.011$ . The separation distance between the droplets is kept similar to that measured in experiments. The length of the mother droplet in the simulation was matched to that observed in the experimental work. The shape of the droplet interfaces obtained at different times is in very good agreement with those recorded in the experiments (Shown in **Figure 3.11**). The experimentally measured maximum finger length is  $27\ \mu\text{m}$  while the numerical value is  $33\ \mu\text{m}$ . Overall, the numerical results capture ‘regime a’ with reasonable accuracy, this benchmarking allows us to examine the deformation of channel wall similar to that of single-layer microvalve at two locations.

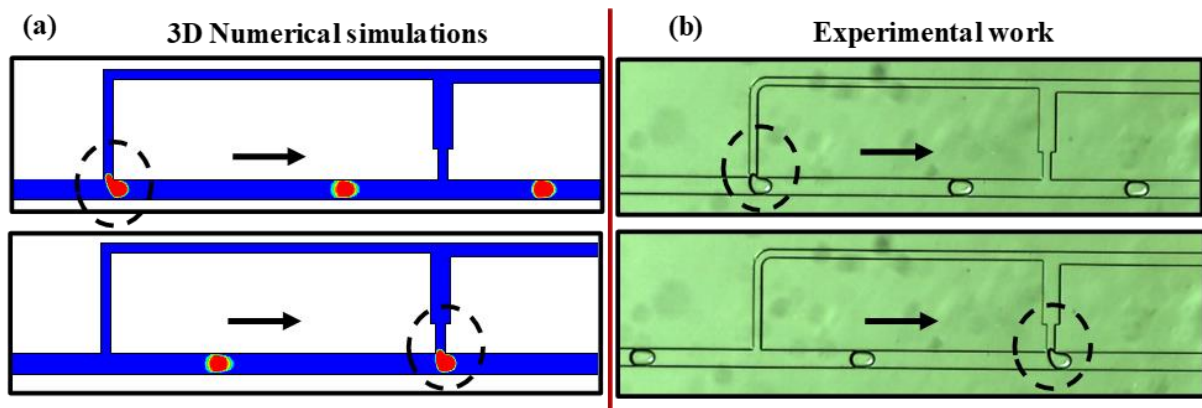


**Figure 3.11:** Comparison between experimental and 3D numerical simulations at  $Ca = 0.011$ . (a) Contours of the volume fraction of the continuous and discontinuous phase. (b) High-speed visualization of the droplet interaction with the first and second junction.

To be able to screen using permutations of reactions, we would like to have a selective breakup of droplets at different locations, in this way the mother droplet becomes the fluid in a pipette and the intervention becomes equivalent to depressing the pipette plunger. We have previously demonstrated selective breakup of mother droplet at a single location using a single layer microvalve [141], here, the change in local geometry moved results from a non-break up to a breakup regime. We turn to simulation to explore whether similar geometric changes can be used on this system with two junctions and balanced flows. We start by selecting the imposed flow condition, which places the system at the knife-edge between regime a and b.



Subsequently, we change the wall shape such that there is an occlusion at the entrance to one of the junctions (as occurs when a single layer valve is partially closed). The wall deformation is assumed to be semi-elliptical with a major axis of the ellipse set as 500  $\mu\text{m}$ , and the semi-minor axis is varied from 0 to 60  $\mu\text{m}$ . Dimensions of the deformation are similar to the dimensions used by Raveshi *et al.* [141] in their experiments.

In the first set of simulations, **Figure 3.12**, we introduced semi-elliptical deformation in the main channel at the entrance of the first branch. The semi-minor axis of deformation is varied from 0 to 60  $\mu\text{m}$ . **Figure 3.12** shows the regularity of droplet breakup, for deformations above 30  $\mu\text{m}$  this is 100%. Insets of **Figure 3.12** show droplet interaction with deformation of 0 and 60  $\mu\text{m}$ . It is worth noting that here we make a fixed geometrical change, when operating a valve, it is possible to switch the deformation rapidly, the requirement is that when this is done the next drop breaks up, hence 100% is required, but the valve would only be operated for the time that a single mother droplet passes the junction.

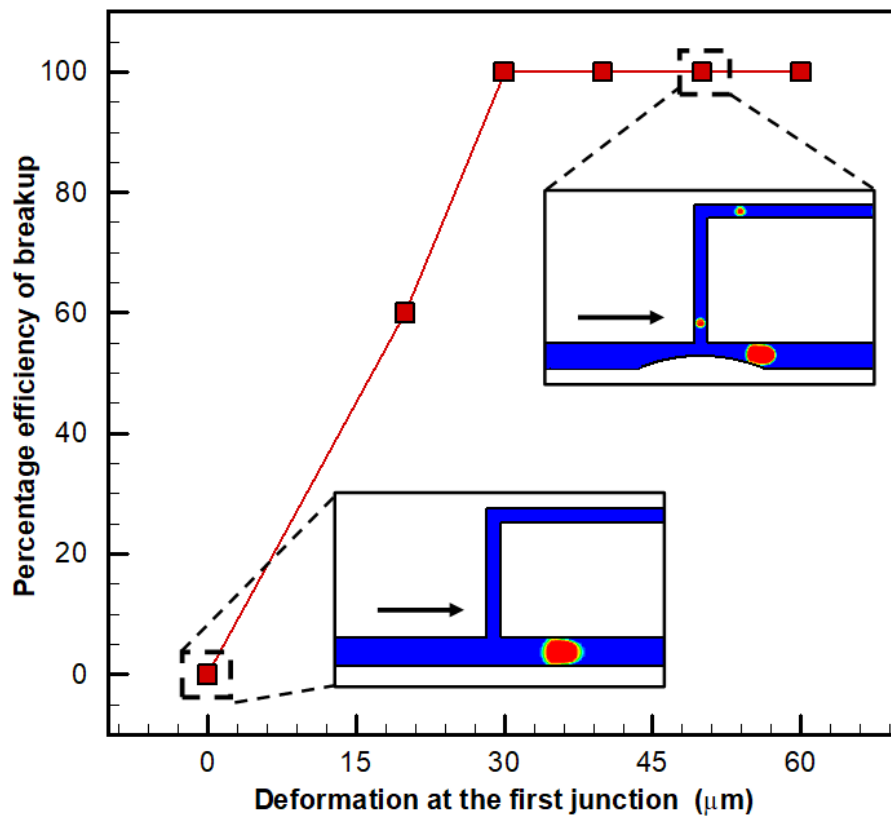


**Figure 3.12:** Percentage efficiency of droplet breakup in the first junction against deformation at the entrance of the first junction calculated using numerical simulations. Bottom inset shows a top view of the 3D numerical simulation without deformation at the entrance of first junction resulting in no breakup. The top inset shows a top view of the 3D numerical simulation with deformation of 50  $\mu\text{m}$  at the entrance of first junction resulting in a breakup (see appendix C, video C1).

In the second set of simulations, we introduced semi-elliptical deformation in the main channel at the entrance of the second junction. The deformation is varied from  $0\ \mu\text{m}$  to  $60\ \mu\text{m}$ . We observe that with these deformations we do not get droplet breakup in the second junction, but instead get breakup at the first junction. The deformation at the entrance of the second junction causes the hydrodynamic resistance of both  $R_2$  and  $R_7$  to increase. This increase in hydrodynamic resistance of  $R_2$  causes the droplet to break in the first junction. To avoid this, we changed the location of deformation slightly downstream from the entrance of the second junction, such that it only causes an increase in the resistance of channel 7. **Figure 3.13** shows the efficiency of droplet breakup for different values of deformation and two different designs: that of two identical junctions and expansion channel. We observed in expansion channel design, for the deformation of  $20\ \mu\text{m}$  and  $30\ \mu\text{m}$  droplet breakup efficiency is found to be  $0\%$ , as deformation is increased to  $40, 50, 60\ \mu\text{m}$  we start getting an efficiency of droplet breakup to  $90\%, 90\%$  and  $100\%$  respectively. While in case of identical second junction even at the deformation of  $60\ \mu\text{m}$  we do not observe droplet breakup.

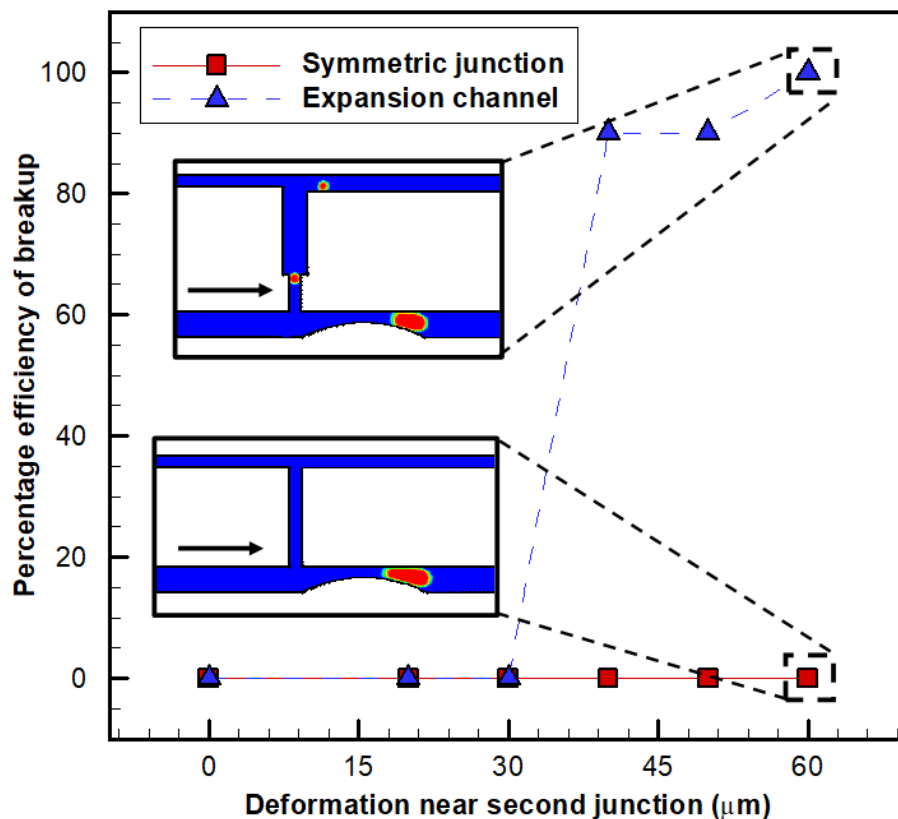


**Figure 3.13:** Percentage efficiency of droplet breakup in the second junction and expansion channel against deformation near the entrance of the second junction calculated using numerical simulations. Bottom inset shows a top view of the 3D numerical simulation with deformation of  $60\ \mu\text{m}$  for symmetric

second junction resulting in no breakup. The top inset shows a top view of the 3D numerical simulation with deformation of 60  $\mu\text{m}$  for expansion channel resulting in a breakup (see appendix C, video C2).

#### 3.3.4.2 Two valve system using experiments

To demonstrate the capability of selective droplet break-up at two locations, we fabricated a system with two single-layer microvalves. Each valve separates a dead-end channel from the main channel by a membrane of 30  $\mu\text{m}$  thickness. Application of pressure using Fluigent system in the dead-end channel causes deformation of the membrane constricting the main channel. The location of the first valve is at the entrance of the first junction while we tried two different locations for the second valve (one at the entrance of the second junction and other away from the second junction). The microfluidic system is operated in ‘regime a’ (no breakup in both the junctions) when the valve is not activated. For selective droplet breakup in the first junction, the valve is pressurized systematically from 0 mbar to 1600 mbar.

**Figure 3.14 a** show the image sequence for the conditions of no valve actuation, actuation at 1200 mbar and 1600 mbar pressure at the first junction. We do not observe droplet breakup, when valve pressure is below 1300 mbar, at 1400 mbar efficiency of droplet breakup is just 5%, and for valve pressure equal to and above 1500 mbar droplet breakup efficiency is 100% as shown in **Figure 3.15**. Each of **Figure 3.14 (b) and (c)** shows the high-speed visualization for three conditions, those of no valve actuation, actuation at 1200 mbar and 1600 mbar pressure, with the valve located (b) at the entrance second junction and (c) downstream from the second junction. We observe that the location of the valve away from the second junction is far more efficient than at the entrance of the second junction. For the valve location away from the second junction, the efficiency of 100% is achieved after the pressure of 1000 mbar. While for the other location to get the efficiency of 100% pressure of 1500 mbar is required.

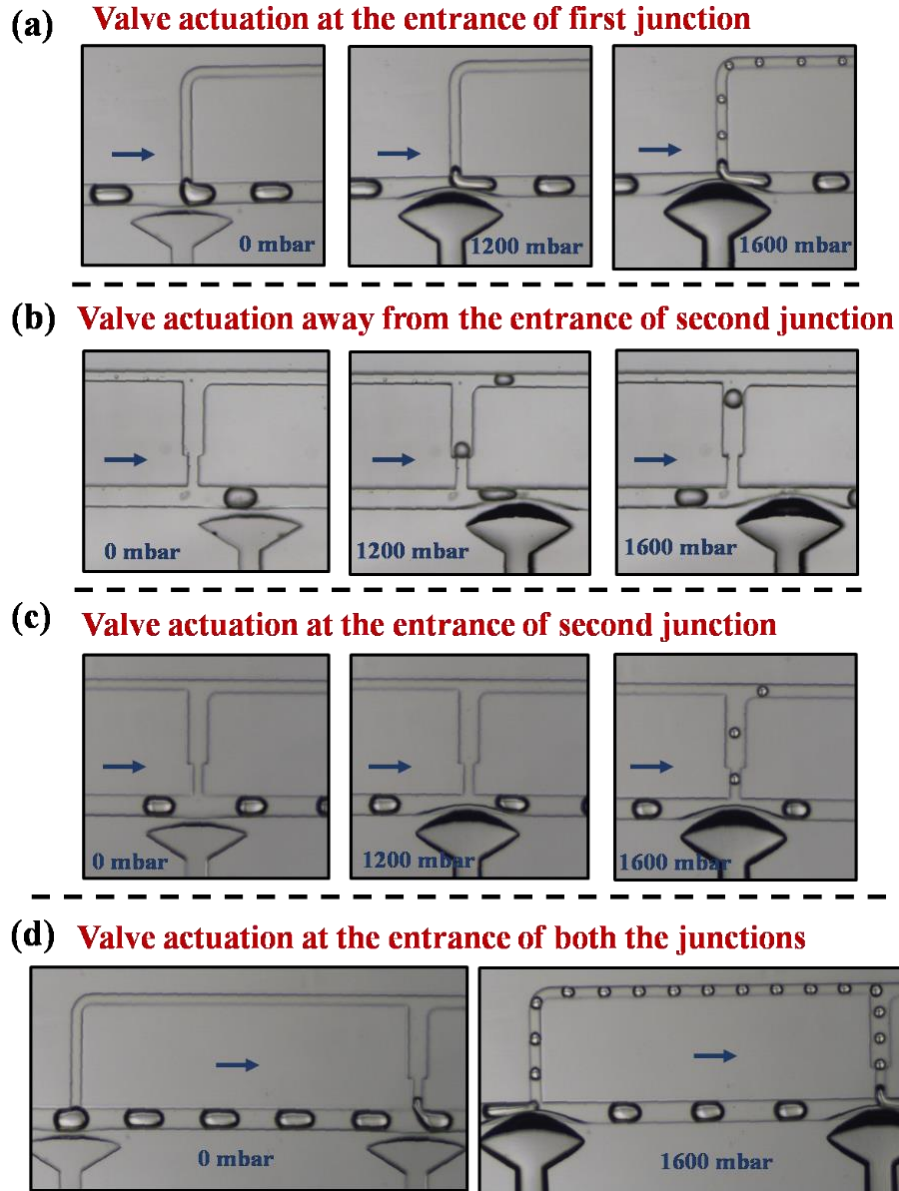


**Figure 3.14:** High-speed visualization showing the interaction of droplets with two junctions in the presence and absence of valve actuation. **(a)** Actuation of valve for the first junction **(b)** Actuation of the valve for the second junction with the valve away from the entrance of second junction **(c)** Actuation of the valve for the second junction with the valve at the entrance of second junction **(d)** Actuating both the valves simultaneously.

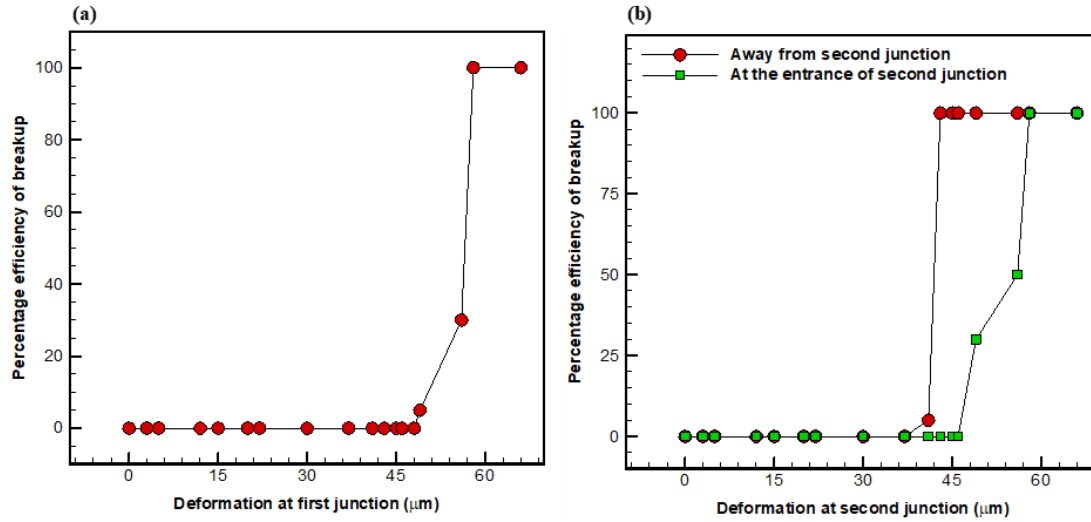


**Figure 3.15:** Percentage efficiency of droplet breakup vs valve deformation for (a) first junction (b) second junction with two valve locations.

While comparing simulation results with experiments for deformation caused due to valve actuation at the first junction, the trend is similar in both cases. Simulations give the efficiency of 100% for 30  $\mu\text{m}$  deformation, while experiments show that full efficiency is reached after the deformation of 56  $\mu\text{m}$ . Similarly, simulations give efficiency of over 90% above the deformation of 40  $\mu\text{m}$ , while experiments show that this efficiency is achieved after the deformation of 45  $\mu\text{m}$  at the second junction. Results obtained from simulations are in close agreement with the experiments when we are not operating the valve. However, when we are operating the valve, the simulation results under predict the deformation compared to experiments. There are two reasons: 1) the actuation of the valve causes much more pressure variations in the microchannel due to its dynamic nature contrary to having a static deformation in the simulations. 2) It is challenging to get the exact shape of the deformed interface in the simulation.

### 3.4 Closure

We analyse the droplet behaviours in a microfluidic system with two junctions, seeking to find the underlying requirements for selective droplet breakup in more than one location. We used resistive network analysis to design the microfluidic system, so that same flow rate of continuous phase enters both the junctions. With this achieved, we observed that under certain flow conditions, the droplet interaction with both junctions was similar, which allowed a critical operational condition to be selected at which break-up does not quite occur. We then

showed the design requirements for the location of microvalves, simulated by deformations of the channel wall, such that we can alter the break-up condition at just one of the junctions. Taken as a whole, this work shows the design and experimental route to selective droplet breakup at multiple locations on a chip.

# Chapter 4

## 4 Controlled Droplet Manipulation and Interaction using Single Layer Microvalves

*In the last two chapters, we investigated the knife-edge condition separating droplet breakup and no breakup at single and two locations. Later we used single-layer microvalves to change the behaviour from no droplet breakup to droplet breakup. In this chapter, we integrate droplet generation, breakup and merging on the same microfluidic chip. We use multi splitting/breakup and merging system to perform permutations of reactions required for high-throughput screening using multiple single-layer microfluidic valves. We generate four different coloured droplets using four single-layer microfluidic valves located in the droplet generation section. These different coloured droplets are split selectively at four different junctions using valves located close to each junction. We used pillar induced merging to demonstrate various functions like merging of two similar coloured droplets, two dissimilar coloured droplets in same/different concentration and selective merging of two different coloured droplets at all the four junctions, bringing high-throughput screening one step closer to the ideal miniaturised version implemented on the microfluidic chip.*

### 4.1 Introduction

Droplet-based microfluidics involves the generation of monodisperse droplets of nL to fL volumes separated by an immiscible carrier fluid. As a carrier fluid separates each droplet, it offers isolation of droplets against cross-contamination; hence samples and reagents can be encapsulated in a droplet. These microsystems provide accurate droplet volumes, reliable droplet manipulation, faster reaction times with reduction in the cost of samples, reagents thus is instrumental in the screening processes in biological and chemical applications. Droplet-based microfluidics finds applications in various fields such as single-cell analysis [14,150], protein crystallization [10,151], nanoparticle production [102,152], inorganic chemistry [19], chemical and biological assays [17,18], clinical diagnosis [12,13], reaction kinetics [9] and high throughput screening (HTS) [23,137,138].

For HTS on-chip, it is necessary to generate different kind of droplets on demand, divide the droplet selectively at multiple locations and merge combinations of droplets on the chip at will. Some of the tasks such as the production of droplet pairs [126,153,154], splitting [56,57] and merging [106,129] have been individually demonstrated. Various researchers used passive and active methods to manipulate the droplet on the chip. Combination of active and passive methods offers better control over droplet manipulation compared to individual methods. It has been previously demonstrated the use of electric forces [63] at splitting junction to control the droplet generating, merging and sorting. Others used lasers [73], micro heaters [75] along with the passive techniques to manipulate droplets; however, these active methods are not biocompatible. Surface acoustic waves (SAW) along with the splitting T-junction has also been used to split and merge the droplet [80]. Though SAW is biologically compatible, there are other issues like the complexity and cost of equipment, slow nature of response which prompts the need of other active methods for droplet manipulation. Single-layer microvalves [88,93] have been used in the field of droplet microfluidics. These valves are biocompatible, simple, easy to fabricate, and several valves can be integrated on a PDMS microfluidic chip. Single-layer microvalves also have a fast response time close to 0.05s [141]. These valves have been used for droplet generating [31], splitting [155], sorting [156] and merging [115], but not all on the same chip, simultaneously.

Our motivation in this study is to introduce different chemicals in different droplets on-chip and develop a method which can selectively break and merge droplets at multiple locations, simultaneously. By doing this, we show that small volumes of samples and reagents can be delivered at multiple locations and can be reacted with each other, which is essential to bring HTS onto the chip. To develop this, we used a valve-based approach (shown in **Figure 4.1**). Previously, we investigated the behaviour of droplets at the entrance of a bypass channel and figured out the regimes of droplet breaking against the flow conditions [148]. Then with the understanding of breakup regimes, we demonstrated selective droplet breakup at the entrance of bypass channel using one single-layer microvalve [141]. We extended this study for two junctions and used two single-layer microvalves to divide droplets at two locations [155]. Here, we used a total of eight single-layer microvalves. For the generation of four different kinds of droplets upstream, we used four valves; remaining four valves were used to split droplets at four T-junctions downstream. We used pillar induced merging of the split droplets to have multiple reactions and combinations on a chip. This demonstration has the potential to have HTS on-chip with much smaller volume.



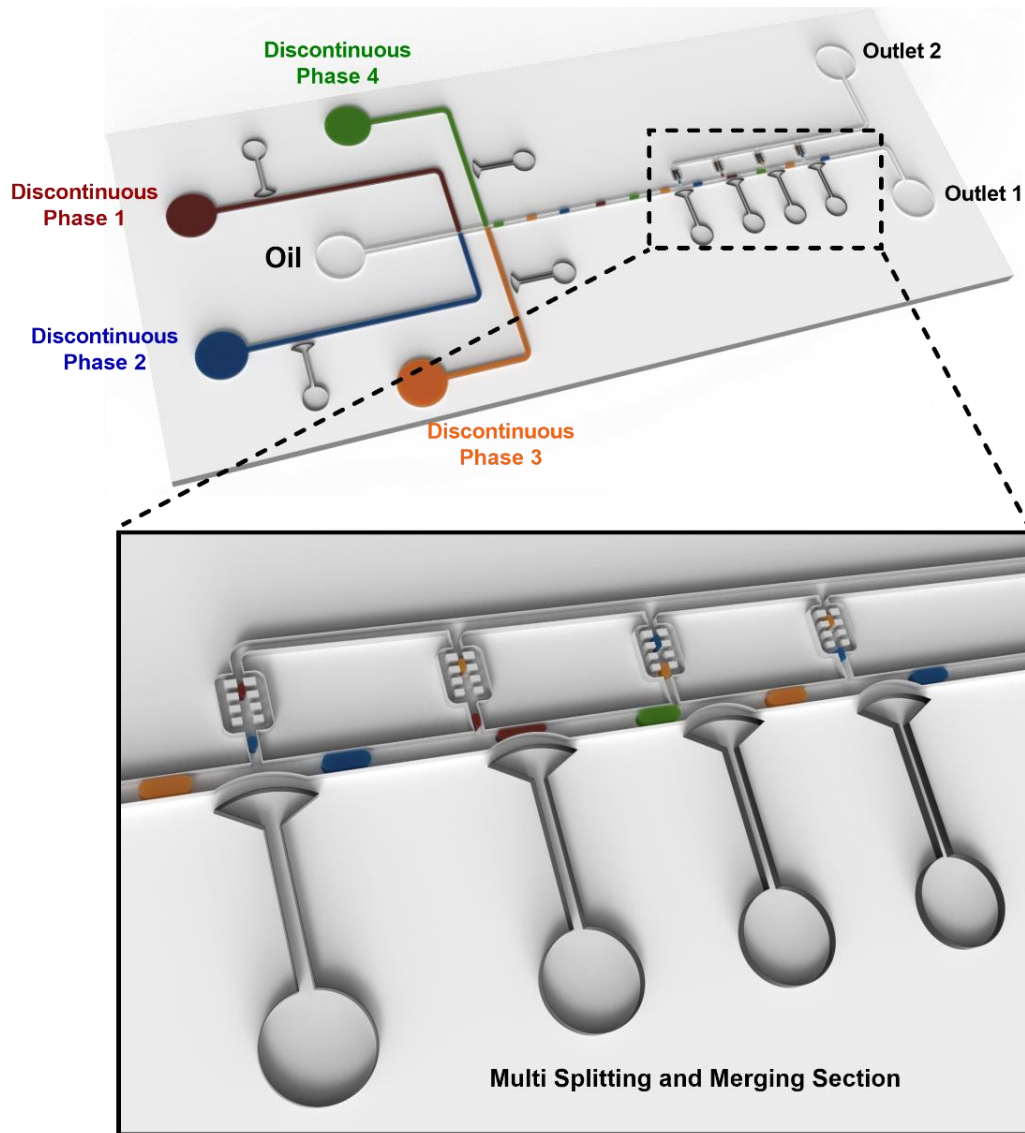


**Figure 4.1:** Schematic of the microfluidic device to achieve selective droplet splitting and merging at multiple locations using eight single-layer microvalves. The microfluidic device generates four different coloured droplets mimicking four different chemicals in the upstream part of the chip, this is achieved using four valves located close to each of the channels carrying discontinuous phases. A zoomed-in view shows that downstream of the generation structures, there is a multiple site splitting and merging section of the chip. Here, the droplet can be split at any of four different locations each controlled by a separate microvalve, after splitting the daughter droplets are merged using a passive pillar-based approach.

## 4.2 Methods and Materials

Polydimethylsiloxane (PDMS) is used to fabricate microchannel using a master mould. We used standard lithography to fabricate the master mould on 4-inch silicon wafer spin-coated with negative photoresist (SU8-3050) for the height of 130 $\mu$ m. PDMS and curing agent mixture (20:1) is poured over prepared mould, degassed, and heated on a hotplate at 70 degrees for 3

hours. After curing, PDMS replica is peeled off from the mould; holes are punched in inlets and outlets of the PDMS replica. PDMS replica and glass slide are bonded by subjecting them to oxygen plasma for 18 seconds.

Polytetrafluoroethylene (PTFE) tubing are used to connect inlets and outlets to the microfluidic flow control system (MFCS<sup>TM</sup>-EZ, Fluigent systems) and syringe pump. We used two different flow control systems simultaneously to control the pressure. One of them is used to control the pressure of air in single-layer pneumatic valves (8 in number), and other is used to control the pressure of the discontinuous phase (4 in number). The syringe pump is used to pump the continuous phase. Synthetic oil (3M<sup>TM</sup> Novec) stabilised by 2% surfactant (30% Pico-surf<sup>TM</sup> + 70% Pico-break<sup>TM</sup>, Sphere Fluidics, UK) is used as the continuous phase in some cases while Olive oil is used to demonstrate droplet splitting and merging. Mili-Q water along with the food-grade dye is used as the discontinuous phase. The videos and images are recorded by a camera (Pixelink PL-B782U, Ottawa, Canada) mounted on an inverted microscope (Olympus CKX53, Tokyo, Japan).

## 4.3 Results and Discussion

### 4.3.1 Channel Flow Rate Examination

We analysed the system to have the same flow rate entering all the four junctions, as finger length of the droplet forming in each junction is dependent on flow rate entering in that junction. To achieve this, we used electric circuit analogy [149], where current is equivalent to flow rate (Q), a potential difference is equivalent to the pressure drop and resistance is equivalent to the hydrodynamic flow resistance of the microchannel. This analysis is used for the initial design of the microfluidic circuit, and design is further modified based on actual experiments performed on the chip. To predict channel flow rate with the least complexity, we only considered the presence of continuous phase and did not consider droplets and pillared merging chambers.

The height of microchannel is assumed to be constant, which is 60  $\mu\text{m}$ . The hydrodynamic resistance in each branch is calculated using the equation below,

$$R = \frac{12\mu l}{wh^3[1-0.63(h/w)]}$$

$$R = al$$

Where  $a = \frac{12\mu}{wh^3 \left[1 - 0.63\left(\frac{h}{w}\right)\right]}$

Where  $w$ ,  $h$ ,  $l$ ,  $\mu$  represent width, height, length of the channel and viscosity of the continuous phase, respectively. Here we need to find the width of branches 5,7,8,10,11 and flow rate  $Q_1$  in terms of  $Q$  (as shown in **Figure 4.2 a**. We will have a similar width for branches 5 and 7, 8 and 10, 11 and 13.

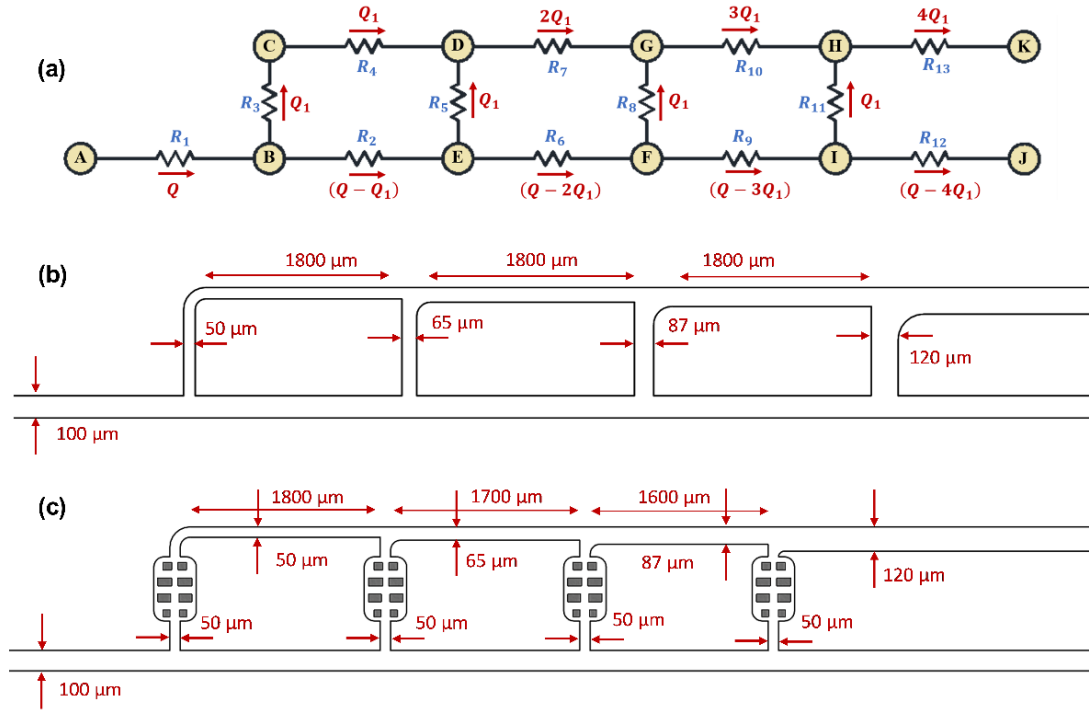


**Figure 4.2:** Working principle of multi-splitting and multi-merging system. (a) The resistance network of a system considering the flow rate and hydrodynamic resistance of each branch without consideration of the presence of droplets in the system. (b) Schematic of the simplified microfluidic system in which same flow rate enters in four T-junctions with different width. (c) Schematic of the actual microfluidic system in the presence of four merging chambers designed in such a way that same flow rate enters in four T-junctions with a similar width.

$$a_5 = a_7, a_8 = a_{10}, a_{11} = a_{13}$$

Applying Kirchhoff's loop law for 1<sup>st</sup> junction, we get

$$R_2(Q - Q_1) + R_5Q_1 - R_4Q_1 - R_3Q_1 = 0$$

$$R_2Q - R_2Q_1 + R_5Q_1 - R_4Q_1 - R_3Q_1 = 0$$

$$R_5Q_1 = (R_2 + R_3 + R_4)Q_1 - R_2Q$$

Converting the above equation in terms of  $a$  and  $l$ , we get

$$a_5l_5Q_1 = (R_2 + R_3 + R_4)Q_1 - R_2Q$$

Dividing both sides by  $Q_1$

$$a_5 l_5 + R_2 Q^* = (R_2 + R_3 + R_4)$$

$$\text{Where } Q^* = \left( \frac{Q}{Q_1} \right)$$

Putting values of the constants, we get

$$5a_5 + (1.77 \times 10^{16} Q^*) = 13.62 \times 10^{16} \quad 4.1$$

Applying Kirchhoff's loop law for 2<sup>nd</sup> junction, we get

$$R_6(Q - 2Q_1) + R_8Q_1 - 2R_7Q_1 - R_5Q_1 = 0$$

$$R_6Q - 2R_6Q_1 + R_8Q_1 - 2R_7Q_1 - R_5Q_1 = 0$$

$$R_8Q_1 = (2R_6 + 2R_7 + R_5)Q_1 - R_6Q$$

Dividing both sides by  $Q_1$ ,

$$R_8 + R_6Q^* = (2R_6 + 2R_7 + R_5)$$

Converting the above equation in terms of  $a$  and  $l$ , we get

$$a_8 l_8 - a_5(2l_7 + l_5) + R_6Q^* = 2R_6$$

Putting values of the constants, we get

$$5a_8 - 37a_5 + (1.77 \times 10^{16} Q^*) = 3.54 \times 10^{16} \quad 4.2$$

Applying Kirchhoff's loop law for 3<sup>rd</sup> junction, we get

$$R_9(Q - 3Q_1) + R_{11}Q_1 - 3R_{10}Q_1 - R_8Q_1 = 0$$

$$R_9Q - 3R_9Q_1 + R_{11}Q_1 - 3R_{10}Q_1 - R_8Q_1 = 0$$

$$R_{11}Q_1 = (3R_9 + 3R_{10} + R_8)Q_1 - R_9Q$$

Dividing both sides by  $Q_1$ ,

$$R_{11} + R_9Q^* = (3R_9 + 3R_{10} + R_8)$$

Converting the above equation in terms of  $a$  and  $l$ , we get

$$a_{11}l_{11} - a_8(3l_{10} + l_8) + R_9Q^* = 3R_9$$

Putting values of the constants, we get

$$5a_{11} - 53a_8 + (1.77 \times 10^{16} Q^*) = 5.31 \times 10^{16} \quad 4.3$$

Both outlets are subjected to atmospheric conditions, we can write

$$(P_A - P_K) = (P_A - P_J)$$

$$\begin{aligned} (P_B - P_C) + (P_C - P_D) + (P_D - P_G) + (P_G - P_H) + (P_H - P_K) \\ = (P_B - P_E) + (P_E - P_F) + (P_F - P_I) + (P_I - P_J) \end{aligned}$$

$$\begin{aligned} R_3Q_1 + R_4Q_1 + 2R_7Q_1 + 3R_{10}Q_1 + 4R_{13}Q_1 \\ = R_2(Q - Q_1) + R_6(Q - 2Q_1) + R_9(Q - 3Q_1) + R_{12}(Q - 4Q_1) \end{aligned}$$

Simplifying the above equation, we get

$$(R_3 + R_4 + 2R_7 + 3R_{10} + 4R_{13})Q_1 = (R_2 + R_6 + R_9 + R_{12})Q - (R_2 + 2R_6 + 3R_9 + 4R_{12})Q_1$$

Dividing both sides by  $Q_1$

$$(R_3 + R_4 + 2R_7 + 3R_{10} + 4R_{13}) = (R_2 + R_6 + R_9 + R_{12})Q^* - (R_2 + 2R_6 + 3R_9 + 4R_{12})$$

Converting the above equation in terms of  $a$  and  $l$ , we get

$$R_3 + R_4 + 2a_5l_7 + 3a_8l_{10} + 4a_{11}l_{13} = (R_2 + R_6 + R_9 + R_{12})Q^* - (R_2 + 2R_6 + 3R_9 + 4R_{12})$$

Putting the value of the constants, we get

$$32a_5 + 48a_8 + 128a_{11} - (8.85 \times 10^{16}Q^*) = (-36.63 \times 10^{16}) \quad 4.4$$

Now we have four equations (1.1, 1.2, 1.3, and 1.4) and four unknown ( $a_5, a_8, a_{11}, Q^*$ ), solving these equations we get,  $w_5 = 65 \mu\text{m}$ ,  $w_8 = 87 \mu\text{m}$ ,  $w_{11} = 125 \mu\text{m}$ ,  $Q_1 = 0.1436 Q$ .

Geometry with these dimensions is shown in **Figure 4.2 b**; this geometry is used as the initial design to conduct the experiments. Several experiments were conducted to modify the initial design further to include the effects of droplets and merging chamber in the microfluidic system. **Figure 4.2 c** shows the modified microfluidic chip design.

### 4.3.2 Droplet Generation

We aim to introduce mother droplets with different composition and later split and merge them. The geometry to achieve this goal consists of the main channel carrying oil (continuous phase) connected to the microfluidic chip using the syringe pump and four other channels carrying dispersed phases interacting perpendicularly to the main channel. We used clear water in one of the inlets of the dispersed phase while for remaining three inlets we used water mixed with food-grade dyes of the colour green, red and blue connected to the chip using Fluigent system. We used two different approaches for droplet generation, first using four single-layer microfluidic valves and second using pressure control of the Fluigent system. These approaches are explained in the sections below in details.

#### 4.3.2.1 Valve Based Approach

We used four single-layer microfluidic valves located close to the channels carrying the discontinuous phase with the membrane thickness of  $35\mu\text{m}$ . Membrane thickness represents the thickness of elastic PDMS separating the dead-end of the valve and the channel. These valves are pressurised when required through Fluigent system to control the generation of

droplets. When these valves are pressurised to 1800 mbar, pressurised air inside the valve deforms the elastic PDMS membrane (35 $\mu$ m) separating valve and inlet of the discontinuous phase. At this pressure, elastic membrane fully deforms and stops the flow of discontinuous phase completely, thereby stopping the generation of the particular kind of droplet—valves used for droplet generation as shown in **Figure 4.3 e**.

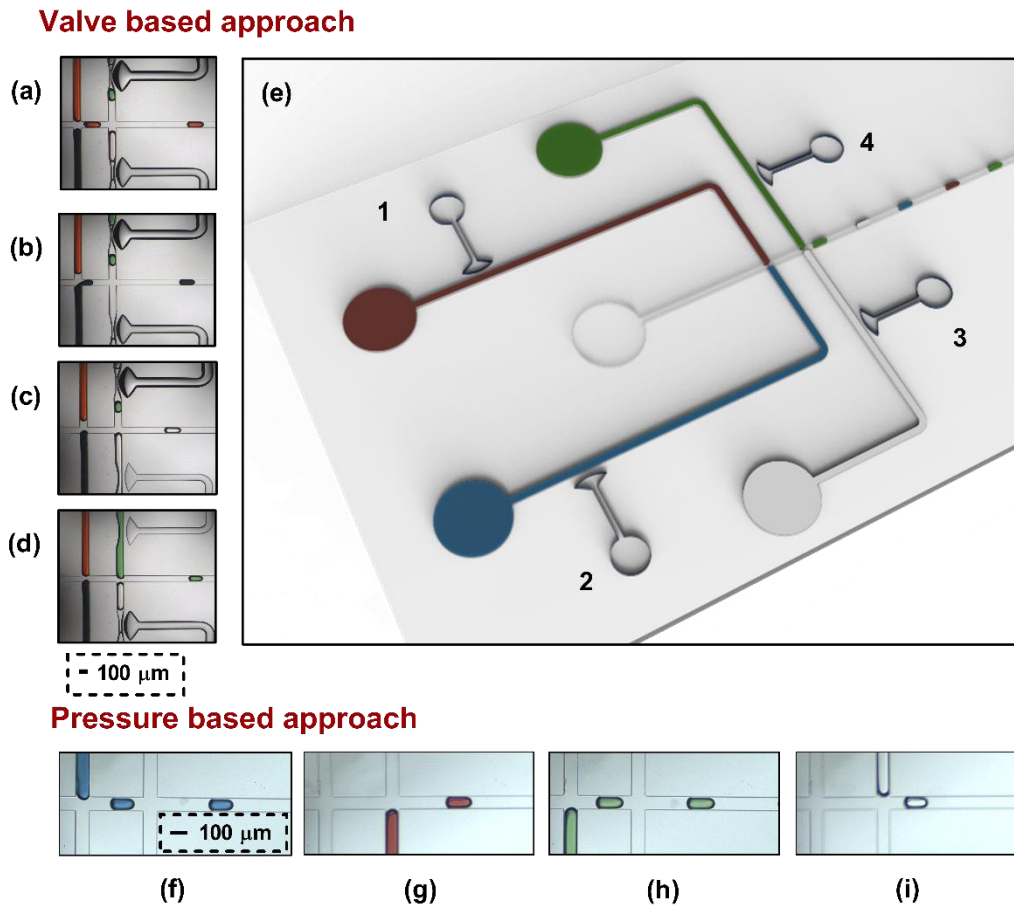


**Figure 4.3:** Droplet generation part of the multi-splitting and multi-merging system using two different approaches. **(a-d)** Valve based droplet generation approach is used to create a red, blue, white, and green droplet, respectively. Scale bars, 100  $\mu$ m. **(e)** Schematic shows all the four valves are used sequentially to generate droplets following the order of the numbers that are written next to them. **(f-i)** Pressure based droplet generation approach which is used to generate blue, red, green, and white droplets, respectively. Scale bars, 100  $\mu$ m.

Initially, all the valves are in depressurised condition and are kept that way till all four streams of discontinuous phase start generating droplets. Now, we fully pressurise three valves to generate only one kind of droplet. To generate only red coloured droplet all the valves except

valve 1 are pressurised to 1800mbar. As other valves are fully pressurised, they do not allow the generation of green, blue and white coloured droplets, as shown in **Figure 4.3 a**. To generate only blue coloured droplets Valves 1, 3, and 4 are actuated (**Figure 4.3 b**). To generate water droplets without any colour, we actuated valves 1, 2 and 4 (**Figure 4.3 c**), and finally, to generate green, valves 1, 2, and 3 are actuated (**Figure 4.3 d**). When three valves are pressurised, and the only single coloured droplet is generated, the system works in a similar way like that of the single T-junction. Various parameters like the size of the droplet, separation distance between the droplet and frequency of the droplet generation can be controlled by the flow rate of the continuous and dispersed phases. To switch from one kind of droplet generation to other, we pressurise all the valves to stop any kind of droplet generation and then depressurise valve to start generating next coloured droplet.

#### **4.3.2.2 Pressure Based Approach**

In this approach, instead of valves, pressure in the discontinuous phase is varied using Fluigent system. For specific droplet generation, pressure in the other three channels carrying the dispersed phase is reduced until they stop producing the droplets. For the generation of red droplets, pressure in other channels carrying the dispersed phase is reduced systematically till the point only red coloured droplet is generated and a similar procedure is followed to generate other droplets as shown in **Figure 4.3 (f-i)**. As we reduce the pressure in other discontinuous phases, fluid in those channels start to retreat and is replaced by the oil. The only problem with this approach is when we want to switch between the different coloured droplets; it takes a considerable amount of time for the next discontinuous phase to start generating the droplet. Compared to the valve-based approach, this approach takes a long time to switch from one kind of droplet to another kind of droplet generation.

#### **4.3.2.3 Generating Droplets Alternately**

With either of the two approaches mentioned in previous subsections, we can generate two or four different droplets one after the other. For the generation of red and green droplets alternately using the valve-based approach, valves controlling the blue and white coloured droplets are pressurised fully to restrict the flow in these channels while valves controlling the red and green coloured droplets are kept in depressurised condition. Fluigent system controlling pressure of the red and green fluid is set at the same value so that they generate red and green

droplets, alternately. For other combinations of droplets like red and green, blue and green (as shown in **Figure 4.4 (a-b)**), the same procedure is followed. For alternately generating droplets using the pressure-based approach, the pressure of the two of the discontinuous phases is kept at the same value while pressure in other two discontinuous phases is systematically reduced until they stop producing the droplets.

We also generated four different coloured droplets one after the other by depressurising all the valves and keeping the pressure of all the discontinuous phases at the same value as shown in **Figure 4.4 c**. We observed that the current geometry of droplet production for four different droplets is unstable. By unstable, we mean the production of four different droplets, one after the other, is not repetitive as four inlets of the discontinuous phase are located close to each other. A slight change in pressure causes the droplet production sequence. To stabilise the droplet production for four different droplets, we modified the geometry. Instead of having all the four channels carrying discontinuous phase connected to the same main channel, we connected two of them to the first oil inlet while other two are connected perpendicularly to the second oil inlet as shown in **Figure 4.4 d**. Then, they are connected at a Y-junction (45°) to generate four different-colour droplets one after the other.

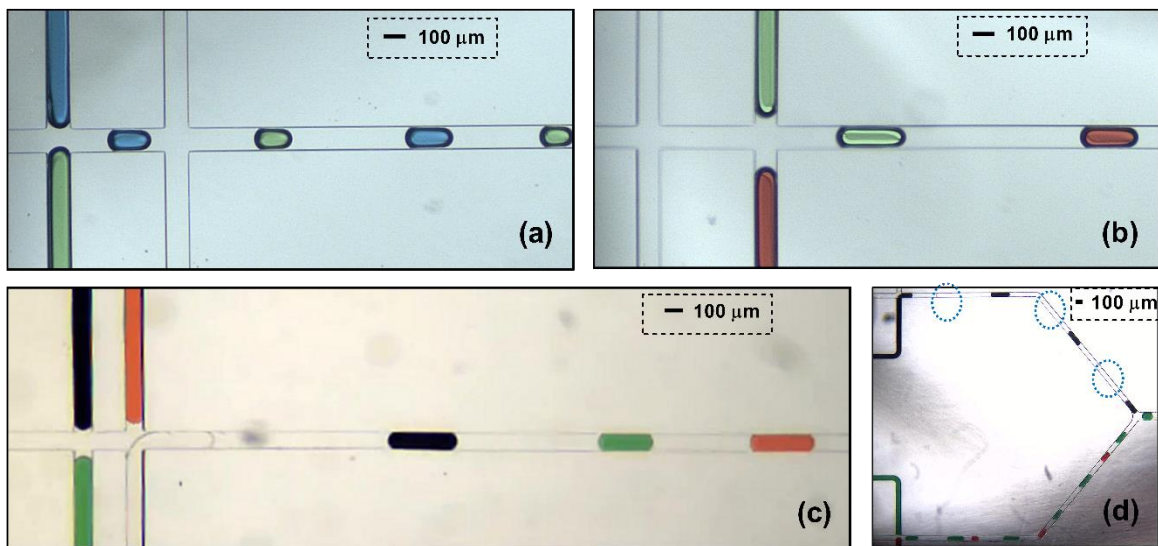


**Figure 4.4:** Generating droplets in different orders using a valve and pressure-based approach. (a) Blue and green droplets are generated, alternately. (b) Green and green droplets are generated, one after the other. (c-d) Four different coloured droplets are produced, sequentially. Scale bar is 100  $\mu\text{m}$ .

### 4.3.3 Droplet Breakup

Droplets will be split at the junctions to the merging chambers by use of four valves along the main channel. In contrast to the use of valves for the droplet generation stage, here they will



not be used in a binary manner. Instead, rather than ceasing flow along the main channel, which would simply divert the droplet in its entirety into the merging chamber, the valve will be partially activated. Enough deformation will be applied to change the division of flow at the junction, pulling more of the droplet into the channel heading to the merging chamber. As a droplet passes a junction in which the flow splits, a finger of the droplet enters the channel with the lower flow. A change in the flow conditions which increases the finger length can cause the finger to pinch off so that the formation of a daughter droplet occurs.

As the valves only act to change local flow conditions, rather than completely block one channel, there is a need to make the change required to transition between behaviours as small as possible. To this end, we first start by analysing the flow conditions when no valve actuation is imposed. The system has been designed such that the flow into the channels at each of the junctions is the same. This provides an idealised starting point for balancing the conditions at each junction, however, the addition of droplets into the system causes alterations to the flow resistances in the system, the inclusion of which into the design process would require no prior knowledge of how the system was to be used and, hence, lose the flexibility of operation being sought.

First, we examine the interaction of the mother droplet with each junction, in the absence of actuation, to obtain a flow regime in which splitting does not occur at any junction. **Figure 4.5** shows different regimes of interaction across a relatively modest range of capillary numbers, 0.006 to 0.009 (calculated from the flow in the main channel before interacting with the first junction). We started with the regime where we observed droplet splitting at all the four junctions, and we called this as regime 1 (**Figure 4.5a**). In this regime the flow rate of the dispersed phase is the highest of all of the regimes, the separation distance between consecutive droplets is the smallest, and the size of the mother droplet is the largest ( $230 \pm 10 \mu\text{m}$ ). As we decreased the flow rate of the dispersed phase gradually, an increase in separation distance and a decrease in the size of the mother droplet ( $210 \pm 10 \mu\text{m}$ ) occurred. Resulting in splitting occurring only in the last three junctions, termed, here, as regime 2 (**Figure 4.5b**). In this regime, the size of the daughter droplet generated becomes larger at each successive junction, there is no droplet splitting at the first junction. With the further reduction of the dispersed phase flow rate (droplet size:  $190 \pm 10 \mu\text{m}$ ), droplet splitting in the last two junctions is observed, regime 3 (**Figure 4.5c**). Finally, with a further decrease in the flow rate of the dispersed phase, no droplet splitting occurred, regime 4 (**Figure 4.5d**). In this regime separation distance is maximum while the size of the mother droplet is minimum ( $175 \pm 10 \mu\text{m}$ ). To have

selective droplet splitting at all the four junctions, regime 4 is the only useful regime as it provides a common outcome of no droplet splitting at all the four junctions.

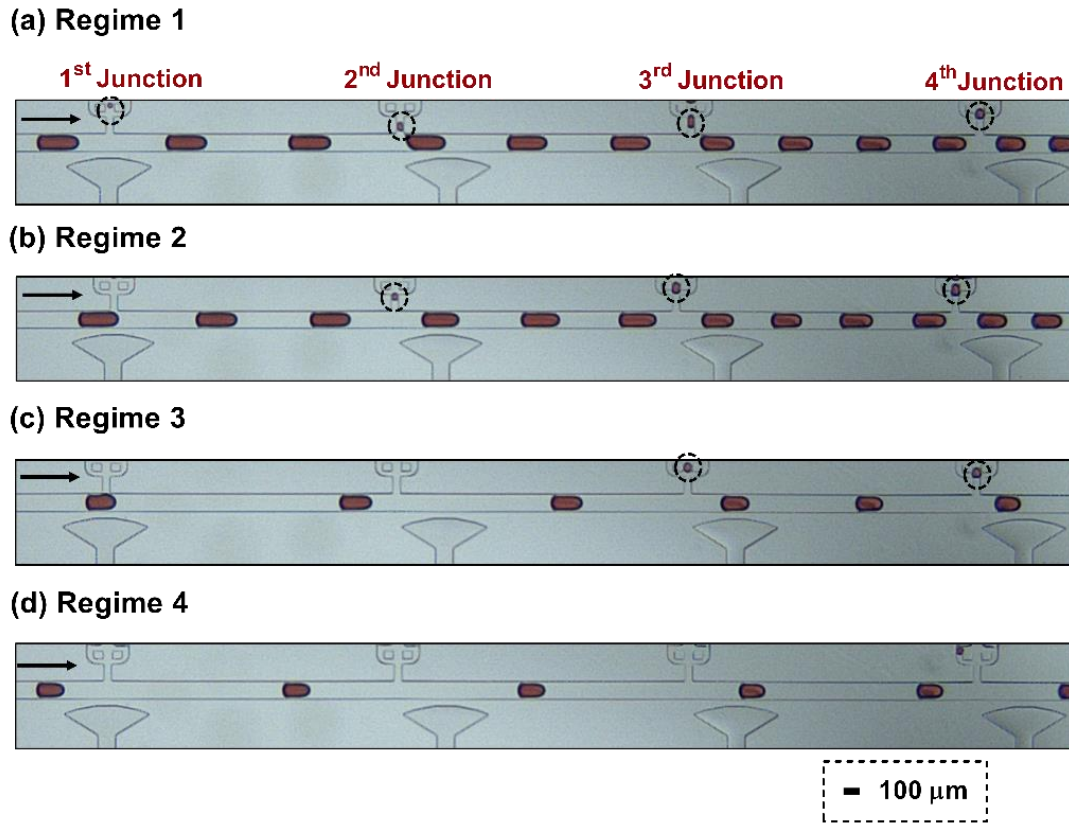


**Figure 4.5:** Different Regimes of droplet splitting when droplets interact with four junctions placed one after the other. (a) Droplets split in all the four junctions. (b) Droplets split in the last three junctions. (c) Droplets split in the last two junctions. (d) There is no droplet splitting in all the four junctions: scale bars, 100  $\mu\text{m}$ .

The percentage of flow rate entering each channel branching from at the junctions is shown in **Figure 4.6**. **Figure 4.6b** shows that there is a critical separation distance at which splitting is observed. The presence of droplets in the channels adds a finite hydrodynamic resistance to the branch in which they are present. Hence, a lower number of droplets in the system will allow the system to function in a manner closer to the idealised design (which ignores this effect). The number of droplets present in a particular branch is inversely proportional to the separation distance. Hence, a decrease in  $d_1$  causes an increase in the resistance of that channel, as such, it is the separation distance in each branch which causes deviations in the flow rate away from the ideal, and so causes four different regimes (rather than two, one with all junctions splitting and one with none).

A line is also plotted (**Figure 4.6c**) distinguishing those cases in which splitting occurred (above 15%) and those in which it did not (below 15%). Ideally, in regime 4, the regime in which selectivity can be imposed, this percentage would be identical in each junction and would lie very close to the 15% value. It can be seen in regime 4, the variation is small, much reduced from the regimes in which different behaviour is observed at each junction.

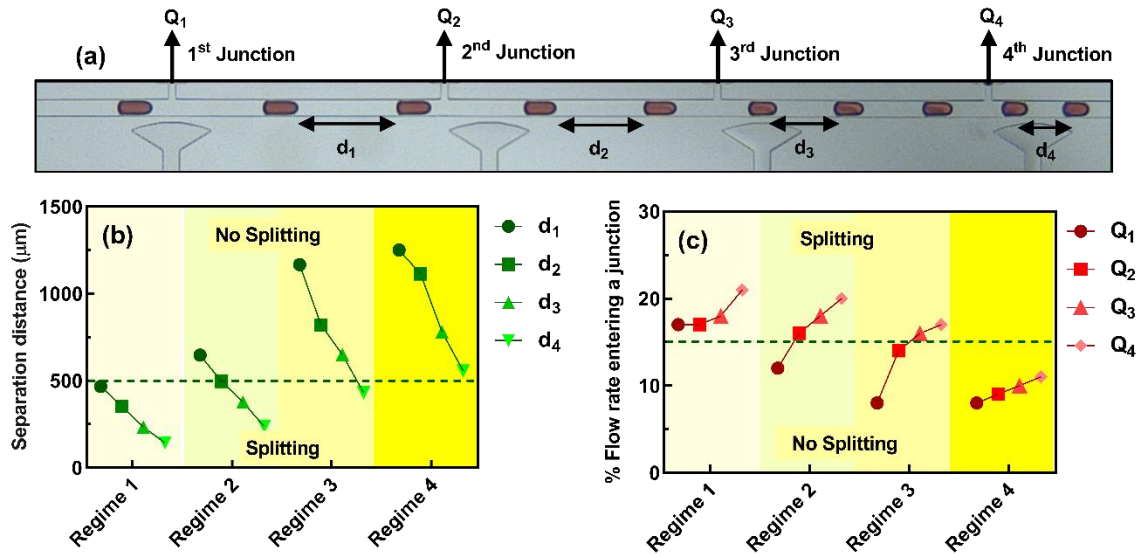


**Figure 4.6:** Classification of different splitting regimes by the separation distance and the percentage of the flow rate entering each junction. (a) Schematic shows the separation distance  $d_1, d_2, d_3, d_4$ . Regimes map is extracted based on (b) the average separation distance in each branch of the main channel, and (c) the percentage of the flow rate entering each branch divided by the total flow rate in the main channel, respectively. The dotted lines separate splitting and no splitting regimes.

#### 4.3.4 Selective Droplet Breakup Using Valves at Four Junctions

Two critical parameters for the present microfluidic system's working are the deformation caused by the valve in elastic PDMS and the time required for pressurising/depressurising the valve. For these two parameters, experiments have been conducted by varying the valve's pressure; these results are shown in **Figure 4.7 a** and **b**.

**Figure 4.7a** shows the plot of maximum deformation in PDMS against the valve pressure. We gradually increased the pressure in a single layer microfluidic valve using a Fluigent system from 0 mbar to 1800 mbar. The deformation because of pressurising the valve is in the form of a semi ellipse. Semi minor axis of this deformation is useful, as it will determine the volume of daughter droplet generated; hence it is plotted on Y-axis. When we gradually increase the valve pressure, deformation increases, maximum deformation for the pressure of 1800 mbar was observed to be 53  $\mu\text{m}$ , which means it blocks more than 50 % of

the main channel due to contraction. In the next set of experiments, we figured out the time required by the valve to achieve maximum deformation (**Figure 4.7 b**). When the valve is pressurised at 1800 mbar, we captured the image sequence of deformation at 266 fps and plotted deformation against time. We observed that the time required to attain maximum deformation is close to 20 ms. In the next set of experiments, we depressurised the valve from 1800 mbar to 0 mbar. We observed that the time required for the channel wall to come back to its original shape is close to 30 ms, making the total time required for pressurising and depressurising the valve to be 50 ms. Hence, the present microfluidic system can split the moving droplets with a frequency of around 20 Hz. **Figure 4.7 c** shows the selectivity of droplet breakup with the help of image sequences. As the first droplet approaches the junction, the valve is depressurised, which does not cause the droplet to break. Before the next droplet arrives at the junction valve is actuated at 1800 mbar, which causes the elastic PDMS membrane to deform, and the droplet breaks at the junction. The valve is depressurised again, and the membrane comes back to the usual position, which allows the droplet to pass the junction without breaking up.

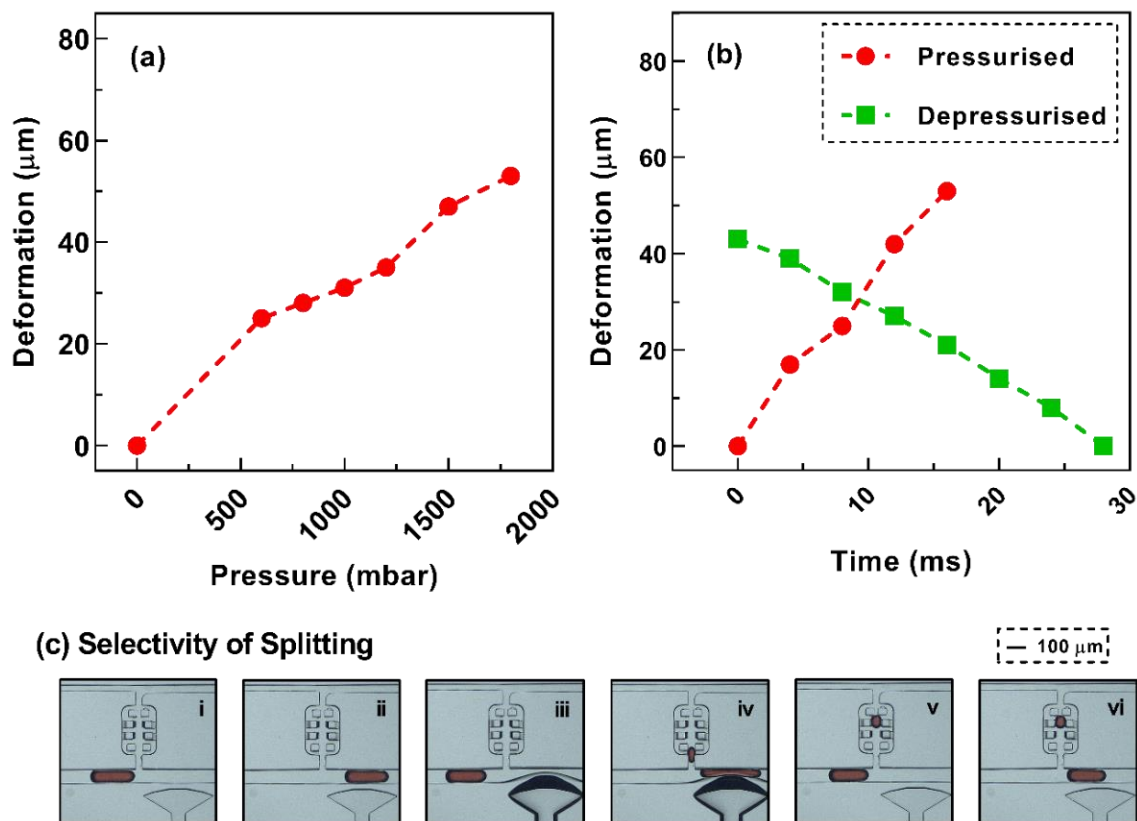


**Figure 4.7:** Characterisation of the single-layer microvalve. (a) Maximum deformation of the channel is plotted against different pressures that are applied to the single-layer valve. (b) Deformation of the channel is plotted against the time when the single-layer valve is fully pressurised to the pressure of

1800 mbar and fully depressurised, respectively. (c) Image sequence showing selectivity of the droplet breakup, red droplet arrives at the second junction and does not break at this junction. Just before the second droplet arrives at this junction valve is actuated to break the droplet. Before the third droplet arrives at this junction valve is deactivated, and the droplet does not split (see appendix D, video D9).

To demonstrate the splitting of different coloured droplets at the different junctions, we operated the microfluidic system in regime 4. There is no droplet splitting at all four junctions in the absence of valve actuation. At each junction, we systematically pressure the valve from 0 to 1800 mbar (corresponding deformation of 53  $\mu\text{m}$ ) to investigate whether a daughter droplet is formed and measure its volume. Daughter droplet formation and size at each junction increases as we pressurise the valve. When we pressurise the valve, deformation in the main channel causes the resistance in the main channel to increase, which leads to droplet splitting at a junction. We observed that the ratio of daughter to mother droplet volume is smallest for the first junction and increases in each subsequent junction for maximum deformation. This variation in droplet volume can be attributed to the fact that in regime 4, the flow rate entering the fourth junction is higher than the other junctions. The maximum relative volume of the daughter droplet formed in the fourth junction is close to 25%, while in the first junction, it is close to 10% for a membrane deformation of 53  $\mu\text{m}$ . The solid line shown in **Figure 4.8a** shows that the deformation required to achieve 10% of the relative volume of daughter droplet is formed in each junction. This system can split a droplet equally at four junctions with the help of a valve placed at each junction pressurised unequally. We also demonstrated selectivity of droplet splitting at each junction by splitting a blue, red, green, and clear droplet at the 1<sup>st</sup>, 2<sup>nd</sup>, 3<sup>rd</sup>, and 4<sup>th</sup> junctions, respectively (**Figure 4.8 b-e**).

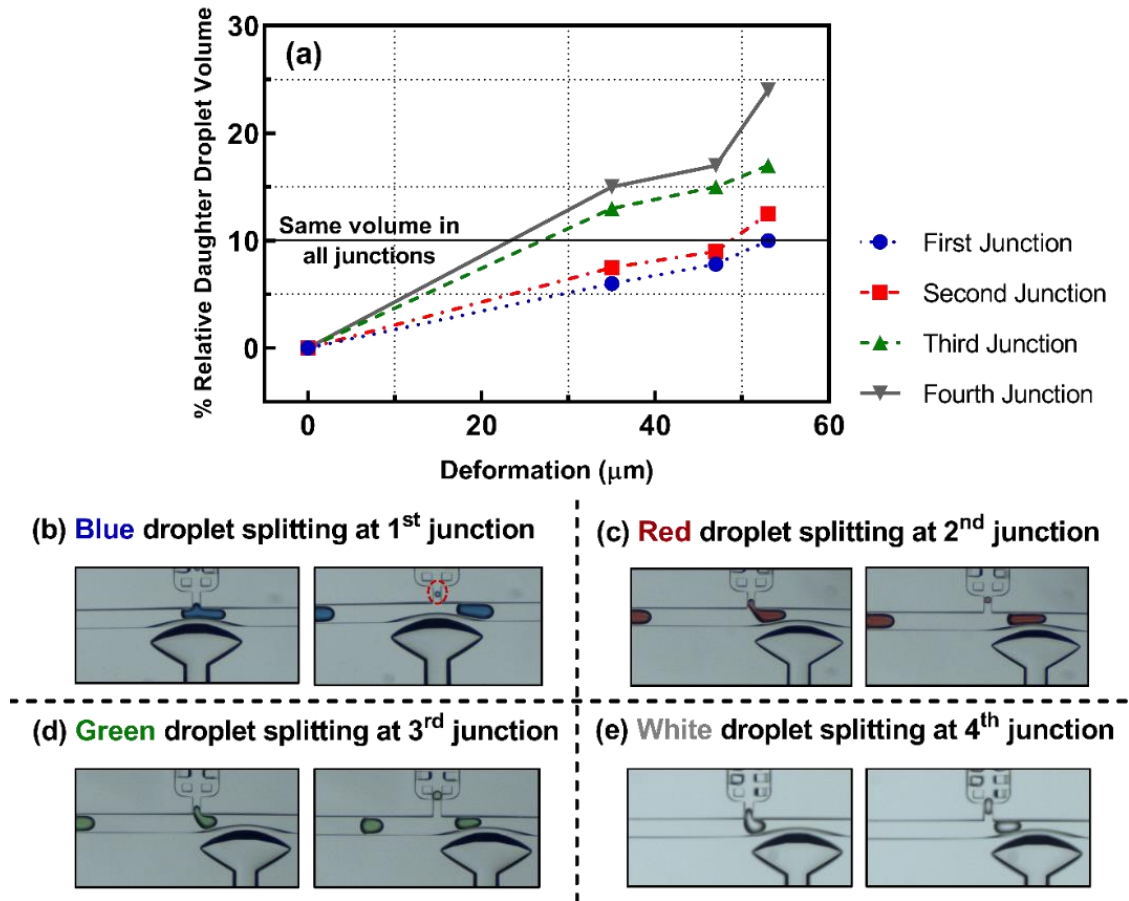


**Figure 4.8:** Splitting of different coloured droplets at different locations using single-layer microfluidic valves. (a) Percentage of the relative daughter droplet volume against the microchannel channel's deformation for all four junctions. (b) The blue coloured droplet is split at the first junction when the valve is pressurised at 1800 mbar (deformation of 53  $\mu\text{m}$ ). (c) Splitting of the red coloured droplet at the second junction using valve pressurised at 1800 mbar. (d) Droplet splitting of the green coloured droplet at third junction using valve pressurised at 1800 mbar. (e) The white coloured droplet is split at the fourth junction when the valve is pressurised at 1800 mbar.

### 4.3.5 Droplet Merging

Four merging chambers with pillars similar to the work of Niu *et al.* [106] were integrated into the system so that the split droplets can be merged as would be required for the onset of a chemical reaction.

First, we demonstrate that the location of splitting can be selected and that merging ensues. Here, droplets of two types are produced alternately and continuously by applying equal pressure to the sources of the two dispersed phases (the valves in the generation section of the chip remaining inactive). As the droplets pass active valves, they all split, the site of splitting is selected by choice of which valve is actuated, but the droplet that should split is not selected. Each daughter droplet enters the merging chamber and merges. When the capacity of

the chamber is reached, they are dragged along the exit channel. Depending on the daughter droplet's size, this can cause the merging of two droplets, **Figure 4.9 a** (1 red + 1 white), as shown at junction three, or four droplets, **Figure 4.9 b** (2 white + 2 blue) shown for junction one. In these experiments, when operated, both valves were pressurised to 1800 mbar. Hence smaller droplets were produced at the first junction than the third.

**Figure 4.9 c** three droplets are merged, two clear and one red; hence the concentration of the merged droplet is altered from the 1:1 ratio shown previously. Again, the droplets that are split are not chosen selectively, rather the location at which they are split. In this case, the valve is pressurised until it splits three droplets and then depressurised, the droplets being generated passively as an alternating stream. As the daughter droplet volume depends on the pressure applied to the valve, two droplets of different sizes can also be merged to control concentration. However, this requires the pressure applied to the single valve to be rapidly altered.

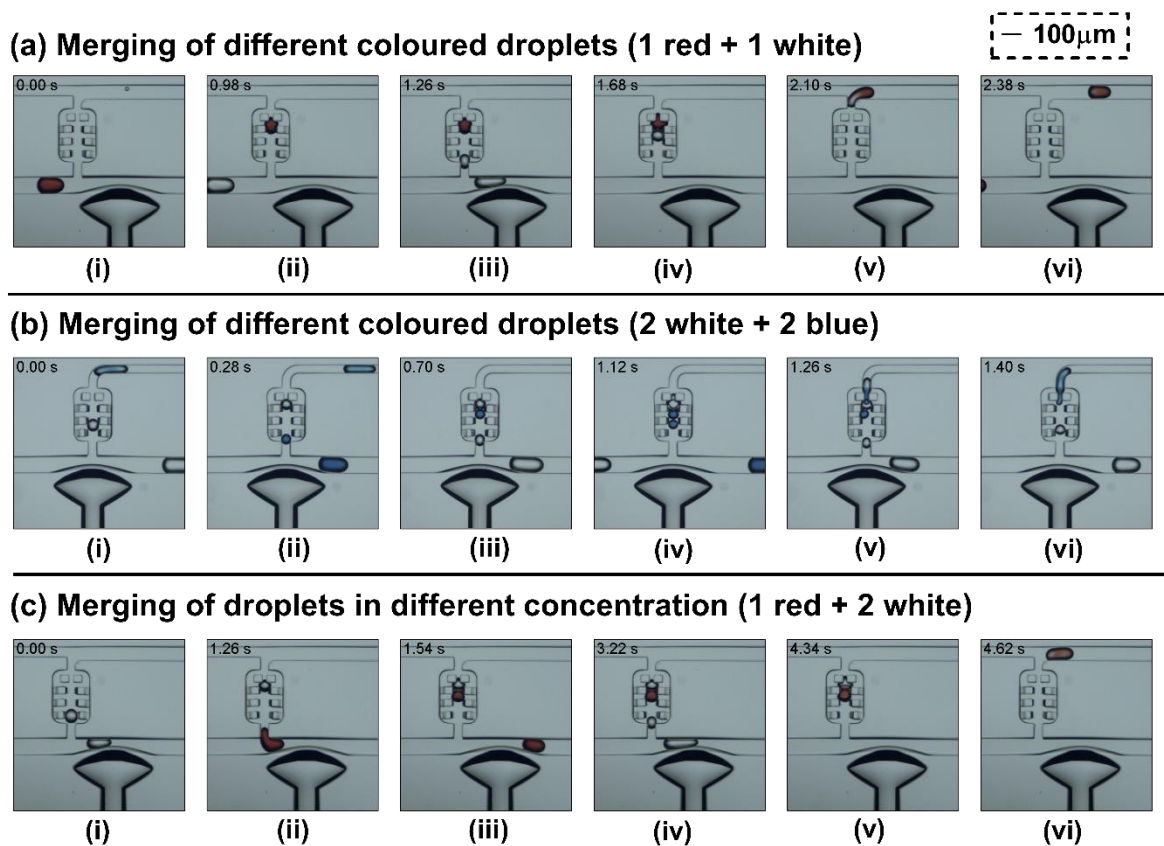


**Figure 4.9:** Splitting of different coloured droplets occurs whilst the valve is actuated. The two daughter droplets are merged within the chamber, the first being retarded by the pillar structures; after merging, the total volume is such that the droplet is dragged out of the merging chamber. Merging of two different coloured droplets, an equal volumetric ratio is shown at the **(a)** third (see appendix D, video D1, D2, D7 and D8) and **(b)** first junctions (see appendix D, video D3 and D4). In the former, a single red



daughter droplet is merged with a single clear one. For the latter, two blue daughter droplets are merged with two clear droplets. (c) Merging of an unequal number of droplets generated from two different samples is achieved, such that the mixing ratio is 1:2 (red: clear) (see appendix D, video D5 and D6).

Finally, we demonstrate the selective splitting of droplets. Here, the location of splitting is dictated by the choice of the valve being operated. The transient nature of valve actuation selects the droplet. In **Figure 4.10**, a single clear droplet is selected out of a stream and split, with the daughter droplet remaining trapped in the merging chamber. Subsequently, a single red droplet out of a stream is split, such that when its daughter droplet enters the merging chamber, it merges with the clear daughter droplet.

This demonstrates single-layer valves' ability to control the introduction of relatively large sample volumes onto the chip and then split these droplets and deposit nanolitre volumes into a merging chamber. For the splitting process, selectivity is achieved both spatially, as local geometric deformation is used such that splitting occurs at just one valve, and temporally such that splitting of a single selected droplet is obtained. Taken together, this approach can be used to subdivide droplets generated on a chip as performed here or introduced after off-chip production and mix them in different combinations at multiple sites.

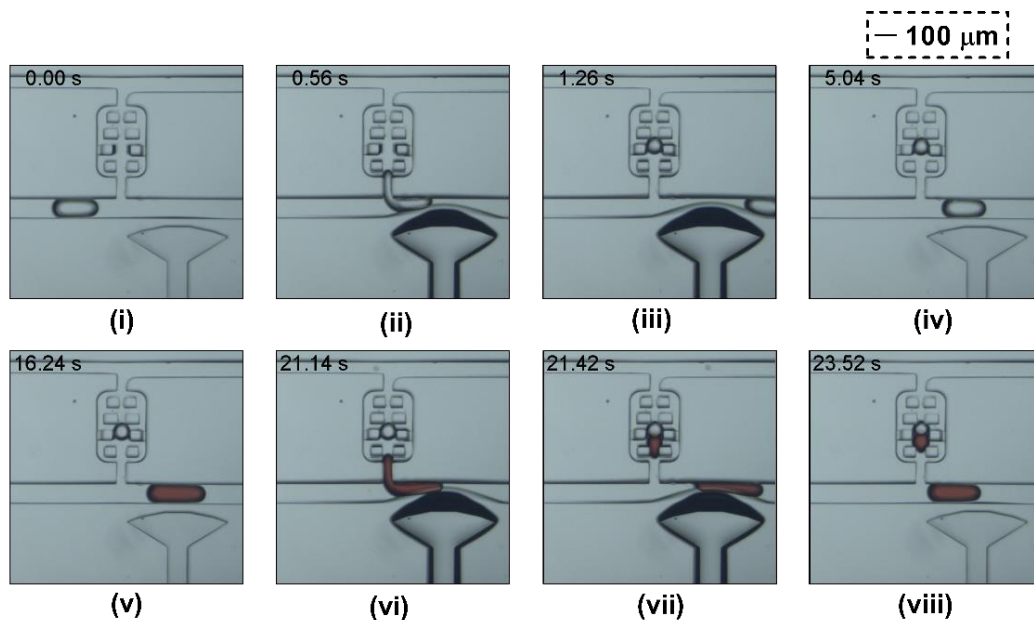


**Figure 4.10:** Image sequence demonstrating the merging of two different selected droplets (one clear and one red droplet) at the third junction. The clear droplet is split by the transient actuation of the valve, resulting in a daughter droplet deposition in the merging chamber. Subsequent clear droplet passes without splitting due to timely deactivation of the valve. Finally, a single red droplet is selected and split; again, a daughter droplet is formed and merges with the clear daughter droplet (see appendix D, video D10).



## 4.4 Closure

We present multi splitting and multi merging microfluidic systems capable of generating different kinds of droplets, split them selectively in different volumes at four junctions, and merging the same droplets/different droplets using pillar induced merging. Droplets are first generated upstream using four standard T-junctions. We have shown that with valve and pressure-based approach, we can generate different coloured droplets separately and one after the other. These generated droplets are then split selectively at four junctions using microfluidic valves in different volumes as well. Finally, we have shown the ability to merge two similar droplets and two different kinds of droplets in various concentrations. The presented microfluidic platform provides control over the valve pressure at each junction, giving users complete ability over the volume of droplet and kind of droplet to split at whichever junction they want and merge later. Microfluidic single layer valves are biocompatible and can be operated at high-speed. It unveils an easy technique to use for splitting and merging at multiple locations. This way, it can reduce chemical waste and save analysis time in sample reagent studies, making it ideal for closed channel microfluidic high throughput screening.



# Chapter 5

## 5 Conclusion and Future Scope of Work

### 5.1 Conclusions

In the second chapter, we investigated the effect of the bypass channel's width ( $\beta$ ) and Capillary number ( $Ca$ ) on no droplet breakup to droplet breakup regimes. Microchannels were fabricated using standard photolithography techniques, and interfacial dynamics is visualised using a high-speed camera. Silicone oil/paraffin oil and water are used as a continuous phase and a discontinuous phase. Experiments show a critical value of  $\beta$ ; keeping  $Ca$  at a constant value for achieving the droplet breakup. Similarly, there is a critical value of the  $Ca$  exists, keeping  $\beta$  constant. We proposed a regime map on the  $Ca$ - $\beta$  plane for showing regimes of no breakup and breakup. We plotted the contours of finger length ( $L_f$ ) in the regime map and the percentage of daughter droplet volume to mother droplet volume ( $V_{ratio}$ ). We observed that the maximum volume of the daughter droplet corresponds to the minimum  $Ca$  and maximum  $\beta$ . Three-dimensional numerical simulations were carried out using commercial CFD software for the breakup and no-breakup cases and validated with the experiments. The simulated results for interfacial dynamics,  $L_f$  and  $V_{ratio}$ , were in good agreement with the experimental results. Simulations proved that when the hydrodynamic pressure drops across the droplet and average shear stress acting on the finger overcomes differential Laplace pressure of the droplet, droplet breakup occurs otherwise not. Like the squeezing and dripping regimes of droplet generation, we reported regimes for droplet breakup at the bypass channel entrance, and they exhibit equivalent squeezing and dripping regimes. In the squeezing regime, the hydrodynamic pressure drop across the droplet plays a crucial role. In the equivalent dripping regime, both shear stress and hydrodynamic pressure drop were dominant. This work provides valuable information regarding the knife-edge between droplet breakup and no breakup, thus significantly beneficial for active methods like surface acoustic waves, electric, magnetic, pneumatic, and thermal control.

In the third chapter, we analysed the droplet behaviours in a microfluidic system having two junctions, seeking to find the underlying conditions for selective droplet breakup at two locations. In the first set of experiments, we used two identical T-junctions placed one after the

other. However, this geometry did not provide identical conditions at both the junctions; hence we discarded this geometry. We used a resistive network analysis to re-design the microfluidic system. The microfluidic system was designed so that the continuous phase's flow rate entering the first and second junction is similar. This was achieved using a T-junction and an expansion channel placed one after the other. We observed that, when droplet interacted with these two junctions, there are five regimes observed, namely 1) No droplet breakup at two junctions. 2) Droplet breakup only at the first junction, 3) Droplet breakup at both the junctions with higher daughter droplet volume in first junction, 4) Droplet breakup at both the junctions with daughter droplet volume higher at second junction 5) Intermittent/irregular droplet breakup in both the junctions. In the first regime, the droplet interaction with both junctions is similar; that is, there is no droplet breakup at both the junctions. The first regime allowed a critical operational condition to be selected, at which break-up do not entirely occur. We then showed the design requirements for the location of microvalves, simulated by deformations of the channel wall, such that we can alter the break-up condition at just one of the junctions. Finally, we used experimental work to show the splitting of droplets at two locations using pressurised valves.

In the fourth chapter, we present multi splitting and multi merging microfluidic systems capable of generating different kinds of droplets, splitting them selectively in different volumes, and merging the same droplets/different droplets using pillar induced merging. Droplets are first generated upstream using four standard T-junctions. We have shown that with valve and pressure-based approach, we can generate different coloured droplets separately and one after the other. These generated droplets are then split selectively at four junctions using microfluidic valves in different volumes as well. The microfluidic system was designed using resistive network analysis so that the same flow enters at each junction. We plotted the volume of daughter droplet formed at four junctions against the valve's deformation. Finally, we have shown the ability to merge two similar droplets and two different kinds of droplets in various concentrations. The presented microfluidic platform provides control over the valve pressure at each junction, giving users complete ability over the volume of droplet and kind of droplet to split at whichever junction they want and merge later. Microfluidic single layer valves are biocompatible and can be operated at high-speed. It unveils an easy technique to use for splitting and merging at multiple locations. This way, it can reduce chemical waste and save analysis time in sample reagent studies, making it ideal for closed channel microfluidic high throughput screening.

## 5.2 Future Scope of Work

In the present thesis, we have used de-ionised water as a discontinuous fluid for generating droplets, and de-ionised water is a Newtonian fluid. For the applications in chemical and biological research areas, fluids used are sometimes non-Newtonian and complex. The present work can be extended for non-Newtonian fluids like the shear-thinning solution of xanthan gum using different concentration. The viscosity of such fluids is proportional to the shear rate that they are subjected. The generation and interaction of droplets made up of non-Newtonian fluids with the bypass channel entrance can be investigated to determine the breakup regimes and non-breakup against the flow conditions applied. Knife-edge conditions separating the regime of droplet breakup and non-breakup of the shear-thinning solution will be significantly different for different flow conditions when compared to the Newtonian fluids. The knowledge acquired from the above investigation can be coupled with any active methods to demonstrate droplet manipulation of non-Newtonian fluids.

In multi-splitting and the merging presented in chapter 4, single-layer microvalves are operated manually. Manual operation is slow compared to the automatic operation of valves. The incorporation of capacitive sensing of droplets in the multi-splitting and merging chamber will add further accuracy to the setup. Different droplets can be sensed by capacitive sensing. Single-layer microvalves controlling the generation and splitting of the valve could be operated based on droplet manipulation required for the process.

# Appendix A

## Numerical Equations used for simulations

Ansys Fluent solves Navier Stokes equations using a finite volume method to simulate the droplet behaviour. For tracking and locating fluid-fluid interface between continuous and discontinuous phase volume of fluid (VOF) method is used, the Navier-stokes equation and VOF are solved separately. Navier Stokes equations are given as follows:

Continuity equation

$$\frac{\partial \rho}{\partial t} + \nabla \cdot (\rho V) = 0$$

Momentum equations

X-momentum

$$\frac{\partial(\rho u)}{\partial t} + \nabla \cdot (\rho u V) = -\frac{\partial p}{\partial x} + \frac{\partial \tau_{xx}}{\partial x} + \frac{\partial \tau_{yx}}{\partial y} + \frac{\partial \tau_{zx}}{\partial z} + \rho f_x$$

Y-momentum

$$\frac{\partial(\rho v)}{\partial t} + \nabla \cdot (\rho v V) = -\frac{\partial p}{\partial y} + \frac{\partial \tau_{xy}}{\partial x} + \frac{\partial \tau_{yy}}{\partial y} + \frac{\partial \tau_{zy}}{\partial z} + \rho f_y$$

Z-momentum

$$\frac{\partial(\rho w)}{\partial t} + \nabla \cdot (\rho w V) = -\frac{\partial p}{\partial z} + \frac{\partial \tau_{xz}}{\partial x} + \frac{\partial \tau_{yz}}{\partial y} + \frac{\partial \tau_{zz}}{\partial z} + \rho f_z$$

The volume of fluid (VOF) method was used for the first time by Hirt & Nichols in 1981 [157]. VOF can model two or more immiscible fluids by solving momentum equations and finding out the volume fraction of a particular phase in each control volume. Hirt & Nichols defined a function  $F$ , whose value is unity when a cell is full of fluid and zero when it is empty cells with  $F$  values between zero, and one must then contain an interface.

$F = 0$  (The cell is empty).

$F = 1$  (The cell is full of fluid).

$0 < F < 1$  = the cell contains the interface.

$F$  is governed by the equation as follows

$$\frac{\partial F}{\partial t} + u \frac{\partial F}{\partial x} + v \frac{\partial F}{\partial y} = 0$$

## Appendix B

### Details about the validation of numerical simulations in chapter 2

We have validated numerical simulation with experimental work for the case of droplet breakup in a bypass channel and no droplet breakup in a bypass channel. The details about the length of mother droplet in  $\mu\text{m}$ , the percentage volume of daughter droplet formed, finger length in  $\mu\text{m}$  and Capillary number used is provided in the table below. To save the computational time in 3D numerical simulation, we have considered only one droplet in numerical simulation, contrary to the number of droplets in actual experiments. As each droplet represents a hydrodynamic resistance in the system, there is some difference in numerical simulations and experiments regarding finger length and percentage of daughter droplet volume formed.

	Experimental	Numerical
<b>Case of droplet breakup in the bypass channel</b>		
1. Length of mother droplet ( $\mu\text{m}$ ) (input)	328	328
2. The percentage volume of daughter droplet formed	11.4%	7.2%
3. Finger length ( $\mu\text{m}$ )	90	78
4. Capillary number (input)	0.007	0.007
<b>Case of no droplet breakup in the bypass channel</b>		
1. Length of mother droplet ( $\mu\text{m}$ ) (input)	358	358
2. The percentage volume of daughter droplet formed	No breakup	No breakup
3. Finger length ( $\mu\text{m}$ )	62	53
4. Capillary number (input)	0.005	0.005

### Velocity vectors inside droplet during droplet breakup in chapter 2

The velocity field inside a droplet using simulations is similar to that observed by Wang et al.<sup>1</sup>. The velocity field is substantial inside the droplet compared to the outside. The magnitude of velocity close to the droplet boundary is more than that of the droplet's centre part. The higher velocity close to the boundary causes the droplet to move forward. We observed that the bypass channel's droplet interaction outcome depends mainly on the droplet portion entering the bypass channel. In case of droplet breakup, as some portion of droplet

enters the bypass channel, velocity inside the droplet close to the later part of the droplet drags it towards the bypass channel, causing the droplet to break, as shown in **figure 1 (v)**.

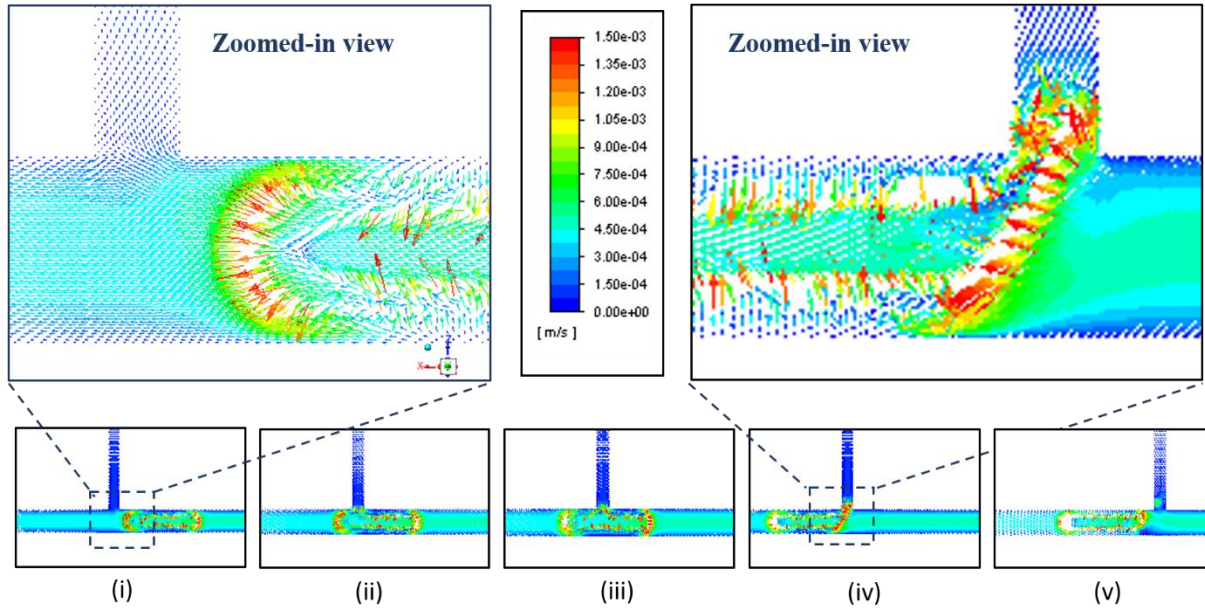


**Figure 11: (i-v)** Sequence of images showing velocity vector inside the droplet and close to the bypass channel entrance. Zoomed-in view of image i and iv are also presented.

## Videos of Droplet Breakup at the Entrance of the Bypass channel in Microfluidic System

### Google Drive Link

<https://drive.google.com/drive/folders/1bUheKY6HU9Y8vE0tYNuo02mtot0kA3X?usp=sharing>

**Video B1 :** High-speed visualization of the droplet interaction with the bypass channel entrance at  $Ca = 0.0028 \pm 0.0002$  and  $\beta = 0.48$  (**AVI**).

**Video B2:** High-speed visualization of the droplet interaction with the bypass channel entrance at  $Ca = 0.0028 \pm 0.0002$  and  $\beta = 0.77$  (**AVI**).

**Video B3 :** High-speed visualization of the droplet interaction with the bypass channel entrance at  $Ca = 0.0028 \pm 0.0002$  and  $\beta = 0.77$  (**AVI**).

**Video B4:** High-speed visualization of the droplet interaction with the bypass channel entrance at  $\beta = 0.48$  and  $Ca = 0.0022$  (**AVI**).



**Video B5:** High-speed visualization of the droplet interaction with the bypass channel entrance at  $\beta = 0.48$  and  $Ca = 0.005$  (**AVI**).

**Video B6:** High-speed visualization of the droplet interaction with the bypass channel entrance at  $\beta = 0.48$  and  $Ca = 0.037$  (**AVI**).

**Video B7:** Computer animation of droplet interaction with the bypass channel entrance at  $\beta = 0.48$  and  $Ca = 0.005$  (**AVI**).

**Video B8:** Computer animation of droplet interaction with the bypass channel entrance at  $\beta = 0.63$  and  $Ca = 0.007$  (**AVI**).

## Appendix C

### Details about the validation of numerical simulations in chapter 3

We validated the numerical simulation with experimental work at both the junctions in the first regime, where there is no droplet breakup at both the junctions. We specifically chose this regime as this is the only regime that provides the same output of no droplet breakup at both the junctions, and valves can be used at both the junction to go from no droplet breakup to droplet breakup. We used the same length of mother droplet, flow conditions, and separation distance for numerical simulations compared to experimental work. We observe that, in addition to the output of no droplet breakup in numerical simulations, finger length in numerical simulation matches the experimental work closely, as shown in the table below.

	Experimental	Numerical
1. Length of mother droplet ( $\mu\text{m}$ ) (input)	150	150
2. Separation distance $d_1$ ( $\mu\text{m}$ ) (input)	994	994
3. Separation distance $d_2$ ( $\mu\text{m}$ ) (input)	750	750
4. Capillary number (input)	0.011	0.011
5. Finger length at the first junction ( $\mu\text{m}$ )	27	33

### Videos of Microfluidic Valves for Selective on Chip Droplet breakup at Multiple Sites

#### Google Drive Link

<https://drive.google.com/drive/folders/15-8A-Xz5O8msJ69numxMcbVlufPxCPPW?usp=sharing>

**Video C1:** Regimes of droplet interaction with first and second junction. These regimes are 1) No droplet breakup in both junctions. 2) Droplet breakup in first junction. 3) Droplet breakup in first junction onset of breakup in second junction. 4) Droplet breakup in both junctions (AVI).

**Video C2:** Numerical simulations with the use of deformation (or valve) at a first and second junction to achieve selective droplet breakup at these junctions (**AVI**).

## Appendix D

### Videos of Controlled Droplet Manipulation and Interaction using Single-Layer Microvalves

#### Google Drive Link

[https://drive.google.com/drive/folders/1uwaCk5fa\\_ww1ek1MOSB3z1GpqVdROCLb?usp=sharing](https://drive.google.com/drive/folders/1uwaCk5fa_ww1ek1MOSB3z1GpqVdROCLb?usp=sharing)

**Video D1:** Merging of one pair of different coloured droplets in the same concentration (1 red and 1 clear droplet merge.) Here, red coloured and clear droplets are generated one after the other in the droplet generation section. We then pressurise the valve close to a third junction where we want to merge to 1800 mbar. When a red coloured droplet passes the junction with a pressurised valve, there is droplet splitting, and the daughter droplet is trapped in the merging chamber. Following that, a clear droplet approaches the junction and splits to generate clear daughter droplet, which gets trapped in the merging chamber. Thin-film between two trapped daughter droplets prevent the merging of two droplets. In a short time, this thin film drains out, and two daughter droplets merge and later, the newly formed droplet is ejected out of the chamber. The movie is in real-time with 7 fps.

**Video D2:** Merging of one pair of different coloured droplets in same concentration (1 red and 1 clear droplets merge.) – Frame rate was decreased by the factor of 7. The attached movie was extracted from the Supplementary Movie 1, the frame rate was decreased by the factor of 7 (from 7 fps to 1 fps) to improve the clarity of the droplets splitting and merging. Timer was added to the movie during the valve operation.

**Video D3:** Merging of two pairs of different coloured droplets in the same concentration (2 blue and 2 clear droplets merge.) Here, clear and blue coloured droplets are generated in the droplet generation section one after the other. We then pressurise the valve close to a first junction where we want to merge to 1800 mbar. With a pressurised valve, when clear coloured droplet passes the junction with a pressurised valve, there is droplet splitting, and the daughter droplet is trapped in the merging chamber. Following that, blue coloured droplet approaches the junction and splits to generate blue daughter droplet, which gets trapped in the merging

chamber. The second set of daughter droplets with clear and blue colour again splits and gets trapped in the merging chamber before merging and ejecting. The movie is in real-time with 7 fps.

**Video D4:** Merging of two pairs of different coloured droplets in same concentration (2 blue and 2 clear droplets merge.) – Frame rate was decreased by the factor of 7. The attached movie was extracted from the Supplementary Movie 3, the frame rate was decreased by the factor of 7 (from 7 fps to 1 fps) to improve the clarity of the droplets splitting and merging. Timer was added to the movie during the valve operation.

**Video D5:** Merging of different coloured droplets in different concentration (1 red and 2 clear droplets merge.) Here, we demonstrate this by splitting and merging two clear droplets with one red coloured droplet at the third junction. Red and clear droplets are generated alternately in the droplet generation section. Then, the clear droplet is split and trapped in the merging chamber. Red droplet following the clear droplet is split and trapped in the merging chamber. We keep the valve pressurised, to split third droplet and trap it in merging chamber: a red droplet and two clear droplets which are trapped in a chamber, merge in a short time and are ejected out. The movie is in real time with 7 fps.

**Video D6:** Merging of different coloured droplets in different concentration (1 red and 2 clear droplets merge.) – Frame rate was decreased by the factor of 7. The attached movie was extracted from the Supplementary Movie 5, the frame rate was decreased by the factor of 7 (from 7 fps to 1 fps) to improve the clarity of the droplets splitting and merging. Timer was added to the movie during the valve operation.

**Video D7:** Merging of one pair of similar coloured droplets in same concentration (2 clear droplets merge.) In this study to merge two same coloured droplets, we generate only one coloured droplet. These generated droplets (in this case, clear) start travelling towards the junction where we want to merge them. We pressurise the valve close to that particular junction (here second junction) to 1800 mbar, causing the droplet to split and daughter droplet gets trapped in the pillars of merging chamber. Merging chamber is designed to hold a specific volume of daughter droplet. When the next mother droplet arrives at the junction due to the pressurised valve, it splits at the same junction and the second daughter droplet is generated. In a short time, two daughter droplets of similar colour merge and later the newly formed droplet is ejected out of the chamber. The movie is in real time with 7 fps.

**Video D8:** Merging of one pair of similar coloured droplets in same concentration (2 clear droplets merge.) – Frame rate was decreased by the factor of 7. The attached movie was extracted from the Supplementary Movie 7, the frame rate was decreased by the factor of 7 (from 7 fps to 1 fps) to improve the clarity of the droplets splitting and merging. Timer was added to the movie during the valve operation.

**Video D9:** Selective droplet splitting using single layer microfluidic valve. The attached movie shows the selectivity of the droplet splitting, red droplet arrives at the second junction and do not split at this junction, just before the second droplet arrives at this junction valve is actuated with the pressure of 1800 mbar to split the droplet. Before the third droplet arrives at this junction valve is deactivated, and the third droplet does not split. Timer was added to the movie during the valve operation and the video is in real time with 7 fps.

**Video D10:** Selective droplet merging using single layer microfluidic valve. The attached movie shows merging of two different coloured droplets selectively (clear and red droplet here) at the third junction. The clear droplet is split using actuation of the valve with the pressure of 1800 mbar; daughter droplet generated is trapped in a merging chamber. We deactivate the valve and allow a few clear droplets to pass without splitting. We then allow red droplets to pass the junction without splitting. Just before the targeted red droplet arriving at the junction, we pressurise the valve to break red droplet selectively, and later red droplet merges with the trapped clear droplet. Timer was added to the movie during the valve operation and the video is in real time with 7 fps.

## References

- [1] G. M. Whitesides, "The origins and the future of microfluidics," *Nature*, vol. 442, no. 7101, pp. 368–373, 2006, doi: 10.1038/nature05058.
- [2] A. Manz, N. Graber and H.M.Widmer, "Miniaturized Total Chemical Analysis Systems: a Novel Concept for Chemical Sensing," *Sensors Actuators, BI*, pp. 244–248, 1990, doi: 10.1109/34.387509.
- [3] H. A. Stone, A. D. Stroock, and A. Ajdari, "ENGINEERING FLOWS IN SMALL DEVICES Microfluidics Toward a Lab-on-a-Chip," *Annu. Rev. Fluid Mech.*, vol. 36, no. 1, pp. 381–411, 2004, doi: doi:10.1146/annurev.fluid.36.050802.122124.
- [4] T. M. Squires and S. R. Quake, "Microfluidics Fluid physics at the nanoliter.pdf," pp. 1–50, 2005.
- [5] I. Kobayashi, K. Uemura, and M. Nakajima, "Formulation of monodisperse emulsions using submicron-channel arrays," *Colloids Surfaces A Physicochem. Eng. Asp.*, vol. 296, no. 1–3, pp. 285–289, 2007, doi: 10.1016/j.colsurfa.2006.09.015.
- [6] J. U. Shim *et al.*, "Ultrarapid generation of femtoliter microfluidic droplets for single-molecule-counting immunoassays," *ACS Nano*, vol. 7, no. 7, pp. 5955–5964, 2013, doi: 10.1021/nn401661d.
- [7] P. S. Dittrich, K. Tachikawa, and A. Manz, "Micro Total Analysis Systems. Latest Advancements and Trends," *Anal. Chem.*, vol. 78, no. 12, pp. 3887–3908, 2006, doi: 10.1021/ac0605602.
- [8] R. B. Fair, *Digital microfluidics: Is a true lab-on-a-chip possible?*, vol. 3, no. 3. 2007.
- [9] H. Song and R. F. Ismagilov, "Millisecond Kinetics on a Microfluidic Chip Using Nanoliters of Reagents," *J. Am. Chem. Soc.*, vol. 125, no. 47, pp. 14613–14619, 2003, doi: 10.1021/ja0354566.
- [10] J. U. Shim, G. Cristobal, D. R. Link, T. Thorsen, and S. Fraden, "Using microfluidics to decouple nucleation and growth of protein crystals," *Cryst. Growth Des.*, vol. 7, no. 11, pp. 2192–2194, 2007, doi: 10.1021/cg700688f.
- [11] B. Zheng, L. S. Roach, and R. F. Ismagilov, "Screening of protein crystallization conditions on a microfluidic chip using nanoliter-size droplets," *J. Am. Chem. Soc.*, vol. 125, no. 37, pp. 11170–11171, 2003, doi: 10.1021/ja037166v.
- [12] T. A. Crowley and V. Pizziconi, "Isolation of plasma from whole blood using planar microfilters for lab-on-a-chip applications," *Lab Chip*, vol. 5, no. 9, pp. 922–929, 2005,

- doi: 10.1039/b502930a.
- [13] K. H. Han and A. B. Frazier, "Paramagnetic capture mode magnetophoretic microseparator for high efficiency blood cell separations," *Lab Chip*, vol. 6, no. 2, pp. 265–273, 2006, doi: 10.1039/b514539b.
  - [14] M. He, J. S. Edgar, G. D. M. Jeffries, R. M. Lorenz, J. P. Shelby, and D. T. Chiu, "Selective encapsulation of single cells and subcellular organelles into picoliter- and femtoliter-volume droplets," *Anal. Chem.*, vol. 77, no. 6, pp. 1539–1544, 2005, doi: 10.1021/ac0480850.
  - [15] J. H. Kim, T. Y. Jeon, T. M. Choi, T. S. Shim, S. H. Kim, and S. M. Yang, "Droplet microfluidics for producing functional microparticles," *Langmuir*, vol. 30, no. 6, pp. 1473–1488, 2014, doi: 10.1021/la403220p.
  - [16] E. Rondeau and J. J. Cooper-White, "Biopolymer microparticle and nanoparticle formation within a microfluidic device," *Langmuir*, vol. 24, no. 13, pp. 6937–6945, 2008, doi: 10.1021/la703339u.
  - [17] S. Vyawahare, A. D. Griffiths, and C. A. Merten, "Miniaturization and parallelization of biological and chemical assays in microfluidic devices," *Chem. Biol.*, vol. 17, no. 10, pp. 1052–1065, 2010, doi: 10.1016/j.chembiol.2010.09.007.
  - [18] A. B. Theberge *et al.*, "Microdroplets in microfluidics: An evolving platform for discoveries in chemistry and biology," *Angew. Chemie - Int. Ed.*, vol. 49, no. 34, pp. 5846–5868, 2010, doi: 10.1002/anie.200906653.
  - [19] A. Abou-Hassan, O. Sandre, and V. Cabuil, "Microfluidics in inorganic chemistry," *Angew. Chemie - Int. Ed.*, vol. 49, no. 36, pp. 6268–6286, 2010, doi: 10.1002/anie.200904285.
  - [20] S. L. Sjoström *et al.*, "High-throughput screening for industrial enzyme production hosts by droplet microfluidics," *Lab Chip*, vol. 14, no. 4, pp. 806–813, 2014, doi: 10.1039/c3lc51202a.
  - [21] M. Sesen, T. Alan, and A. Neild, "Droplet control technologies for microfluidic high throughput screening ( $\mu$ HTS)," *Lab Chip*, vol. 17, no. 14, pp. 2372–2394, 2017, doi: 10.1039/C7LC00005G.
  - [22] X. Niu, F. Gielen, J. B. Edel, and A. J. DeMello, "A microdroplet dilutor for high-throughput screening," *Nat. Chem.*, vol. 3, no. 6, pp. 437–442, 2011, doi: 10.1038/nchem.1046.
  - [23] E. Brouzes *et al.*, "Droplet microfluidic technology for single-cell high-throughput screening," *Proc. Natl. Acad. Sci. U. S. A.*, vol. 106, no. 34, pp. 14195–14200, 2009,



- doi: 10.1073/pnas.0903542106.
- [24] S. A. Sundberg, “High-throughput and ultra-high-throughput screening: Solution- and cell-based approaches,” *Curr. Opin. Biotechnol.*, vol. 11, no. 1, pp. 47–53, 2000, doi: 10.1016/S0958-1669(99)00051-8.
  - [25] T. Thorsen, R. W. Roberts, F. H. Arnold, and S. R. Quake, “Dynamic pattern formation in a vesicle-generating microfluidic device,” *Phys. Rev. Lett.*, vol. 86, no. 18, pp. 4163–4166, 2001, doi: 10.1103/PhysRevLett.86.4163.
  - [26] S. L. Anna, N. Bontoux, and H. A. Stone, “Formation of dispersions using ‘flow focusing’ in microchannels,” *Appl. Phys. Lett.*, vol. 82, no. 3, pp. 364–366, 2003, doi: 10.1063/1.1537519.
  - [27] P. B. Umbanhowar, V. Prasad, and D. A. Weitz, “Monodisperse emulsion generation via drop break off in a coflowing stream,” *Langmuir*, vol. 16, no. 2, pp. 347–351, 2000, doi: 10.1021/la990101e.
  - [28] Z. Z. Chong, S. H. Tan, A. M. Gañán-Calvo, S. B. Tor, N. H. Loh, and N. T. Nguyen, “Active droplet generation in microfluidics,” *Lab Chip*, vol. 16, no. 1, pp. 35–58, 2016, doi: 10.1039/c5lc01012h.
  - [29] S. H. Jin, H. H. Jeong, B. Lee, S. S. Lee, and C. S. Lee, “A programmable microfluidic static droplet array for droplet generation, transportation, fusion, storage, and retrieval,” *Lab Chip*, vol. 15, no. 18, pp. 3677–3686, 2015, doi: 10.1039/c5lc00651a.
  - [30] S. Zeng, B. Li, X. Su, J. Qin, and B. Lin, “Microvalve-actuated precise control of individual droplets in microfluidic devices,” *Lab Chip*, vol. 9, no. 10, pp. 1340–1343, 2009, doi: 10.1039/b821803j.
  - [31] A. R. Abate, M. B. Romanowsky, J. J. Agresti, and D. A. Weitz, “Valve-based flow focusing for drop formation,” *Appl. Phys. Lett.*, vol. 94, no. 2, pp. 92–95, 2009, doi: 10.1063/1.3067862.
  - [32] D. J. Collins, T. Alan, K. Helmersson, and A. Neild, “Surface acoustic waves for on-demand production of picoliter droplets and particle encapsulation,” *Lab Chip*, vol. 13, no. 16, pp. 3225–3231, 2013, doi: 10.1039/c3lc50372k.
  - [33] L. Schmid and T. Franke, “SAW-controlled drop size for flow focusing,” *Lab Chip*, vol. 13, no. 9, p. 1691, 2013, doi: 10.1039/c3lc41233d.
  - [34] L. Schmid and T. Franke, “Acoustic modulation of droplet size in a T-junction,” *Appl. Phys. Lett.*, vol. 104, no. 13, p. 133501, 2014, doi: 10.1063/1.4869536.
  - [35] R. Ahmed and T. B. Jones, “Dispensing picoliter droplets on substrates using dielectrophoresis,” *J. Electrostat.*, vol. 64, no. 7–9, pp. 543–549, 2006, doi:

- 10.1016/j.elstat.2005.10.008.
- [36] R. Ahmed and T. B. Jones, “Optimized liquid DEP droplet dispensing,” *J. Micromechanics Microengineering*, vol. 17, no. 5, pp. 1052–1058, 2007, doi: 10.1088/0960-1317/17/5/027.
  - [37] K. L. Wang, T. B. Jones, and A. Raisanen, “Dynamic control of DEP actuation and droplet dispensing,” *J. Micromechanics Microengineering*, vol. 17, no. 1, pp. 76–80, 2007, doi: 10.1088/0960-1317/17/1/010.
  - [38] T. B. Jones, M. Gunji, M. Washizu, and M. J. Feldman, “Dielectrophoretic liquid actuation and nanodroplet formation,” *J. Appl. Phys.*, vol. 89, no. 2, pp. 1441–1448, 2001, doi: 10.1063/1.1332799.
  - [39] T. B. Jones, “Liquid dielectrophoresis on the microscale,” *J. Electrostat.*, vol. 51–52, no. 1–4, pp. 290–299, 2001, doi: 10.1016/S0304-3886(01)00074-2.
  - [40] S. K. Cho, H. Moon, and C. J. Kim, “Creating, transporting, cutting, and merging liquid droplets by electrowetting-based actuation for digital microfluidic circuits,” *J. Microelectromechanical Syst.*, vol. 12, no. 1, pp. 70–80, 2003, doi: 10.1109/JMEMS.2002.807467.
  - [41] J. Lee, H. Moon, J. Fowler, T. Schoellhammer, and C. J. Kim, “Electrowetting and electrowetting-on-dielectric for microscale liquid handling,” *Sensors Actuators, A Phys.*, vol. 95, no. 2–3, pp. 259–268, 2002, doi: 10.1016/S0924-4247(01)00734-8.
  - [42] J. Berthier *et al.*, “Computer aided design of an EWOD microdevice,” *Sensors Actuators, A Phys.*, vol. 127, no. 2, pp. 283–294, 2006, doi: 10.1016/j.sna.2005.09.026.
  - [43] S. M. S. Murshed, S. H. Tan, N. T. Nguyen, T. N. Wong, and L. Yobas, “Microdroplet formation of water and nanofluids in heat-induced microfluidic T-junction,” *Microfluid. Nanofluidics*, vol. 6, no. 2, pp. 253–259, 2009, doi: 10.1007/s10404-008-0323-3.
  - [44] Y. F. Yap, S. H. Tan, N. T. Nguyen, S. M. S. Murshed, T. N. Wong, and L. Yobas, “Thermally mediated control of liquid microdroplets at a bifurcation,” *J. Phys. D. Appl. Phys.*, vol. 42, no. 6, 2009, doi: 10.1088/0022-3727/42/6/065503.
  - [45] C. A. Stan, S. K. Y. Tang, and G. M. Whitesides, “Independent control of drop size and velocity in microfluidic flow-focusing generators using variable temperature and flow rate,” *Anal. Chem.*, vol. 81, no. 6, pp. 2399–2402, 2009, doi: 10.1021/ac8026542.
  - [46] S. M. S. Murshed, S. H. Tan, and N. T. Nguyen, “Temperature dependence of interfacial properties and viscosity of nanofluids for droplet-based microfluidics,” *J. Phys. D. Appl. Phys.*, vol. 41, no. 8, 2008, doi: 10.1088/0022-3727/41/8/085502.
  - [47] N. T. Nguyen *et al.*, “Thermally mediated droplet formation in microchannels,” *Appl.*

- Phys. Lett.*, vol. 91, no. 8, pp. 89–92, 2007, doi: 10.1063/1.2773948.
- [48] J. Liu, Y. F. Yap, and N. T. Nguyen, “Numerical study of the formation process of ferrofluid droplets,” *Phys. Fluids*, vol. 23, no. 7, 2011, doi: 10.1063/1.3614569.
  - [49] J. Liu, S. H. Tan, Y. F. Yap, M. Y. Ng, and N. T. Nguyen, “Numerical and experimental investigations of the formation process of ferrofluid droplets,” *Microfluid. Nanofluidics*, vol. 11, no. 2, pp. 177–187, 2011, doi: 10.1007/s10404-011-0784-7.
  - [50] Y. Wu, T. Fu, Y. Ma, and H. Z. Li, “Ferrofluid droplet formation and breakup dynamics in a microfluidic flow-focusing device,” *Soft Matter*, vol. 9, no. 41, pp. 9792–9798, 2013, doi: 10.1039/c3sm51860d.
  - [51] C. P. Lee, T. S. Lan, and M. F. Lai, “Fabrication of two-dimensional ferrofluid microdroplet lattices in a microfluidic channel,” *J. Appl. Phys.*, vol. 115, no. 17, pp. 1–4, 2014, doi: 10.1063/1.4867964.
  - [52] P. Garstecki, M. J. Fuerstman, H. A. Stone, and G. M. Whitesides, “Formation of droplets and bubbles in a microfluidic T-junction - Scaling and mechanism of break-up,” *Lab Chip*, vol. 6, no. 3, pp. 437–446, 2006, doi: 10.1039/b510841a.
  - [53] M. De Menech, P. Garstecki, F. Jousse, and H.A.Stone, “Transition from squeezing to dripping in a microfluidic T-shaped junction,” *J. Fluid Mech.*, vol. 595, pp. 141–161, 2008, doi: 10.1017/S002211200700910X.
  - [54] P. Garstecki, M. . Fuerstman, and G. M. H A Stone Whitesides, “Formation of droplets and bubbles in a microfluidic T-junction-scaling and mechanism of break-up,” *Lab Chip*, vol. 6, no. 3, pp. 437–446, 2006, doi: 10.1039/b510841a.
  - [55] P. Garstecki, H. A. Stone, and G. M. Whitesides, “Mechanism for flow-rate controlled breakup in confined geometries: A route to monodisperse emulsions,” *Phys. Rev. Lett.*, vol. 94, no. 16, pp. 1–4, 2005, doi: 10.1103/PhysRevLett.94.164501.
  - [56] D. R. Link, S. L. Anna, D. A. Weitz, and H. A. Stone, “Geometrically Mediated Breakup of Drops in Microfluidic Devices,” *Phys. Rev. Lett.*, vol. 92, no. 5, p. 054503, 2004, doi: 10.1103/PhysRevLett.92.054503.
  - [57] L. Ménétrier-Deremble and P. Tabeling, “Droplet breakup in microfluidic junctions of arbitrary angles,” *Phys. Rev. E*, vol. 74, no. 3, p. 035303(R), 2006, doi: 10.1103/PhysRevE.74.035303.
  - [58] M. C. Jullien, M. J. Tsang Mui Ching, C. Cohen, L. Menetrier, and P. Tabeling, “Droplet breakup in microfluidic T-junctions at small capillary numbers,” *Phys. Fluids*, vol. 21, no. 7, p. 072001, 2009, doi: 10.1063/1.3170983.
  - [59] V. Cristini and Y.-C. Tan, “Theory and numerical simulation of droplet dynamics in

- complex flows-a review,” *Lab Chip*, vol. 4, no. 4, pp. 257–264, 2004, doi: 10.1039/b403226h.
- [60] D. A. Hoang, L. M. Portela, C. R. Kleijn, M. T. Kreutzer, and V. van Steijn, “Dynamics of droplet breakup in a T-junction,” *J. Fluid Mech.*, vol. 717, p. R4, 2013, doi: 10.1017/jfm.2013.18.
- [61] M. De Menech, “Modeling of droplet breakup in a microfluidic T-shaped junction with a phase-field model,” *Phys. Rev. E - Stat. Nonlinear, Soft Matter Phys.*, vol. 73, no. 3, pp. 1–9, 2006, doi: 10.1103/PhysRevE.73.031505.
- [62] M. A. Leshansky and M. L. Pismen, “Breakup of drops in a microfluidic T junction,” *Phys. Fluids*, vol. 21, no. 2, pp. 1–6, 2009, doi: 10.1063/1.3078515.
- [63] D. R. Link *et al.*, “Electric control of droplets in microfluidic devices,” *Angew. Chemie - Int. Ed.*, vol. 45, no. 16, pp. 2556–2560, 2006, doi: 10.1002/anie.200503540.
- [64] B. Ahn, K. Lee, R. Panchapakesan, and K. W. Oh, “On-demand electrostatic droplet charging and sorting,” *Biomicrofluidics*, vol. 5, no. 2, p. 024113, 2011, doi: 10.1063/1.3604393.
- [65] B. Ahn, K. Lee, R. Louge, and K. W. Oh, “Concurrent droplet charging and sorting by electrostatic actuation,” *Biomicrofluidics*, vol. 3, no. 4, 2009, doi: 10.1063/1.3250303.
- [66] F. Guo *et al.*, “Droplet electric separator microfluidic device for cell sorting,” *Appl. Phys. Lett.*, vol. 96, no. 19, 2010, doi: 10.1063/1.3360812.
- [67] H. D. Xi *et al.*, “Active droplet sorting in microfluidics: a review,” *Lab Chip*, vol. 17, no. 5, pp. 751–771, 2017, doi: 10.1039/c6lc01435f.
- [68] K. Ahn, C. Kerbage, T. P. Hunt, R. M. Westervelt, D. R. Link, and D. A. Weitz, “Dielectrophoretic manipulation of drops for high-speed microfluidic sorting devices,” *Appl. Phys. Lett.*, vol. 88, no. 2, p. 024104, 2006, doi: 10.1063/1.2164911.
- [69] R. Pethig, “Dielectrophoresis: Status of the theory, technology, and applications,” *Biomicrofluidics*, vol. 4, no. 2, 2010, doi: 10.1063/1.3456626.
- [70] A. M. Pit, R. de Ruiter, A. Kumar, D. Wijnperlé, M. H. G. Duits, and F. Mugele, “High-throughput sorting of drops in microfluidic chips using electric capacitance,” *Biomicrofluidics*, vol. 9, no. 4, 2015, doi: 10.1063/1.4928452.
- [71] J.-C. Baret *et al.*, “Fluorescence-activated droplet sorting (FADS): efficient microfluidic cell sorting based on enzymatic activity,” *Lab Chip*, vol. 9, no. 13, pp. 1850–8, 2009, doi: 10.1039/b902504a.
- [72] Adam Sciambia and Adam R. Abate, “Accurate microfluidic sorting of droplets at 30 kHz,” *Lab Chip*, 2012, doi: 10.1039/x0xx00000x.

- [73] C. N. Baroud, M. Robert de Saint Vincent, and J.-P. Delville, “An optical toolbox for total control of droplet microfluidics,” *Lab Chip*, vol. 7, no. 8, p. 1029, 2007, doi: 10.1039/b702472j.
- [74] C. N. Baroud, J. P. Delville, F. Gallaire, and R. Wunenburger, “Thermocapillary valve for droplet production and sorting,” *Phys. Rev. E - Stat. Nonlinear, Soft Matter Phys.*, vol. 75, no. 4, pp. 1–5, 2007, doi: 10.1103/PhysRevE.75.046302.
- [75] T. H. Ting, Y. F. Yap, N. T. Nguyen, T. N. Wong, J. C. K. Chai, and L. Yobas, “Thermally mediated breakup of drops in microchannels,” *Appl. Phys. Lett.*, vol. 89, no. 23, 2006, doi: 10.1063/1.2400200.
- [76] T. Franke, A. R. Abate, D. A. Weitz, and A. Wixforth, “Surface acoustic wave (SAW) directed droplet flow in microfluidics for PDMS devices,” *Lab Chip*, vol. 9, no. 18, pp. 2625–2627, 2009, doi: 10.1039/b906819h.
- [77] M. Sesen, T. Alan, and A. Neild, “Microfluidic plug steering using surface acoustic waves,” *Lab Chip*, vol. 15, no. 14, pp. 3030–3038, 2015, doi: 10.1039/c5lc00468c.
- [78] J. H. Jung, G. Destgeer, B. Ha, J. Park, and H. J. Sung, “On-demand droplet splitting using surface acoustic waves,” *Lab Chip*, vol. 16, no. 17, pp. 3235–3243, 2016, doi: 10.1039/c6lc00648e.
- [79] X. Ding *et al.*, “Surface acoustic wave microfluidics,” *Lab Chip*, vol. 13, no. 18, pp. 3626–3649, 2013, doi: 10.1039/c3lc50361e.
- [80] M. Sesen, C. Devendran, S. Malikides, T. Alan, and A. Neild, “Surface acoustic wave enabled pipette on a chip,” *Lab Chip*, vol. 17, no. 3, pp. 438–447, 2017, doi: 10.1039/c6lc01318j.
- [81] G. Destgeer and H. J. Sung, “Recent advances in microfluidic actuation and micro-object manipulation via surface acoustic waves,” *Lab Chip*, vol. 15, no. 13, pp. 2722–2738, 2015, doi: 10.1039/c5lc00265f.
- [82] D. B. Weibel, M. Kruithof, S. Potenta, S. K. Sia, A. Lee, and G. M. Whitesides, “Torque-actuated valves for microfluidics,” *Anal. Chem.*, vol. 77, no. 15, pp. 4726–4733, 2005, doi: 10.1021/ac048303p.
- [83] P. M. Pilarski, S. Adamia, and C. J. Backhouse, “An adaptable microvalving system for on-chip polymerase chain reactions,” *J. Immunol. Methods*, vol. 305, no. 1, pp. 48–58, 2005, doi: 10.1016/j.jim.2005.07.009.
- [84] C. M. Pemble and B. C. Towe, “Miniature shape memory alloy pinch valve,” *Sensors Actuators, A Phys.*, vol. 77, no. 2, pp. 145–148, 1999, doi: 10.1016/S0924-4247(99)00157-0.

- [85] D. B. Weibel, A. C. Siegel, A. Lee, A. H. George, and G. M. Whitesides, "Pumping fluids in microfluidic systems using the elastic deformation of poly(dimethylsiloxane)," *Lab Chip*, vol. 7, no. 12, pp. 1832–1836, 2007, doi: 10.1039/b714664g.
- [86] G. V. Kaigala, V. N. Hoang, and C. J. Backhouse, "Electrically controlled microvalves to integrate microchip polymerase chain reaction and capillary electrophoresis," *Lab Chip*, vol. 8, no. 7, pp. 1071–1078, 2008, doi: 10.1039/b802853b.
- [87] D. E. Lee, S. Soper, and W. Wang, "Design and fabrication of an electrochemically actuated microvalve," *Microsyst. Technol.*, vol. 14, no. 9–11, pp. 1751–1756, 2008, doi: 10.1007/s00542-008-0594-3.
- [88] N. Sundararajan, D. Kim, and A. A. Berlin, "Microfluidic operations using deformable polymer membranes fabricated by single layer soft lithography," *Lab Chip*, vol. 5, no. 3, pp. 350–354, 2005, doi: 10.1039/b500792p.
- [89] M. A. Unger, H. P. Chou, T. Thorsen, A. Scherer, and S. R. Quake, "Monolithic microfabricated valves and pumps by multilayer soft lithography," *Science (80-. )*, vol. 288, no. 5463, pp. 113–116, 2000, doi: 10.1126/science.288.5463.113.
- [90] K. Hosokawa and R. Maeda, "Pneumatically-actuated three-way microvalve fabricated with polydimethylsiloxane using the membrane transfer technique," *J. Micromechanics Microengineering*, vol. 10, no. 3, pp. 415–420, 2000, doi: 10.1088/0960-1317/10/3/317.
- [91] V. Studer, G. Hang, A. Pandolfi, M. Ortiz, W. F. Anderson, and S. R. Quake, "Scaling properties of a low-actuation pressure microfluidic valve," *J. Appl. Phys.*, vol. 95, no. 1, pp. 393–398, 2004, doi: 10.1063/1.1629781.
- [92] W. H. Grover, A. M. Skelley, C. N. Liu, E. T. Lagally, and R. A. Mathies, "Monolithic membrane valves and diaphragm pumps for practical large-scale integration into glass microfluidic devices," *Sensors Actuators, B Chem.*, vol. 89, no. 3, pp. 315–323, 2003, doi: 10.1016/S0925-4005(02)00468-9.
- [93] A. R. Abate and D. A. Weitz, "Single-layer membrane valves for elastomeric microfluidic devices," *Appl. Phys. Lett.*, vol. 92, no. 24, pp. 1–4, 2008, doi: 10.1063/1.2945797.
- [94] Y. Chen, Y. Tian, Z. Xu, X. Wang, S. Yu, and L. Dong, "Microfluidic droplet sorting using integrated bilayer micro-valves," *Appl. Phys. Lett.*, vol. 109, no. 14, 2016, doi: 10.1063/1.4964644.
- [95] J. H. Choi, S. K. Lee, J. M. Lim, S. M. Yang, and G. R. Yi, "Designed pneumatic valve actuators for controlled droplet breakup and generation," *Lab Chip*, vol. 10, no. 4, pp. 456–461, 2010, doi: 10.1039/b915596a.

- [96] A. R. Abate, J. J. Agresti, and D. A. Weitz, "Microfluidic sorting with high-speed single-layer membrane valves," *Appl. Phys. Lett.*, vol. 96, no. 20, 2010, doi: 10.1063/1.3431281.
- [97] D. H. Yoon, J. Ito, T. Sekiguchi, and S. Shoji, "Active and precise control of microdroplet division using horizontal pneumatic valves in bifurcating microchannel," *Micromachines*, vol. 4, no. 2, pp. 197–205, 2013, doi: 10.3390/mi4020197.
- [98] C. G. Yang, Z. R. Xu, and J. H. Wang, "Manipulation of droplets in microfluidic systems," *TrAC - Trends Anal. Chem.*, vol. 29, no. 2, pp. 141–157, 2010, doi: 10.1016/j.trac.2009.11.002.
- [99] E. Klaseboer, J. P. Chevaillier, C. Gourdon, and O. Masbernat, "Film drainage between colliding drops at constant approach velocity: Experiments and modeling," *J. Colloid Interface Sci.*, vol. 229, no. 1, pp. 274–285, 2000, doi: 10.1006/jcis.2000.6987.
- [100] S. Y. Teh, R. Lin, L.-H. Hung, and A. P. Lee, "Droplet microfluidics," *Lab Chip*, vol. 8, no. 2, pp. 198–220, 2008, doi: 10.1039/b715524g.
- [101] L. Li, J. Q. Boedicker, and R. F. Ismagilov, "Using a multijunction microfluidic device to inject substrate into an array of preformed plugs without cross-contamination: Comparing theory and experiments," *Anal. Chem.*, vol. 79, no. 7, pp. 2756–2761, 2007, doi: 10.1021/ac062179n.
- [102] L.-H. Hung, K. M. Choi, W.-Y. Tseng, Y.-C. Tan, K. J. Shea, and A. P. Lee, "Alternating droplet generation and controlled dynamic droplet fusion in microfluidic device for CdS nanoparticle synthesis," *Lab Chip*, vol. 6, no. 2, pp. 174–178, 2006, doi: 10.1039/b513908b.
- [103] K. Liu, H. Ding, Y. Chen, and X. Z. Zhao, "Droplet-based synthetic method using microflow focusing and droplet fusion," *Microfluid. Nanofluidics*, vol. 3, no. 2, pp. 239–243, 2007, doi: 10.1007/s10404-006-0121-8.
- [104] Y. C. Tan, Y. L. Ho, and A. P. Lee, "Droplet coalescence by geometrically mediated flow in microfluidic channels," *Microfluid. Nanofluidics*, vol. 3, no. 4, pp. 495–499, 2007, doi: 10.1007/s10404-006-0136-1.
- [105] Y.-C. Tan, J. S. Fisher, A. I. Lee, V. Cristini, and A. P. Lee, "Design of microfluidic channel geometries for the control of droplet volume, chemical concentration, and sorting," *Lab Chip*, vol. 4, no. 4, pp. 292–298, 2004, doi: 10.1039/b403280m.
- [106] X. Niu, S. Gulati, J. B. Edel, and A. J. deMello, "Pillar-induced droplet merging in microfluidic circuits," *Lab Chip*, vol. 8, no. 11, p. 1837, 2008, doi: 10.1039/b813325e.
- [107] L. M. Fidalgo, C. Abell, and W. T. S. Huck, "Surface-induced droplet fusion in

- microfluidic devices,” *Lab Chip*, vol. 7, no. 8, p. 984, 2007, doi: 10.1039/b708091c.
- [108] A. Liau, R. Kamik, A. Majumdar, and J. H. D. Cate, “Mixing crowded biological solutions in milliseconds,” *Anal. Chem.*, vol. 77, no. 23, pp. 7618–7625, 2005, doi: 10.1021/ac050827h.
- [109] J. Wang and C. Lu, “Microfluidic cell fusion under continuous direct current voltage,” *Appl. Phys. Lett.*, vol. 89, no. 23, pp. 2004–2007, 2006, doi: 10.1063/1.2402122.
- [110] P. Singh and N. Aubry, “Transport and deformation of droplets in a microdevice using dielectrophoresis,” *Electrophoresis*, vol. 28, no. 4, pp. 644–657, 2007, doi: 10.1002/elps.200600549.
- [111] K. Ahn, J. Agresti, H. Chong, M. Marquez, and D. A. Weitz, “Electrocoalescence of drops synchronized by size-dependent flow in microfluidic channels,” *Appl. Phys. Lett.*, vol. 88, no. 26, 2006, doi: 10.1063/1.2218058.
- [112] C. Priest, S. Herminghaus, and R. Seemann, “Controlled electrocoalescence in microfluidics: Targeting a single lamella,” *Appl. Phys. Lett.*, vol. 89, no. 13, 2006, doi: 10.1063/1.2357039.
- [113] M. Sesen, T. Alan, and A. Neild, “Microfluidic on-demand droplet merging using surface acoustic waves,” *Lab Chip*, vol. 14, no. 17, pp. 3325–3333, 2014, doi: 10.1039/c4lc00456f.
- [114] B. A. Korshak, V. G. Mozhaev, and A. V. Zyryanova, “Observation and interpretation of SAW-induced regular and chaotic dynamics of droplet shape,” *Proc. - IEEE Ultrason. Symp.*, vol. 2, no. c, pp. 1019–1022, 2005, doi: 10.1109/ULTSYM.2005.1603024.
- [115] A. Jamshaid, M. Igaki, D. H. Yoon, T. Sekiguchi, and S. Shoji, “Controllable active micro droplets merging device using horizontal pneumatic micro valves,” *Micromachines*, vol. 4, no. 1, pp. 34–48, 2013, doi: 10.3390/mi4010034.
- [116] R. M. Lorenz, J. S. Edgar, G. D. M. Jeffries, and D. T. Chiu, “Microfluidic and optical systems for the on-demand generation and manipulation of single femtoliter-volume aqueous droplets,” *Anal. Chem.*, vol. 78, no. 18, pp. 6433–6439, 2006, doi: 10.1021/ac060748l.
- [117] J. M. Köhler *et al.*, “Digital reaction technology by micro segmented flow - components, concepts and applications,” *Chem. Eng. J.*, vol. 101, no. 1–3, pp. 201–216, 2004, doi: 10.1016/j.cej.2003.11.025.
- [118] A. Huebner, S. Sharma, M. Srisa-Art, F. Hollfelder, J. B. Edel, and A. J. deMello, “Microdroplets: A sea of applications?,” *Lab Chip*, vol. 8, no. 8, p. 1244, 2008, doi: 10.1039/b806405a.



- [119] D. J. Collins, A. Neild, A. deMello, A.-Q. Liu, and Y. Ai, “The Poisson distribution and beyond: methods for microfluidic droplet production and single cell encapsulation,” *Lab Chip*, vol. 15, no. 17, pp. 3439–3459, 2015, doi: 10.1039/C5LC00614G.
- [120] H. Zhang, E. Tumarkin, R. M. A. Sullan, G. C. Walker, and E. Kumacheva, “Exploring microfluidic routes to microgels of biological polymers,” *Macromol. Rapid Commun.*, vol. 28, no. 5, pp. 527–538, 2007, doi: 10.1002/marc.200600776.
- [121] C. N. Baroud, F. Gallaire, and R. Danga, “Dynamics of microfluidic droplets,” *Lab Chip*, vol. 10, no. 16, p. 2032, 2010, doi: 10.1039/c001191f.
- [122] J. D. Tice, H. Song, A. D. Lyon, and R. F. Ismagilov, “Formation of Droplets and Mixing in Multiphase Microfluidics at Low Values of the Reynolds and the Capillary Numbers,” *Langmuir*, vol. 19, no. 22, pp. 9127–9133, 2003, doi: 10.1021/la030090w.
- [123] S. Okushima, T. Nisisako, T. Torii, and T. Higuchi, “Controlled production of monodisperse double emulsions by two-step droplet breakup in microfluidic devices,” *Langmuir*, vol. 20, no. 23, pp. 9905–9908, 2004, doi: 10.1021/la0480336.
- [124] A. M. Gañán-Calvo and J. M. Gordillo, “Perfectly Monodisperse Microbubbling by Capillary Flow Focusing,” *Phys. Rev. Lett.*, vol. 87, no. 27, p. 274501, 2001, doi: 10.1103/PhysRevLett.87.274501.
- [125] L. L. A. Adams, T. E. Kodger, S.-H. Kim, H. C. Shum, T. Franke, and D. A. Weitz, “Single step emulsification for the generation of multi-component double emulsions,” *Soft Matter*, vol. 8, no. 41, p. 10719, 2012, doi: 10.1039/c2sm25953b.
- [126] J. Hong, M. Choi, J. B. Edel, and A. J. deMello, “Passive self-synchronized two-droplet generation,” *Lab Chip*, vol. 10, no. 20, p. 2702, 2010, doi: 10.1039/c005136e.
- [127] D. Huh *et al.*, “Gravity-driven microfluidic particle sorting device with hydrodynamic separation amplification,” *Anal. Chem.*, vol. 79, no. 4, pp. 1369–1376, 2007, doi: 10.1021/ac061542n.
- [128] H. Lee, L. Xu, B. Ahn, K. Lee, and K. W. Oh, “Continuous-flow in-droplet magnetic particle separation in a droplet-based microfluidic platform,” *Microfluid. Nanofluidics*, vol. 13, no. 4, pp. 613–623, 2012, doi: 10.1007/s10404-012-0978-7.
- [129] M. Sesen, T. Alan, and A. Neild, “Microfluidic on-demand droplet merging using surface acoustic waves,” *Lab Chip*, vol. 14, no. 17, p. 3325, 2014, doi: 10.1039/c4lc00456f.
- [130] J. C. Brenker, D. J. Collins, H. Van Phan, T. Alan, and A. Neild, “On-chip droplet production regimes using surface acoustic waves,” *Lab Chip*, vol. 16, no. 9, pp. 1675–1683, 2016, doi: 10.1039/C5LC01341K.

- [131] Z. Nie *et al.*, “Emulsification in a microfluidic flow-focusing device: Effect of the viscosities of the liquids,” *Microfluid. Nanofluidics*, vol. 5, no. 5, pp. 585–594, 2008, doi: 10.1007/s10404-008-0271-y.
- [132] H. Liu and Y. Zhang, “Droplet formation in a T-shaped microfluidic junction,” *J. Appl. Phys.*, vol. 106, no. 3, p. 034906, 2009, doi: 10.1063/1.3187831.
- [133] G. F. Christopher, N. N. Noharuddin, J. A. Taylor, and S. L. Anna, “Experimental observations of the squeezing-to-dripping transition in T-shaped microfluidic junctions,” *Phys. Rev. E*, vol. 78, no. 3, p. 036317, 2008, doi: 10.1103/PhysRevE.78.036317.
- [134] S. S. Bithi and S. A. Vanapalli, “Collective dynamics of non-coalescing and coalescing droplets in microfluidic parking networks,” *Soft Matter*, vol. 11, no. 25, pp. 5122–5132, 2015, doi: 10.1039/C5SM01077B.
- [135] R. Gao, Z. Cheng, A. J. Demello, and J. Choo, “Wash-free magnetic immunoassay of the PSA cancer marker using SERS and droplet microfluidics,” *Lab Chip*, vol. 16, no. 6, pp. 1022–1029, 2016, doi: 10.1039/c5lc01249j.
- [136] D. L. Chen, L. Li, S. Reyes, D. N. Adamson, and R. F. Ismagilov, “Using three-phase flow of immiscible liquids to prevent coalescence of droplets in microfluidic channels: Criteria to identify the third liquid and validation with protein crystallization,” *Langmuir*, vol. 23, no. 4, pp. 2255–2260, 2007, doi: 10.1021/la062152z.
- [137] P. S. Dittrich and A. Manz, “Lab-on-a-chip: Microfluidics in drug discovery,” *Nat. Rev. Drug Discov.*, vol. 5, no. 3, pp. 210–218, 2006, doi: 10.1038/nrd1985.
- [138] D. K. Kang *et al.*, “3D Droplet Microfluidic Systems for High-Throughput Biological Experimentation,” *Anal. Chem.*, vol. 87, no. 21, pp. 10770–10778, 2015, doi: 10.1021/acs.analchem.5b02402.
- [139] D. N. Josephides and S. Sajjadi, “Increased drop formation frequency via reduction of surfactant interactions in flow-focusing microfluidic devices,” *Langmuir*, vol. 31, no. 3, pp. 1218–1224, 2015, doi: 10.1021/la504299r.
- [140] T. Glawdel, C. Elbuken, and C. L. Ren, “Droplet formation in microfluidic T-junction generators operating in the transitional regime. I. Experimental observations,” *Phys. Rev. E - Stat. Nonlinear, Soft Matter Phys.*, vol. 85, no. 1, pp. 1–9, 2012, doi: 10.1103/PhysRevE.85.016322.
- [141] M. R. Raveshi, S. N. Agnihotri, M. Sesen, R. Bhardwaj, and A. Neild, “Sensors and Actuators B: Chemical Selective droplet splitting using single layer micro fluidic valves,” *Sensors Actuators B. Chem.*, vol. 292, no. April, pp. 233–240, 2019, doi:

10.1016/j.snb.2019.04.115.

- [142] D. N. Adamson, D. Mustafi, J. X. J. Zhang, B. Zheng, and R. F. Ismagilov, "Production of arrays of chemically distinct nanolitre plugs via repeated splitting in microfluidic devices," *Lab Chip*, vol. 6, no. 9, pp. 1178–1186, 2006, doi: 10.1039/b604993a.
- [143] A. C. Hatch *et al.*, "1-Million droplet array with wide-field fluorescence imaging for digital PCR," *Lab Chip*, vol. 11, no. 22, pp. 3838–3845, 2011, doi: 10.1039/c1lc20561g.
- [144] J. Clausell-Tormos, A. D. Griffiths, and C. A. Merten, "An automated two-phase microfluidic system for kinetic analyses and the screening of compound libraries," *Lab Chip*, vol. 10, no. 10, pp. 1302–1307, 2010, doi: 10.1039/b921754a.
- [145] E. Um, M. E. Rogers, and H. A. Stone, "Combinatorial generation of droplets by controlled assembly and coalescence," *Lab Chip*, vol. 13, no. 23, pp. 4674–4680, 2013, doi: 10.1039/c3lc50957e.
- [146] K. Akamatsu, K. Minezaki, M. Yamada, M. Seki, and S. I. Nakao, "Direct Observation of Splitting in Oil-In-Water-In-Oil Emulsion Droplets via a Microchannel Mimicking Membrane Pores," *Langmuir*, vol. 33, no. 49, pp. 14087–14092, 2017, doi: 10.1021/acs.langmuir.7b03331.
- [147] S. R. Doonan and R. C. Bailey, "K-Channel: A Multifunctional Architecture for Dynamically Reconfigurable Sample Processing in Droplet Microfluidics," *Analytical Chemistry*, vol. 89, no. 7, pp. 4091–4099, 2017, doi: 10.1021/acs.analchem.6b05041.
- [148] S. N. Agnihotri, M. R. Raveshi, R. Bhardwaj, and A. Neild, "Droplet Breakup at the Entrance to a Bypass Channel in a Microfluidic System," *Phys. Rev. Appl.*, vol. 11, no. 3, p. 034020, 2019, doi: 10.1103/PhysRevApplied.11.034020.
- [149] K. Oh, K. Lee, and B. Ahn *et al.*, "Design of pressure-driven microfluidic networks using electric circuit analogy," *Lab Chip*, vol. 12, no. 3, pp. 515–545, 2012, doi: 10.1039/C2LC20799K.
- [150] A. Rakszewska, J. Tel, V. Chokkalingam, and W. T. S. Huck, "One drop at a time: Toward droplet microfluidics as a versatile tool for single-cell analysis," *NPG Asia Mater.*, vol. 6, no. 10, pp. 1–11, 2014, doi: 10.1038/am.2014.86.
- [151] B. Zheng, C. J. Gerdt, and R. F. Ismagilov, "Using nanoliter plugs in microfluidics to facilitate and understand protein crystallization," *Curr. Opin. Struct. Biol.*, vol. 15, no. 5, pp. 548–555, 2005, doi: 10.1016/j.sbi.2005.08.009.
- [152] I. A. Shestopalov, J. D. Tice, and R. F. Ismagilov, "Multi-Step Chemical Reactions Performed On Millisecond Time Scale In a Microfluidic Droplet-Based System," *Lab Chip*, no. 4, pp. 316–321, 2004, [Online]. Available: x:%5C03 Publications

- (external)%5C02                      Journalpaper%5C02                      Other                      Journals%5C2004  
 Multistep\_synthesis\_nanoparticles\_ms\_timescale.pdf.
- [153] L. Frenz, J. Blouwolff, A. D. Griffiths, and J. C. Baret, “Microfluidic production of droplet pairs,” *Langmuir*, vol. 24, no. 20, pp. 12073–12076, 2008, doi: 10.1021/la801954w.
  - [154] V. Chokkalingam, S. Herminghaus, and R. Seemann, “Self-synchronizing pairwise production of monodisperse droplets by microfluidic step emulsification,” *Appl. Phys. Lett.*, vol. 93, no. 25, 2008, doi: 10.1063/1.3050461.
  - [155] S. N. Agnihotri, M. R. Raveshi, R. Bhardwaj, and A. Neild, “Microfluidic Valves for Selective on-Chip Droplet Splitting at Multiple Sites,” *Langmuir*, vol. 36, pp. 1138–1146, 2020, doi: 10.1021/acs.langmuir.9b03515.
  - [156] A. R. Abate, J. J. Agresti, and D. A. Weitz, “Microfluidic sorting with high-speed single-layer membrane valves,” *Appl. Phys. Lett.*, vol. 96, no. 20, p. 203509, 2010, doi: 10.1063/1.3431281.
  - [157] C. W. Hirt and B. D. Nichols, “Volume of fluid (VOF) method for the dynamics of free boundaries,” *J. Comput. Phys.*, vol. 39, no. 1, pp. 201–225, 1981, doi: 10.1016/0021-9991(81)90145-5.

# List of Publications

## Journals

1. **Agnihotri, S. N.**, Raveshi, M. R., Bhardwaj, R. & Neild, A. Droplet Breakup at the Entrance to a Bypass Channel in a Microfluidic System. *Phys. Rev. Appl.* **11**, 034020 (2019).
2. **Agnihotri, S. N.**, Raveshi, M. R., Bhardwaj, R. & Neild, A. Microfluidic Valves for Selective on-Chip Droplet Splitting at Multiple Sites. *Langmuir* **36**, 1138–1146 (2020).
3. Raveshi, M. R., **Agnihotri, S. N.**, Sesen, M., Bhardwaj, R. & Neild, A. Selective droplet splitting using single layer microfluidic valve. *Sensors Actuators B. Chem.* **292**, 233–240 (2019).
4. **Agnihotri, S. N.**, Raveshi, M. R., Bhardwaj, R. & Neild, A. Controlled droplet manipulation and interaction using single-layer microvalves (Under review in *Microfluidics and Nanofluidics*)
5. M.R. Raveshi, M. Abdul Halim, **S. N. Agnihotri**, Moira K. O'Bryan, A. Neild, R. Nosrati, “*Curvature in the Reproductive Tract Alters Sperm-Surface Interaction*” – first revision received from the Journal of Nature Communications.

## Conferences

1. **S. N. Agnihotri**, R. Bhardwaj, A. Neild, M.R. Raveshi, Interaction of a Droplet with T-junction of a Microfluidic Bypass Channel, Bulletin of the American Physical Society, 2018
2. **S. N. Agnihotri**, R. Bhardwaj, A. Neild, M.R. Raveshi, Droplet Breakup in a Bypass Channel of a Microfluidic System, Proceedings of the 7th International Conference on Fluid Mechanics and Fluid Power (FMFP), 2018.
3. M. R. Raveshi, **S. N. Agnihotri**, M. Sesen, R. Bhardwaj, A. Neild, Selective Partitioning of Microdroplets Using Horizontal Microvalves, 23rd International Conference on Miniaturized Systems for Chemistry and Life Sciences, 2019.
4. **S. N. Agnihotri**, M. R. Raveshi, R. Bhardwaj, A. Neild, Towards High Throughput Screening for Drug Discovery in Multi Splitting and Merging System Using

Microvalves, 24<sup>th</sup> International Conference on Miniaturized Systems for Chemistry and Life Sciences, 2020.